Coronal Mass Ejections in the Low Solar Corona: Ion Composition and EUV Diagnostics

A Coupled Investigation using Remote-Sensing Observations and In-situ Measurements

by

Manan Kocher

A dissertation submitted in partial fulfillment
of the requirements for the degree of
Doctor of Philosophy
(Atmospheric, Oceanic and Space Sciences)
in the University of Michigan
2018

Doctoral Committee:

Professor Enrico Landi, Co-Chair
Professor Susan T. Lepri, Co-Chair
Professor Edwin Bergin
Dr. Jason A. Gilbert

'When you get these jobs that you have been so brilliantly trained for,

just remember

that your real job is that if you are free, you need to free somebody else.

If you have some power, then your job is to empower somebody else.

This is not just a grab-bag candy game.’

Dr. Toni Morrison

Manan Kocher

mkocher@umich.edu

ORCID iD: 0000-0002-4656-4325

This dissertation is dedicated to my parents

Madhu Kocher
Mahesh Chand Kocher

&

Hrivaan, Amaira, Kabir

Acknowledgements

I would like to offer my deepest gratitude to my committee, Sue Lepri, Enrico Landi, Jason Gilbert, and Ted Bergin for committing their time, energy, and expertise to this process and providing the guidance, encouragement, and feedback to help me achieve the best version of this dissertation.

I am grateful to my advisor, Sue Lepri for introducing me to the world of CMEs and giving me the tools to explore it for myself. I have developed a deep respect for their scientific perspective and find myself trying to pose questions Sue might ask. Sue has nudged throughout my four years in the program leading me to this stage. Thank you, Sue, for giving me opportunities to lecture for your courses and develop my skills as an educator. I want to thank you for giving me space to express and process how my interactions and experiences outside the office impact my work. Thank you for the opportunities and connections you have shared with me that have allowed me to enter and participate in scientific spaces I would otherwise not have access to this early in my career. Thank you for taking a chance on me.

I would like to recognize my advisor, Enrico Landi, as the probable force and inspiration behind any course I create in the future. I would like to thank Enrico for always demonstrating what the highest form of dedication, passion, and effort in any task. From meetings, emails, edits, course work, and feedback, you have pushed me to be the best researcher and educator I should aspire to be. I thank you for allowing me to always speak candidly to you as I navigated the PhD process. I thank you for taking on my every last-minute request for edits and recommendations through the last few years. I would especially like to acknowledge the critical part you've played in my journey as a scientific writer. I do not hesitate to take on proposals and enjoy the process of scientific writing – all thanks to your mentorship. I will carry these skills with me as I move forward and try to channel your dedication starting with this upcoming postdoctoral position.

Sue Lepri and Enrico Landi are an advisor dream-team. I would like to thank them for believing in me, giving me space to make my own decisions, allowing me to work independently on my own timeline, travel frequently to present my research, and making the last four years of work together joyful and fulfilling. Thank you very very much indeed, and I hope we get to work together in the future.

As a culture, we don't really thank the people we are closest to. Here is my attempt to express my gratitude to my beautiful parents: Madhu Kocher and Mahesh Kocher for giving me the best of everything. Thank you for giving me the opportunity to soar into spaces where I could discover myself, challenge myself, and be myself. Thank you for the regular suitcases of snacks from Jodhpur/Delhi/Mumbai/Jaipur, blazers for birthdays, wake up calls after all-nighters and your never-ending concern that I am not eating and sleeping enough. Thank you for your patience as I grew into my truth these past few years and for trusting that the PhD was the right step for me. Thank you for teaching me the lessons of empathy, generosity, and perseverance. Thank you for letting me choose my own path that has led me to where I am now today. I will work hard to make up for the time lost these past eight years. A big shout out to my favorite lawyer and sister, Mahak Kocher for always reminding me to not take myself too seriously. I would like to thank my uncle, Vimal Kocher, for inspiring me from a very young age. Your dedication to your work, focus, patience (and extreme neatness) have always been benchmarks of how I should carry myself in professional spaces. I have been constantly inspired and nurtured by the ethics and charms of my fabulous Marwari Kocher's and Bhandari's, and I thank them for cheering me on.

Angela Farrehi drew the framework within which I could dream of getting this stellar education. Few know of the adversities I overcame to be admitted into the PhD program, and Angie saw me through every shut and open door. Thank you, Angie, for advocating for me as a student, scientist, and human. Thank you for reteaching me to believe in myself against all odds and working with me through my fears toward my aspirations. Every achievement stems from the steps we took starting seven years ago.

I would like to thank my best and dearest friend, Dr. Fadi Shihadeh. Thank you for poetry, travels, cooking, scrapbooking and movies. Thank you for patiently cheering me on through the doctoral process with your companionship and humor. The dedication you demonstrated in your profession, your constant and vibrant curiosity, and passion to participate in our communities have pushed me to be a well-rounded scientist. Thank you for your thoughtful feedback, expert grammatical edits, and unconditional support through the variable tides of a PhD program. You have seen us through the five chapters of this dissertation and I look forward to sharing the sixth with you.

I would like to thank my CLaSP comrade Doga Can Su Ozturk without whom the walks to the coffee machine would be significantly less exciting. Thank you for your friendship, perspective, sense of humor, magnets, chocolates, and sticky notes with me. Thank you for starting DEI Tea Time with me, strategizing emails together, and processing on the daily. You made CLaSP a really special place for me, and I cannot wait to be neighbors (sort of) in a new state!

I am so grateful to have a resilient chosen family that has supported me through the PhD experience. I would like to thank Navya Varshney, Priya Thyagarajan, Puru Agrawal, and Sharon Deshpande for the regular check-ins, hangouts filled with song and dance, intimate conversations, and for being my tribe. Each one of you has motivated me to be a better researcher, student, and person through your stories, resilience, compassion, and candor. I would like to thank Zarina Kraal for sharing with me tools to process emotions and develop a better understanding of my relationship to them – skills that have improved my balance through the PhD. Thank you to Kate Curley for being an excellent study companion. Thank you, Sofia Chesnokova for every study break filled with love and humor. I would like to thank my local guardians, Sundeep Kalantry and Smita Malpani for their love, support, and a home away from Jodhpur. I would like to thank Prashant Kumbhat and Meghan Tinsley for being my beautiful US Marwari family. I would like to thank Donia Jarrar for being my PhD buddy during our candidacy trials. Donia's passion for her art has inspired me to treat my research like art. I would like to thank Erin Busbee for the excellent breakfast dates that allowed me to start many a day of research with positive reflection, gusto, and excitement. Thank you Douj Kripke and Andrew Silapaswan for being the best brothers.

The community in CLaSP has been instrumental in shaping my experience as a graduate student into an educational, enjoyable, and memorable one. I would like to thank Debbie Eddy firstly for saving the bibliography of my first publication. With your help, I am a little less scared of those sections now. Thank you for helping me navigate my travels, funds, and always taking time to ensure everything ran smoothly. I would like to thank Sandra Pytlinski for seeing me through a very interesting transition from undergrad to PhD, and now, on to the next phase. Thank you for the candid discussions, help in navigating coursework and requirements, and your gift of always being able to predict the next question. I would like to thank Elaine Meinzer, Rachel Long, and Rick Baker for coordinating every last detail and formality related to my fellowships, student status, and employment. I would like to thank Sandee Hicks for being the first person to welcome me into the CLaSP family.

I would like to thank Jason Gilbert for guiding me through my very first research project as part of the Solar and Heliospheric Research Group (SHRG). Thank you to Jim Raines for the plotting lessons, presentation feedback, and encouragement throughout the years. Thank you to Thomas Zurbuchen for teaching me what scientific questions to ask, starting from my very first SHRG meeting. I offer my deepest gratitude to Liang Zhao for their feedback, encouragement, and collaboration. I have benefited from Liang's mentorship throughout my time in SHRG, and I hope we get to work on the projects we have not gotten to yet as I navigated the PhD process. I would like to thank Micah Weberg for introducing me to graduate student life in our research group, being an excellent Python coach, and allowing me to come to them with all my coding and solar wind questions. I would like to thank Aleida Higginson for their friendship, all the coffee and lunch dates we can squeeze into our trips, candid opinions, and excellent advice on how to proceed in the next phases of my career as a Space Physicist. I would like to thank Ava Dupre for inspiring me with their work and passions since our undergrad days together. I would like to thank Justin Kasper, Michael Liemohn, Dan Welling, Jim Slavin, and Mark Flanner for leading some of my favorite courses that have significantly influenced my scientific understanding of space and its physics.

I would like to thank Darren Britten-Bozzone, Kevin McLaughlin, Faye Ogasawara, and Bryan White for guiding me through every small and big technical and coding issues that have regularly sprung up through the years. My conversations with our chair, Jim Slavin, have always added clarity to why and how I fit into the space science community. I would like to thank Jim for encouraging me through the years, sharing contacts and resources, always recognizing my passion for Space Policy, and supporting the DEI Tea Time meetings.

Over my doctoral career, I have had opportunities to interact with solar and heliospheric scientists outside UM, and my research has greatly benefited from their expertise and input. I would like to extend my deepest gratitude to Ben Lynch, John Raymond, Angelos Vourlidas, Teresa Nieves-chinchilla, Lan Jian, Barbara Thompson, Meng Jin, Mark Cheung, and Wei Liu for welcoming me into the community with their invaluable scientific feedback, hospitality during my visits, and encouragement.

Thank you to the Michigan Institute for Plasma Science and Engineering (MIPSE) for their generous fellowship in 2015. Thank you to the Rackham Graduate School for travel fellowships that have made trips to AGU conferences possible. I extend my deepest gratitude to NASA for the NASA Earth and Science Fellowship (NESSF). Supporting my research over the last two years, this fellowship gave me opportunities to travel, share my research, and develop contacts in the wider solar and heliophysics community.

Table of Contents

Chapters

List of Figures

Abstract

Coronal Mass Ejections (CMEs) are spectacular solar transients that deposit vast amounts of plasma and magnetic energy into the heliosphere. The build-up and release of plasma and energy during CME events are critically important to science and society. They involve processes at the center of the heating and evolution of the solar atmosphere that are also relevant across a range of other scientific disciplines. Furthermore, society's interconnectedness and dependence on technology makes us extremely vulnerable to solar activity and major CME eruptions, which can paralyze our indispensable space-borne and ground-based infrastructure.

This dissertation presents a study of the evolution of geo-effective CMEs using an array of remote-sensing observations, in-situ measurements, an ionization model, numerical simulations, and diagnostic techniques. These analyses attempt an extensive observational account of the evolution of the dynamics, energetics, and composition of these consequential transients. The overarching vision in these series of investigations is to develop groundwork for connecting the unprecedented remote-sensing and in-situ observations from future missions of Parker Solar Probe and Solar Orbiter.

Three central CME science topics addressed here are: (1) in-situ signatures of CME processes in the low solar corona, (2) the evolution of filament composition in the low

solar corona, and (3) the evolution of filament dynamics and energetics in the low solar corona.

First, a detailed analysis of in-situ observations of 14 years of Earth-intercepting ICMEs and associated composition anomalies is presented. 45% of these ICMEs (called 'depleted ICMEs') contained distinct periods of anomalous heavy-ion charge state composition and peculiar ion thermal properties (called 'Depletion Regions'). The most consistent characteristics of the Depletion Regions were (1) depleted fully stripped ions of helium, carbon, nitrogen, and oxygen, and (2) exposure to sources of heating before the charge states froze-in. Using results from two prominent CME models, a preliminary investigation into the possibility of the Depletion Region plasma being an in-situ signature of magnetic reconnection in the low solar corona is conducted.

To connect near-Earth observations of ICMEs to their evolution in the low solar corona, a case-study of a geo-effective ICME is presented. The event was traced to the Sun using *SOHO*/LASCO and *STEREO*/SECCHI observations. The filament eruption associated with the CME was 'followed' in multi-wavelength *SDO*/AIA and *STEREO*/EUVI images in an attempt to quantify its behavior at high-cadence. Estimates of kinematics, dynamics, and the ionization history of the filament eruption during the first hour of its journey are discussed. However, the diagnostic technique used to estimate temperature and density of the filament assumed a non-emitting plasma. Since AIA 304 Å observations where contributions from emission may be significant was used, uncertainties that were difficult to quantify were introduced to the results. This motivated the final portion of this dissertation.

A new EUV diagnostic technique is introduced that accounts for absorption as well as emission contributions from emitting channels such as 304 Å. This diagnostic technique can be equally applied to emitting and non-emitting channels, paving the way for more realistic discussion of the heating and energetics of the transient plasmas using a wider range of observations. Presented is a comparison between the results using this new diagnostic technique with the results derived when 304 Å He II emission was not considered. Improved and more precise high-cadence estimates of the evolution of filament density, temperature, speed, ionization history, and energetics are discussed.

CHAPTER I

An Introduction to Coronal Mass Ejections

I.1. Objectives and Significance:

In March of 1989 Quebec, Canada was suddenly enveloped in darkness. Electrical outages in Quebec and many other parts of North America that day were a direct consequence of powerful eruptions from our Sun three days prior. This significant **geoeffective solar storm** distracted North America with spectacular auroras that extended as far south as Florida and Cuba (Figure 1, left), as it paralyzed the Hydro-Quebec Power Authority by inducing electric ground currents that triggered the grid's protection system (Figure 1, right). The driver of the solar storm was a Coronal Mass Ejection.

Large Solar Flares Erupt Anew
New York Times (1857-Current file); Mar 13, 1989; ProQuest Historical Newspapers The New York Times pg. B5

Large Solar Flares Erupt Anew

HOLLOMAN AIR FORCE BASE, N.M., March 12 (AP) — A series of large solar flares, each with the potential to disrupt radio transmissions, have erupted in a wake of an unusually large blast, researchers at this base say.

A blast 36 times the size of Earth that occurred Thursday on the sun's northeast quarter was possibly the largest ever recorded, the researchers said.

Staff Sgt. Leroy Kirkegard said Saturday that the huge eruption of gas from the surface of the sun was followed by another large explosion Friday morning and three more on Saturday. The flares were all big enough to disrupt long-range communications on Earth, like shortwave transmissions and satellite links.

"That's uncommon — to have that many big flares in the same region in the same day," Sergeant Kirkegard said.

"It's a very disturbed area — probably two to three Earths in diameter," said Tom Folkers, a technical specialist and telescope operator at Kitt Peak National Observatory near Tucson, Ariz.

The solar flare on Thursday extended about 70,000 miles into space, said researchers at Sacramento Peak, just east of Holloman.

Tom Duvall, an astronomer at Kitt Peak, said researchers at Sacramento Peak told him that "it's the largest one they've seen — ever." He added, "This is pretty exciting for us up here."

Air Force Maj. James B. Near Jr., commander of Holloman's solar observatory in the Sacramento Mountains, said Friday that the flare was the size of 36 Earths.

Mr. Folkers said ultraviolet radiation and X-rays hit the Earth's upper atmosphere at noon Thursday, just eight minutes after the solar blast. Such radiation travels at the speed of light, he said.

Figure I.1: (left) March 13th, 1989 aurora, taken from Sea Cliff, NY, USA by Ken Spencer, (middle) snapshot of the news of the 1989 solar storm from New York Times, (right) impact of the Hydro-Quebec electrical outage in March 1989, credit: NASA

Coronal Mass Ejections (CMEs) are large-scale solar transients that erupt out of the solar corona, and deposit vast amounts of plasma in the range of 10^{15} – 10^{16} grams of ejecta and magnetic energy into the heliosphere, traveling at velocities that can exceed 2000 km/s. The frequency of CME eruptions follows the ~11 year cycle of the Sun's magnetic activity, from one CME eruption per day during solar minimum (period of reduced magnetic activity at the Sun) to nearly five a day during solar maximum (Gopalswamy et al. 2005). If incident at Earth, this influx of plasma and energetic particles can interact with the Earth's magnetic field, penetrate the Earth's atmosphere and immobilize our interconnected infrastructure. Starting with our electric power systems, it would consequently impacting sectors ranging from transportation, emergency services, government services, oil and gas, communications, water, banking and finance.

The Quebec Blackout is one humbling example of potential consequences to communities unprepared to deal with large solar storms. Investigations into CME science are crucial to our increasingly interconnected and technology-dependent society, as our ground-based, space-borne infrastructures, and communication systems are vulnerable to Earth-incident energetic CMEs (Baker et al. 2008, Riley et al. 2018). CMEs are central actors in the understanding and prediction of geoeffective **space weather**, and the connection between the Sun and the Earth's magnetic field.

In addition to their direct relevance to societal safety, the build-up and release of plasma and energy during CME events are also critically important across numerous scientific fronts. CMEs involve processes that are at the center of the energy transport and partition in the solar atmosphere, and of the time evolution of the latter; these ideas are also important in numerous other fields of plasma physics.

Also, a thorough understanding of solar CMEs is crucial to the physics of stellar CMEs from Sun-like stars and the impact of space weather and space climate on potential exoplanetary habitability, atmospheric evolution, and the astrobiological signatures of extra-terrestrial life (e.g. Vidotto et al. 2014, Drake et al. 2016).

This dissertation is scientifically motivated to: determine CME behavior in the near-Earth space; understand their spatial and kinematic evolution in the heliosphere based on how they interact with the ambient solar wind; and dissect the dynamic processes that lead to their formation at their solar source. The author presents a study of the evolution of geo-effective CMEs using an array of remote-sensing observations, in-situ measurements, an ionization model, numerical simulations, and diagnostic techniques in order to present an extensive observational account of the evolution of the dynamics, energetics, and composition of these spectacular transients. The overarching vision in these series of investigations is to develop groundwork for connecting the unprecedented remote-sensing and in-situ observations from future missions such as Parker Solar Probe (Fox et al. 2016) and Solar Orbiter[1].

---

[1] http://sci.esa.int/solar-orbiter/46022-solar-orbiter-assessment-study-report/

I.2. The Sun-Earth Connection and Coronal Mass Ejections:

The Sun can be divided into two parts – the solar interior, the optically thick portion of the Sun from where radiation is unable to escape to space, and the solar atmosphere, the portion of the Sun extending outwards where the energy generated in the solar interior begins to escape into space as radiation.

The **solar interior** (see Figure I.2 (left)) consists of four layers, which transport energy from the core out to the base of the solar atmosphere. The **core** is the innermost layer with temperatures up to 15 MK where nuclear reactions consume hydrogen to form helium and produce the enormous amounts of energy that powers our Sun. The temperatures at the outermost point of the core is half its central value and densities drop from 150 to 20 gm/cm^3. Next to the core is the **radiative zone**, where the energy generated in the core is transported via radiation. Here, the photons (light) are absorbed, re-emitted, and scattered in a random walk from particle to particle through the radiative zone until they reach the next layer, the **tachocline**. The tachocline is a thin interface layer between the rigidly rotating radiative zone and the differentially rotating convective zone of the solar interior where the Sun's magnetic field is believed to be generated and amplified due to the large shearing flows between the two layers. Above the tachocline is the **convective zone**, the outermost layer of the solar interior, where the density and temperature continue to drop, and the energy is transported to the solar atmosphere via convection because of the large temperature gradients of this layer. These convective motions are visible at the solar surface as convection cells called granules and supergranules. The tachocline-generated magnetic fields that are able to overcome the background gravitational stratification rise to the solar surface (photosphere) through the process of **magnetic buoyancy** (Parker 1955).

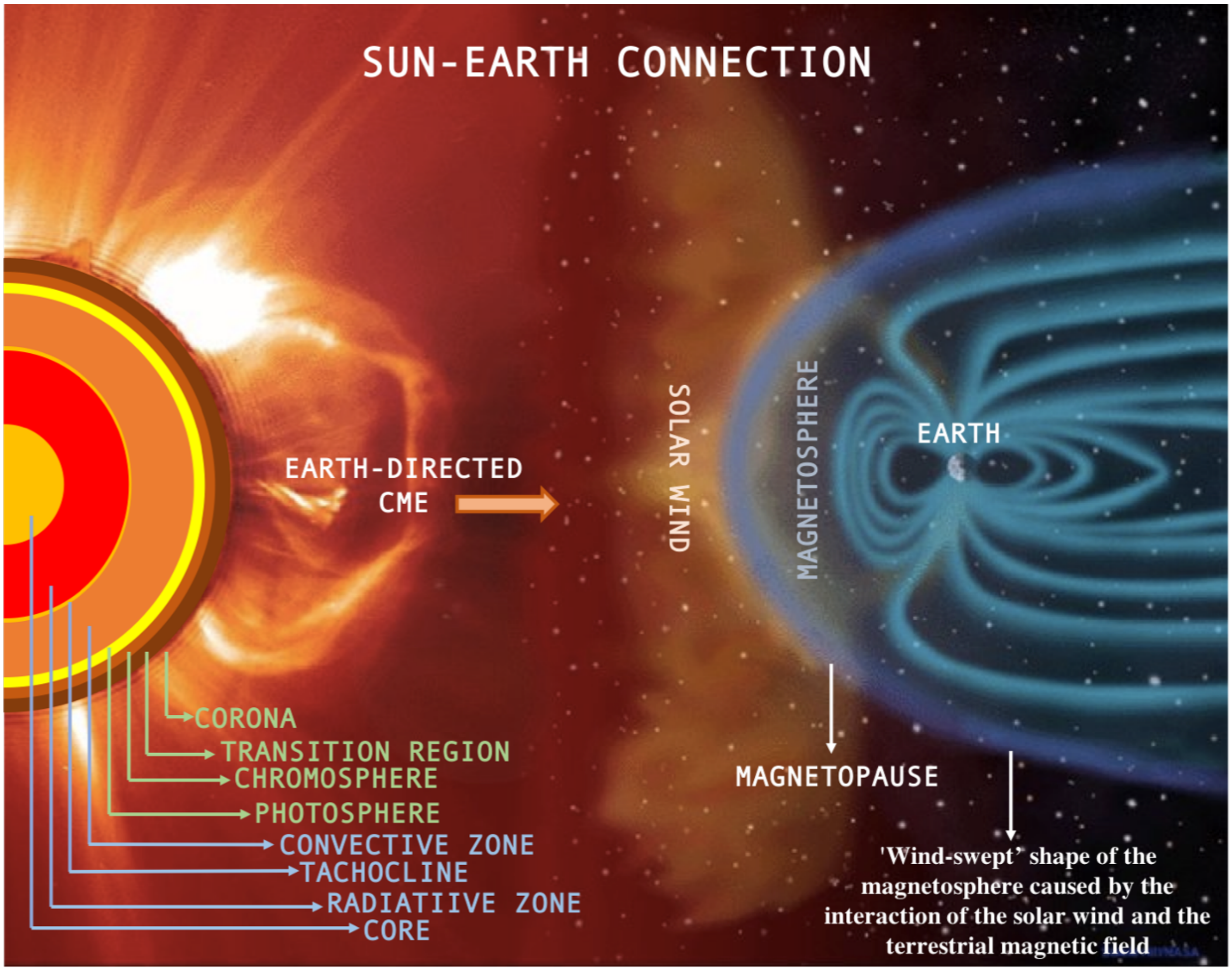

Figure I.2. The above schematic shows the different layers of the solar interior and atmosphere (left), an Earth directed filament eruption, and a cartoon of the solar wind and transient interaction with the Earth's magnetosphere. The image is not to scale. The layers of the Sun and labels are created by the author on top of a background courtesy: Magnetosphere: NASA, the Sun: *ESA/NASA* – SOHO[2]

---

[2] https://www.esa.int/spaceinimages/Images/2007/07/The_Sun-Earth_connection

The **solar atmosphere** (see Figure I.2 (left)) consists of four layers. (1) The **photosphere** is the lowest layer, visible to the naked eye and loosely regarded as the surface of the Sun. It is thin, dense, emits most of the visible sunlight and has an equivalent blackbody temperature of 5,770 K. (2) The **chromosphere** is the next layer, where the temperature starts from a minimum from 4,200 K followed by an increase to 10^4 K, possibly due to the absorption of acoustic waves emerging from the convection zone (Gingerich et al. 1971, Carlsson and Stein 1995) (3) The **transition region** is a thin region between the chromosphere and corona where the temperature increases drastically from 10^4 – 10^6 K. (4) The **corona** is the uppermost layer of the solar atmosphere where the temperatures reach a few million degrees. The corona extends into interplanetary space via the solar wind. The **solar wind** is the stream of supersonic ionized particles traveling out of the corona, carrying the solar magnetic field with it. Occasionally, CMEs erupt and disrupt this ambient solar wind, affecting the wind speed, density, magnetic field strengths, radiation and other factors that make up space weather. How the corona gets heated to millions of degrees kelvins from the ~6000 K solar surface has been an open question in the scientific community since the 1940's and is believed to be linked to complex processes related to the magnetic activity of the Sun.

One of most prominent and oldest recorded solar magnetic features are called **sunspots**, observed as dark regions on the solar photosphere (Vaquero et al. 2007 and references therein). Sunspots are colder than their surrounding photosphere, are known to have extremely strong magnetic fields, and often span a region as large as the Earth's cross-section. The number of sunspots on the solar disk provide a record for the Sun's magnetic activity; that is, a larger number of sunspots appear during solar maximum due to enhanced magnetic activity at the Sun, while sunspots are rare during solar minimum. Regions of strong magnetic concentrations in the solar atmosphere, called **active regions**, are often associated with or surround sunspots. The active regions are also often the source regions of CME eruptions. Hence, the frequency of CME occurrence also follows the ~11-year sunspot cycle. Evolving solar magnetic fields, which are engrained in the various layers of the solar atmosphere and are generated deep in the solar interior, are accordingly strongly linked to CME genesis.

The Earth is continuously immersed in the solar wind. Not only are we reliant on the Sun's energy for survival, we're also at the mercy of the solar wind and transients (e.g. CMEs) constantly bombarding and interacting with our magnetosphere. Solar wind interacts with the Earth's magnetosphere forming the 'wind swept' shape seen in Figure I.2 (right).

The interplanetary disturbance caused by the ICME (Interplanetary CME, the heliospheric counterpart of a CME) can compress the Earth's magnetosphere. When a CME interacts with the Earth's magnetosphere it can cause prolonged geomagnetic disturbances called **magnetic storms**. Most magnetic storms correspond to and are driven by long periods of southward components of the interplanetary magnetic field (IMF), which provides the most favorable situation for magnetic reconnection (process of the breaking and reconnecting of oppositely directed magnetic field lines in a plasma, see discussion in Section I.4.1) at the dayside magnetopause. This allows coupling of the solar wind and magnetosphere, providing energy and plasma input from the solar wind into magnetospheric plasma.

This coupling between the solar wind and the geo-space environment means that CMEs are an integral, and especially dangerous part of this connection and central to the study of Space Weather.

I.3. Solar and Heliospheric Observations of Coronal Mass Ejections:

A majority of this dissertation describes the analysis and interpretation of transient activity in the solar atmosphere and heliosphere. Presented here is an overview of Coronal Mass Ejection observations.

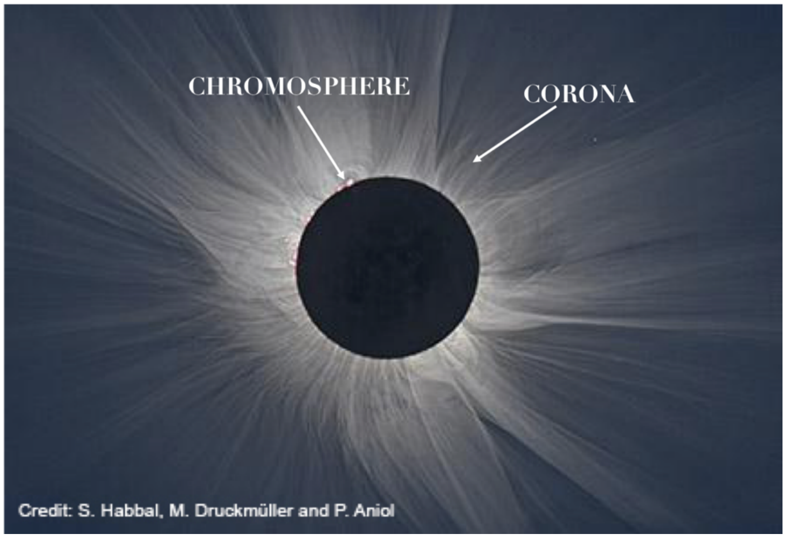

Figure I.3: Above is a total eclipse image taken by S. Habbal, M. Druckmuller, and P. Aniol on March 20th, 2015 at Svalbard, Norway. Marked in the image is the chromosphere and the corona. [*eclipse2017.nasa.gov*]

I.3.1. Remote-Sensing Observations:

A **solar eclipse** is a cosmic coincidence where our Moon passes between the Sun and the Earth; blocking the light of the solar disc and giving us the unique opportunity to observe the chromosphere, transition region, and corona. Figure I.3 shows an image of a

2015 total eclipse, where the chromosphere and corona are seen in spectacular detail. It is in the chromosphere and corona where the birth and evolution of CMEs and associated phenomena can be unraveled making eclipse observations extremely important (e.g. Hanaoka et al. (2013)).

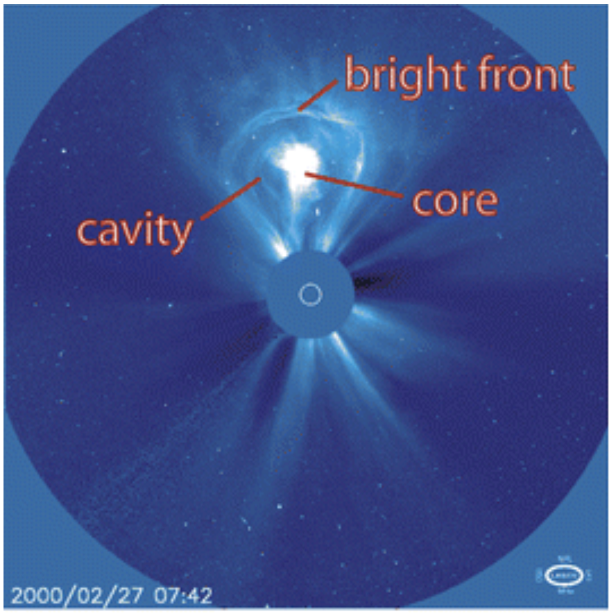

Figure I.4: Classic 3-part CME structure of a February 27th, 2000 CME, adapted from Riley et al. (2008)

Coronagraphs are Sun-observing telescopes that use a physical disk to block the Sun's bright surface so we may study the remaining solar atmosphere and surround interplanetary bodies, essentially giving us continuous artificial solar eclipse observations. Starting from the first observations of CMEs in the 1970s from the OSO-7 coronagraph (Tousey, 1973), an array of Sun-observing instruments (including coronagraphs) have provided a wealth of diverse types of remote observations of these solar eruptions across the electromagnetic spectrum, giving this generation of researchers a unique opportunity to address open questions about the initiation and evolution of CMEs.

The launch of the SOlar and Heliospheric Observatory (*SOHO*, Domingo et al. 1995) in 1995 changed the landscape of CME science with its groundbreaking routine observations of Earth-bound transients. The Large Angle Spectrometric COronagraphs (LASCO, Brueckner et al., 1995) onboard *SOHO* has three white-light coronagraphs, each with a different sized occulting disk so different portions of the corona could be observed. Two of these (C2 and C3) white-light coronagraphs view Thompson-scattered sunlight from the free electrons in coronal plasma. LASCO observes the inner and outer solar corona between 1.1-32 solar radii – with C1 from 1.1 – 3 R_{SUN}, C2 from 1.5-6 R_{SUN}. and C3 from 3.5-30 R_{SUN}. The twin *STEREO* (Kaiser et al. 2008) spacecraft launched in 2006 further enhanced our ability to study CMEs by placing identical Sun-Earth Connection Coronal & Heliospheric Investigation (*SECCHI,* Howard et al. 2008) fleet of instruments onboard the two spacecraft, allowing for multi-perspective viewing from 1-15 R_{SUN} and hence 3D reconstruction of CMEs. Each *SECCHI* suite includes two white-light coronagraphs: COR 1 observes the solar corona between 1.4-4 R_{SUN}, and COR 2 observes the solar corona between 2.5-15 R_{SUN}. The overlapping fields of view of the *SECCHI* instruments enables us to connect the same structure as it expands away from the Sun and crosses the different instruments' fields of view.

The white light coronagraph observations of CME's have revealed that CMEs have distinct forms. This archetypal structure is the commonly observed "**three-part" CME**: a bright and dense front, trailed by a low-density cavity which contains a relatively bright, high density core (Howard et al., 1985, Hundhausen, 1987, 1999). A 3-part CME observed by *SOHO*/LASCO C3 is shown in Figure I.4.

However, much of the electromagnetic radiation emanating from the chromosphere and corona has significantly higher photon energies than those of visible wavelength radiation (3900 Å – 7700 Å | 1.6 – 3 eV). In fact, chromospheric and coronal plasmas of temperatures ranging from 10^5 K – 10^6 K are strong emitters of radiation in the Ultra-Violet (UV, 1000 – 3900 Å), Extreme Ultra-Violet (EUV, 100 – 1000 Å) and soft X-Ray (1 – 100 Å) range. White-light coronagraphs also block the innermost region of the corona where the birth and initial evolution of the CMEs take place. Hence, in addition to white-light observations, full-disk observations from multi-wavelength telescopes are necessary tools used to expose the different layers and features of the solar atmosphere.

Three solar disk observing telescopes in coronal to EUV wavelengths that have greatly contributed to CME science are introduced here. (1) *SOHO*'s Extreme Ultraviolet Imaging Telescope (*EIT*, Delaboudiniere et al. 1995) provides observations of the full disk and up to 1.5 R_{SUN} of the solar atmosphere in 171 Å, 195 Å, 284 Å, and 304 Å spectral emission lines, allowing us to observe plasmas in the temperature range of 10^4 – 10^6 K. (2) The Extreme Ultraviolet Imager (*EUVI*, Howard et al. 2008) on board the twin *STEREO* spacecraft observe the solar corona below 1.7 solar radii in 171 Å, 195 Å, 284 Å, and 304 Å channels. (3) The Advanced Imaging Assembly (*AIA*) (Lemen et al. 2012), onboard *SDO* (Pesnell et al. 2012) gives us pioneering tools to study CME source regions with its high cadence full Sun EUV observations in 94 Å, 131 Å, 171 Å, 193 Å, 211 Å, 304 Å, and 335 Å, with temperature diagnostic capabilities covering the range from 6 x 10^4 – 2 x 10^7 K.

The energetics of a CME are best studied if we know the varying properties of their heterogenous components over spatial and temporal scales. In the case of the three-part CME, the temperatures and densities of the core, cavity, and front can span a few orders of magnitude, can be traveling at different speeds, and can have varying spatial dimensions. Hence, neither the field of view of a single imager, nor the diagnostic potential of a single wavelength band is sufficient to study the various parts of a single CME. A coordinated consortium of coronagraphs, multi-wavelength imagers, and spectrometers are required to diagnose and map the complete evolution of CMEs over distances sufficient to understand their complex evolution, dissect the intricacies of their different magnetic or plasma features and then follow their evolution over time. Implementing coordinated analysis of multi-instrument observations to a single solar event is challenging because of the different spatial resolutions, time resolutions, and fields of view of the various instruments. This will be explored in Chapters III and IV of this dissertation.

CME cores are frequently made of a commonly observed feature in the solar atmosphere, an erupting filament. Often observed in EUV images, **filaments** are long tendrils of very cold and dense gas etched in the million-degree corona that are thermally and pressure isolated from the surrounded plasma. When observed at the limb, these structures are called prominences. The average filament length can vary between 10^4 – 10^5 km (Bernasconi et al. 2005, Wang et al. 2010). They are primarily found all around the border of polar coronal holes, between active regions or in their vicinity (intermediate filaments), and inside active regions (active filaments). Filaments found near coronal holes and active regions typically have larger lengths and longer lifetimes due to the stable nature of the environment they live in. They are called quiescent filaments, examples of which are shown in Figure I.5 (left). The longest filaments can cover the diameter of the Sun, as seen in the western hemisphere in He II emission *SOHO/EIT* image in Figure I.5 (left), suggesting a connection between filaments and the large scale magnetic structure of the Sun (Parenti 2014).

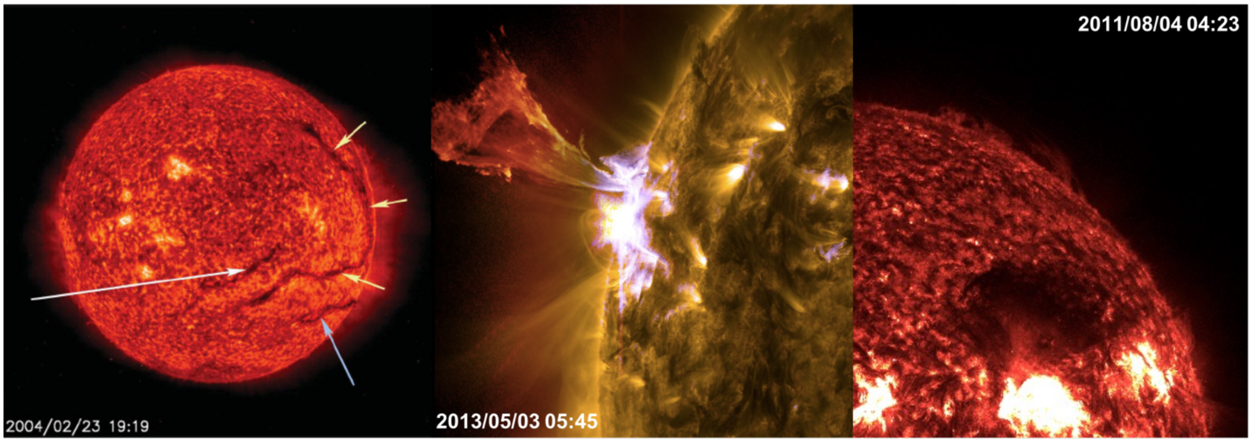

Figure I.5: (left) He II 304 Å *SOHO/EIT* images from February 23rd, 2004 showing 3 quiescent filaments [Parenti 2014], (middle) erupting filament from May 3rd, 2013 seen as a bright emitting feature in *SDO/AIA* 131 Å, 171 Å, and 304 Å channels. Flare seen near the surface [Goddard Media Studios], (right) erupting filament from August 4th, 2011 seen in *SDO/AIA* 304 Å as a dark feature indicating absorption properties [Kocher et al. 2018]

The low temperatures of filaments mean they are composed of partially-ionized plasma, and their high densities imply they are optically thick in certain wavelengths. Hence, in prominent chromosphere lines such as He II 304 Å which is emitted at ~50,000 K they appear darker than the surrounding quiet Sun. When observed in MK coronal temperatures, they are either not seen or seen in absorption. Figure I.5 (right) shows an erupting filament as a dark absorbing feature against the hot chromosphere in 304 Å. If a solar feature is observed in 'absorption' in a specific wavelength band, it implies the atoms/molecules in the optically thick plasma made a transition from a lower to a higher energy level and a photon, emitted by the plasma in the background, was absorbed. This process results in the dark absorption feature along that line of sight of observation.

Conversely, if a solar feature is observed as brighter than its background in a specific wavelength band – an emission feature – it implies the atoms/ions within the plasma made a higher-to-lower energy level transition, emitting additional energetic photons along the line of sight. This process results in the bright emission feature along that line of sight of observation. Figure I.5 (middle) is a composite image of three *SDO*/AIA wavelength channels observing an erupting filament and the surrounding corona in emission: 131 Å which observes the multi-million Kelvin active corona and flaring regions (hence the flaring loops are seen at the solar surface), 171 Å which observes the upper transition region and quiet corona, and 304 Å which observes the transition region and chromosphere. Composite images are extremely valuable in analyzing the multiple aspects of the filament eruption that a single wavelength filter cannot provide.

Filaments are extremely important to CME dynamics because upon eruption, they frequently form the dense core of the three-part CME structure (House et al. 1981, Webb and Hundhausen, 1987, Gilbert et al. 2000, Zhang et al. 2001, Gopalswamy et al. 2003). Studies have also shown that energetics of CME cores forms a significant portion of the energetics of the entire CME itself (Landi et al. (2010)); hence, filament observations are highly valuable to our understanding of processes involved in the onset of CMEs.

In order to understand the energetics of filaments and CME cores (along with the other CME components) we need to be able to estimate the time and spatial evolution of their thermodynamic and kinetic properties at high cadence and spatial resolution. Remote-sensing observations of the corona in EUV, UV and X-Ray domains are mainly conducted using high-resolution spectrometers, narrow band imagers and broad band imagers. High-resolution spectrometers preserve diagnostic potential across the entire wavelength range of observations; however, their field of view is limited to narrow slices of the Sun (e.g. *Hinode*/EUV Imaging Spectrograph (EIS)*,* Culhane et al. 2007). Wider slits can compromise the line profile resolution, creating confusion by blending nearby lines together. In using narrow slit observations to cover rapidly evolving and expansive events such as CMEs over larger areas of the Sun, we compromise on temporal resolution and simultaneity of the observed event (Landi and Miralles 2014). Narrow-band imagers on the other hand sum in each spatial pixel, all the spectral features within the wavelength range transmitted by the instrument’s coating and create a two-dimensional image over the entire field of view. Imagers such as *SDO*/AIA give us multi-wavelength full-Sun observations with 12 second cadence allowing for simultaneous and rapid visualization of CMEs and their various components. However, the lack of spectral resolution posed limitations on the diagnostic potential that spectral lines can provide. Nonetheless, with rigorous knowledge of the atomic physics involved in the formation of different emission and absorption lines of the solar spectrum, we are able to perform quantitative analysis of these narrow-band images via some cutting-edge **diagnostic techniques**.

For instance, responses of different wavelength filters to temperatures of plasmas along the line of sight can be used to determine the thermal distribution of plasmas everywhere in CMEs (e.g. Hannah and Kontar 2013). Studies such as Gilbert et al. (2005), Gilbert et al. (2011), Landi & Reale (2013), Landi & Miralles (2014), Hannah & Kontar (2012, 2013), and Williams et al. (2013) developed techniques that measure properties of transient plasmas utilizing dark absorption features or bright emission features from EUV and X-ray images. Some of these techniques, the observations they utilize and the associated measurements are listed in Table I.1. An extensive review of absorption diagnostic results can be found in Gilbert et al. (2011).

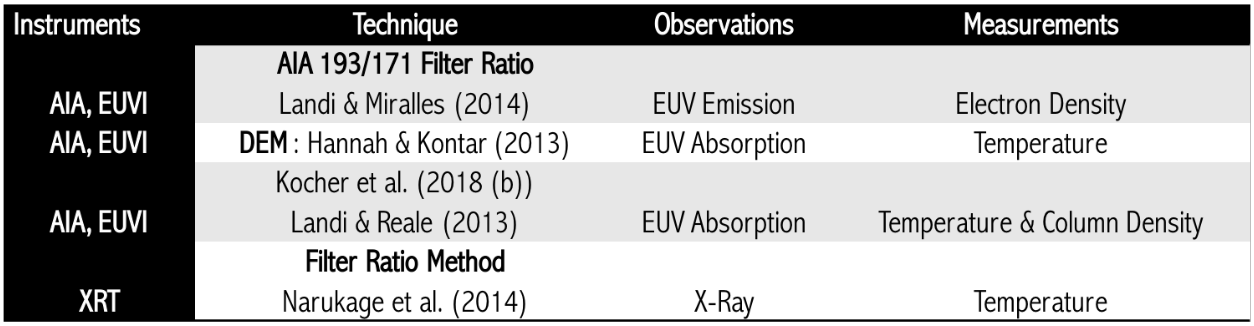

Instruments	Technique	Observations	Measurements
AIA, EUVI	**AIA 193/171 Filter Ratio** Landi & Miralles (2014)	EUV Emission	Electron Density
AIA, EUVI	**DEM** : Hannah & Kontar (2013)	EUV Absorption	Temperature
AIA, EUVI	Kocher et al. (2018 (b)) Landi & Reale (2013)	EUV Absorption	Temperature & Column Density
XRT	**Filter Ratio Method** Narukage et al. (2014)	X-Ray	Temperature

Table I.1. Some diagnostic techniques to measure density and temperature from EUV and X-Ray observations

A recent study by Lee et al. (2017) demonstrated some of the abovementioned diagnostic techniques in their investigation of an erupting prominence and loops associated with a January 25th, 2012, CME observed by SDO/*AIA* first as absorption features, which then changed into emission features as the plasma heated up. They used a polychromatic diagnostic technique to compute column densities of the absorbing plasma, performed the Differential Emission Measure (DEM) analysis to compute column densities and temperatures of the emitting plasma, estimated the mass of the erupting loops and prominence, and then computed the energetics and heating of these erupting features. Another study by Rodkin et al. (2017) performed DEM diagnostics on multi-wavelength *SDO*/AIA observations of a series of solar wind transients to derive averaged electron temperatures and densities of the associated CME plasma structures at five different times. However, in order to utilize derived CME plasma parameters to constrain models and validate the heating and acceleration processes, these parameters need to be derived at multiple points in the eruption at higher cadence while ensuring the evolution of the same transient plasma is tracked. Chapters III and IV of this dissertation will explore the applications and limitation of EUV diagnostics on multi-wavelength observations of filament eruptions in detail.

I.3.2. In-situ Observations:

As CMEs expand into the outer corona they can be tracked by a variety of heliospheric instruments, such as: white-light coronagraphs, EUV telescopes, heliospheric imagers on board the twin-*STEREO* spacecraft, and white-light coronagraphs and EUV telescope on board *SOHO*. In addition to the evolution of their thermal and kinetic properties, the evolution of the various ionization states has proved itself an excellent tool for scientific investigations of CMEs. The heliospheric counterpart of CMEs, interplanetary CMEs (ICMEs) (Zhao & Webb 2003) have been explored by spacecraft such as the *Advanced Composition Explorer (ACE)*, *WIND, Ulysses, and Helios*. Using the unprecedented in-situ measurements drawn from their instruments, we are now able to identify ICMEs using a combination of magnetic field, plasma, compositional, and energetic particle signatures (summarized in Zurbuchen & Richardson 2006).

Magnetic field signatures of ICMEs are extensively documented. A well-organized subset of ICMEs called magnetic clouds (e.g. Klein and Burlaga 1982) have enhanced magnetic field, that rotates slowly through a large angle, have low proton temperatures, and low plasma beta (ratio of thermal and magnetic energies). A schematic of a magnetic cloud ICME headed to Earth, with the distinct twisted magnetic field, called a 'flux rope' like structure is shown in Figure I.6.

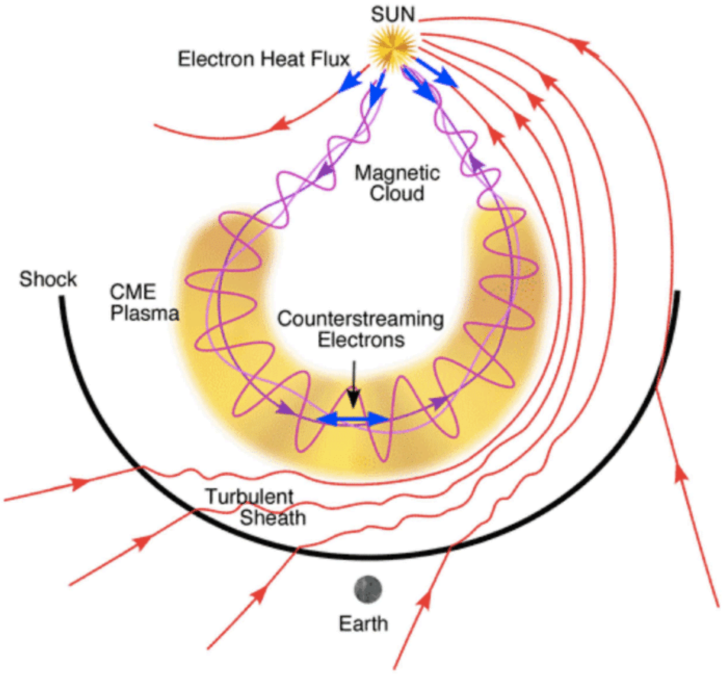

Figure I.6. Schematic of an ICME configuration from Zurbuchen and Richardson (2006). The Sun is at the top and the Earth is at the bottom with the ICME propagating towards the Earth. The coronal plasma in the CME is shaded in yellow. The shock is propagating ahead of the CME plasma, with the turbulent sheath, where the magnetic field lines are kinked, between them. Contained within the CME is the Magnetic Cloud where the magnetic field lines are twisted by the CME.

The importance of ionic composition measurements near 1 AU can be understood by a process commonly referred to as **'freeze-in'**. The ion composition of plasma parcels (ambient solar wind and CME plasmas) is controlled by ionization and recombination processes. These atomic processes are in turn modulated by the local electron density, temperature, and speed of the parcel. Since the electron densities of solar wind plasmas typically drop due to expansion as they travel to higher altitudes above the solar surface, the ionization and recombination processes become less and less efficient until eventually they shut down, and the plasma ionization states stop evolving. This process is known as freeze-in and typically occurs between 1-5 solar radii for the ambient solar wind (Hundhausen et al. 1968, Hundhasusen, 1972, Bame et al. 1974, Buergi & Geiss, 1986, Geiss et al. 1995). Figure I.7 shows two freeze-in related plots from the literature.

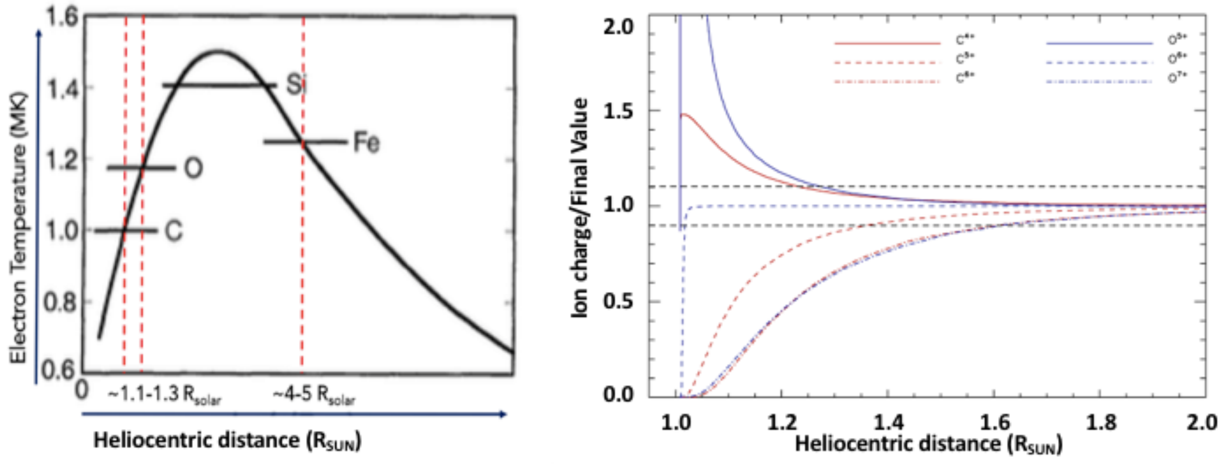

Figure I.7: (left) Schematic of electron temperature profile with increasing height away from the photosphere, marked with heights at which carbon (C), oxygen (O), silicon (Si), and iron (Fe) freeze-in. Modified from Geiss et al. (1995). (right) Landi et al. (2012) results of ionization profiles computed using inputs from a theoretical model for density, temperature and speed. On the y-axis is the ratio of density of $C^{4\text{-}6+}$ and $O^{5\text{-}7+}$ to the frozen-in density of the same ion seen by SWICS, with increasing height away from the photosphere. Both plots show that C and O freeze-in a similar region close to the Sun.

Figure I.7 (left) is a schematic from Geiss et al. (1995) that shows electron temperature versus height above the solar surface. Approximate heights at which charge states of C, O, Si, and Fe are expected to be frozen-in are marked. The corresponding electron temperature of the solar wind plasma in the freeze-in region of the specific ion is given by the y-axis. Figure I.7 (right) is an important result from Landi et al. (2012) that shows the evolution of the relative abundance of the most abundant charge states of carbon and oxygen over heliocentric distance in the low solar corona. The ionic composition was calculated for a theoretical model for the plasma temperature, density, and outflow speed of an open magnetic flux line in a coronal hole as a function of distance from Cranmer et al. (2007). The first critical take-away from these plots is that the process of freeze-in occurs over a range of heliocentric distances, depending on the different ion species. Second, freeze-in is strongly dependent on the properties of the plasma, therefore expected to exhibit great variation between different solar wind plasmas and even the different components of the same CME (Figure I.4). Third, in-situ charge state measurements of oxygen and carbon are excellent diagnostic tools of the solar corona, since they freeze-in relatively close to the Sun and are sufficiently well-resolved in time-of-flight instruments such as *ACE*/SWICS. For instance, the O^{7+}/O^{6+} ratio has been used in determining different properties of the solar wind (e.g. Zhao et al. 2009, 2014; Zurbuchen et al. 2000), and C^{6+}/C^{4+} can be used to do the same with higher sensitivity (Landi et al. 2012).

When the charge states freeze-in they retain characteristics that are determined by the electron temperature and density in the freeze-in region, thus carrying along a thermodynamic history of the CME parcel in the low corona. Hence, charge state composition measurements in ICMEs made beyond the freeze-in region reveal information about plasma conditions and acceleration close to the Sun. Accordingly, in-situ charge state ratios of heavy ions can be an effective diagnostic tool for studying coronal electron temperature, density, and wind velocity before freeze-in height in the corona (e.g. Zhao et al. 2009, 2014).

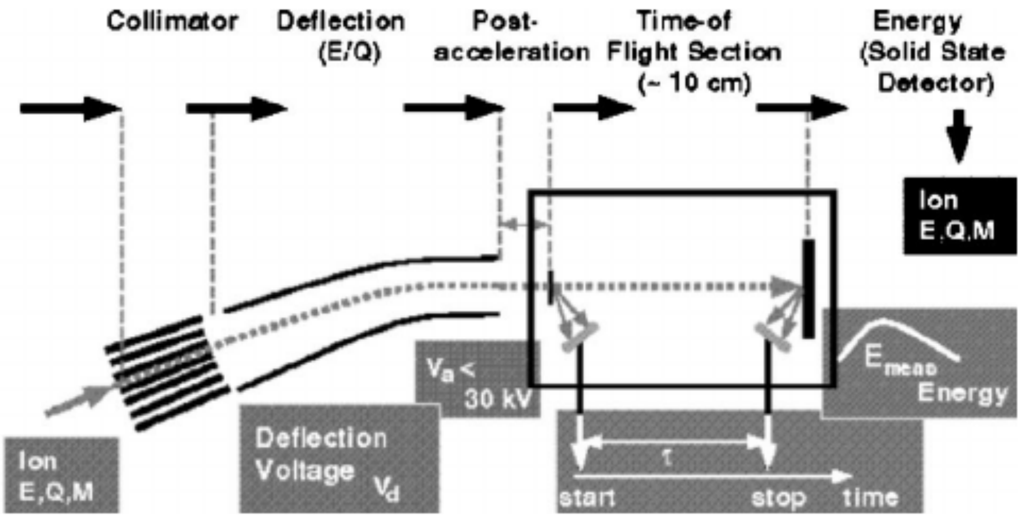

Figure I.8. Schematic of measurement technique used by *ACE*/SWICS. Adapted from Gloeckler et al. (1998). The various steps are described in the text of Section I.3.2.

Central to the investigation presented in this dissertation, the Solar Wind Ion Composition Spectrometer (*SWICS*, Gloeckler et al. 1998) is a time-of-flight - energy mass spectrometer on *ACE* optimized for measurements of the chemical and isotopic composition of solar and interstellar matter. *SWICS* separates solar wind ions by their mass m, charge q, and energy E using a triple coincidence measurement procedure. A schematic of the instrumental technique adapted from Gloeckler et al. (1998) is shown in

Figure I.8 and is briefly described here. Ions entering the collimator pass through an electrostatic analyzer that allows specific energy/charge passband ions to enter. The admitted ion is post-accelerated through a fixed negative potential (V_d) after which it is incident on a thin carbon foil, triggering the ejection of secondary electrons. These electrons are accelerated towards a microchannel plate, where they trigger a 'start signal' when they hit it. The ion then travels a distance of 10 cm before hitting a final gold-plated solid-state detector that measures the energy of the particle. At the same time, the collision ejects other secondary electrons, that are accelerated towards a second microchannel plate, where they trigger a 'stop signal' upon arrival. The difference between the start and stop signal gives the time-of-flight measurement. The triple coincidence event occurs when a stop signal and energy signals are simultaneously recorded within 200 ns of a start signal, and it allows to determine unambiguously the incident ion's mass, charge, and energy. ACE/*SWICS* has provided the community with reliable observations of over 40 ions (von Steiger et al. 2000, Shearer et al. 2014), including the following commonly observed ion species in the solar wind: H^{+} , $_3He^{1-2+}$, $_4He^{1-2+}$, C^{2-6+} , N^{2-7+} , O^{2-8+} , Ne^{6-9+} , Mg^{6-12+} , Si^{6-12+} , S^{6-14+} , and Fe^{3-24+} since 1998. Proton density and speeds are available over averaged twelve-minute cadence, and ion densities, ion thermal speeds, and ion bulk speeds at one and two-hour cadence are available at the ACE Science Center online database[3].

---

[3] http://www.srl.caltech.edu/ACE/ASC/

Plasma signatures of ICMEs include unusually low proton temperatures (Gosling et al 1973, Richardson & Cane 1995), bidirectional supra-thermal electron beams (Gosling et al. 1987), and low electron temperature (Montgomery et al. 1974). Also, elements heavier than helium make up less than 2% of the Sun, however play an important role in the physics of CMEs. Plasma composition anomalies, relative to the composition of the ambient solar wind, are extremely effective ICME identifiers (Zurbuchen et al. 2003). Enhanced helium abundance relative to proton (Hirshberg et al. 1972), enhanced iron charge states (Lepri et al. 2001; Lepri & Zurbuchen 2004), and enhanced oxygen charge states (Rodriguez et al. 2004) are amongst the anomalies observed in different populations of ICMEs. Cane & Richardson (2003) identified ICMEs in near-Earth solar wind primarily using a combination of magnetic field and proton temperature signatures. Richardson & Cane (2004, 2010) refined their ICME identification technique by incorporating an analysis of the departures of plasma composition measurements from the expected values in the ambient solar wind. However, these signatures are considered with caution due to their event-to-event variability (Gosling 1993), making ICME identification a complicated yet intriguing science.

I.3.3. The Remote- In-situ Connection:

In-situ measurements and remote-sensing observations, discussed in the previous two chapters, are two vastly different types of measurements involving different instruments, observation techniques and analysis methods. Both classes of measurements have been the foremost contributors to our existing knowledge of transient solar phenomena, such as CMEs. In-situ observations of ICMEs tell us about the state of the plasma after the freeze-in process. Remote-sensing observations of CMEs contribute to our understanding of CMEs immediately after eruption and near their coronal source. However, in-situ observations cannot inform us about the processes involved in the initiation of the CMEs. This is demonstrated by the fact that the ion composition of the CME before freeze-in cannot be determined directly from in-situ composition measurements, because the plasma temperature inferred from these measurements has little direct correlation with the actual temperature in the region before the freeze-in point (Landi et al. 2012). Conversely, remote-sensing observations of CMEs can tell us little about the final state of the plasma after the plasma has left the instrument's field of view. Conducting coordinated investigations of remote-sensing and in-situ observations can be an excellent way to study the complete evolution of CMEs from their birth through freeze-in, to their incidence in near-Earth space.

Studies in the past decade such as Gruesbeck et al. (2011), Landi et al. (2012), Rodkin et al. (2017), and Zhao et al. (2017) have discussed and implemented techniques that use combinations of in-situ and remote-sensing measurements to provide additional insight into CME dynamics at their source and through their heliospheric evolution. For instance, Gruesbeck et al. (2011) used in-situ ionic charge state measurements of a January 27th, 2003 ICME from *ACE*/SWICS to constrain the early evolution of the CME plasma, focusing on the characteristic bi-modal nature of iron distribution with typical peaks at Fe^{10+} and Fe^{16+} (Lepri et al. 2001). By modeling the freeze-in condition of the CME using different temperature and density profiles, they concluded that the bi-modal iron charge distributions along with the observed carbon and oxygen distributions are best matched if the CME plasma underwent rapid heating followed by rapid expansion from a high initial density before freeze-in.

Landi et al. (2012) presented a new diagnostic technique that combined ion composition measurements from instruments such as *ACE*/SWICS and high-resolution spectral observations of the inner corona from instruments such as *Hinode*/EIS. The goal of this combination was to (1) utilize the strength of both observation techniques, (2) investigate the heating and acceleration mechanisms in the solar wind, and (3) understand and identify the origins of the solar wind. As a demonstration of the technique, the Cranmer et al. (2007) solar wind model was used as inputs to an ionization code to test against spectra and in situ measurements to determine whether the wind model predictions were realistic. They found that several changes to the input curves were necessary to reach a satisfactory agreement.

Another novel method of connecting in-situ observations back to Sun was demonstrated by Zhao et al. (2017) in the form of their solar wind mapping technique, which maps the in-situ solar wind composition, plasma, and magnetic field measurements obtained by *ACE* back to the solar surface by a radial ballistic mapping technique from the spacecraft to 2.5 R_{SUN}, followed by a Potential Field Source Surface extrapolation to the photosphere. The state-of-the-art techniques and models used are described in Zhao et al. (2009, 2013a, 2013b, 2017) and references within. Zhao et al. (2017) categorized the solar wind (into six types) based on the identified location of the wind's coronal source regions using this mapping technique.

In the very near future, the Parker Solar Probe mission will provide us with the first in-situ measurement of the outer-layers of our Sun's atmosphere when its orbit around the Sun will bring it as close as 9-10 R_{Sun}. Combining their unprecedented in-situ measurements with remote-sensing and in-situ observations from Solar Orbiter and other heliospheric missions will be the prime challenges presented to our community. Investigations presented in this dissertation were intended to provide rigorous groundwork for connecting these diverse classes of observations and enable us to constrain the thermal evolution of CME plasmas between the Sun and Earth.

I.4. CME Science Questions of Interest:

I.4.1. In-situ Signatures of CME Processes in the Low Solar Corona:

Section I.3.2 described some notable heavy-ion signatures that are used to identify geo-effective ICMEs in in-situ solar wind observations. These compositional measurements of transient plasma carry signatures of the thermal environment in which they traveled. For instance, more than 80% of ICMEs contain signatures of million-degree (coronal) temperatures via elevated ionic charge states (e.g. Lepri et al. 2001, Henke et al. 2001, Richardson and Cane 2004). This consistent behavior has potential to lead us to the underlying coronal physical process that produced this peculiar plasma composition. For instance, the elevated charge states imply heating of that plasma parcel before those charge states froze-in and while the ICME plasma parcel continued to expand. This is thought to be a result of heating due to flare-related magnetic reconnection (described below) which is often associated with CMEs (Rakowski et al. 2007, Lepri & Zurbuchen 2004). **Flares** are localized explosive releases of energy in the range of 10^{21}-10^{25} Joules in the form of electromagnetic radiation and energetic particles that appear as quick brightenings in the chromospheric, EUV, and X-Ray emission.

What can we learn about processes that occur during CME initiation and acceleration via in-situ ICME observations? An in-depth look into this science question needs to be preceded by a discussion of the common mechanisms that lead to CME formation, eruption and the processes involved. In addition to remote-sensing and in-situ observations of CMEs and accompanying eruptive phenomena, such as filaments and flares, models of CME evolution and the underlying MHD theory are critical to the understanding of CMEs. Our scientific community relies on CME simulations and models to provide quantitative information on the physical processes that shape CMEs during eruption and their heliospheric evolution. CMEs are phenomena that involve so many different types of plasma emission, and whose properties span so many different orders of magnitude (spatial, temperature, temporal), that a comprehensive observation of a CME in all its manifestations is essentially impossible. Models are hence essential to tie the different observational pieces together, and also to provide information on what one cannot see while observing a single portion of a CME.

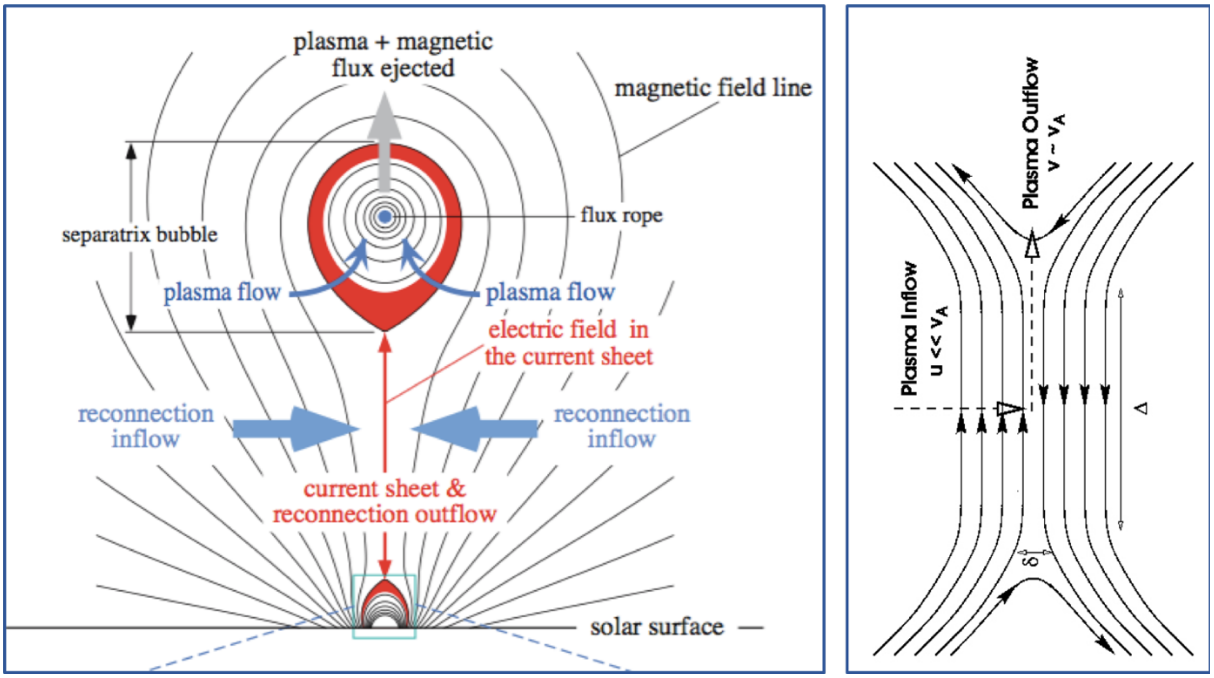

Figure I.9. (left) Flux Cancellation/Catastrophic model of CME initiation (Lin and Forbes (2000)) shows reconnection is required in the extended current sheet below the flux rope for it to be ejected. (right) Schematic of magnetic reconnection – that would be required in the current sheet of the Flux Cancellation model – where the vertical, oppositely-directed field lines would reconnect and result in flux rope ejection. Adapted from Webb and Howard (2012).

While it is widely accepted that CMEs are triggered by magnetic eruptions, much ambiguity exists regarding the magnetic field configurations that cause the eruption. Flux cancellation (Moore and LaBonte 1980), shearing motions (Low, 1977), magnetic breakout model (Antiochos et al. 1999), and catastrophe-related triggering (Forbes, 2000) are four of many proposed mechanisms (see review in Chen 2011). A schematic of the catastrophic model is shown in Figure I.9 (left) (Lin and Forbes 2000, Lin 2004). Though there is no one-to-one relationship between flares and CMEs, this model describes both. The magnetic arcade (top) containing the flux rope at its core begins to rise, causing a current sheet to develop below it. The oppositely directly field lines converge and eventually reconnect. **Magnetic reconnection** refers to the dynamic process of the breaking and reconnecting of oppositely directed magnetic field lines in a plasma and is central to many astrophysical phenomena. It is believed that energy is liberated in this process, adding mass and energy to the CME plasma (Webb and Howard 2012), as the magnetic field energy is converted to plasma kinetic and thermal energy. This energy can also heat the low lying magnetic loops, travel down the loops to the chromosphere, and trigger a flare (brightening seen near the solar surface in Figure I.5 (middle)).

The mechanism responsible for CME onset is difficult to observe, and white light coronagraphs have been unsuccessful in providing us with an accurate description of features such as the current sheet described above and the underlying magnetic reconnection morphology. The nature of the current sheets can have significant effects on the characteristics of the CME plasma, and current sheet investigations are complicated by the fact that they vary greatly in their altitude above the corona (Lin et al. 2005), as well as duration of their lifespan. While we have current sheet density, temperature, and composition estimates from UV and EUV data (Ciaravella et al. 2002; Ko et al. 2003; Landi et al. 2010, 2012), the environment in which important processes such as reconnection occurs in the low solar corona continues to be an open question. Whether or not magnetic reconnection is necessary for CME eruptions is still debated in the community. Soft X-Ray and EUV brightenings are the most common remote observations used as evidence to support the central role of magnetic reconnection in CME eruptions (Chen 2011). **What can we learn about processes that occur during CME initiation and acceleration via in-situ ICME observations?** Chapter II of this dissertation utilizes in-situ measurements of heavy ions in ICMEs to explore evidence of magnetic reconnection in the low solar corona.

I.4.2. Evolution of Filament Composition in the Low Solar Corona:

Filaments (described in Section I.3.1) have consistently fascinated solar scientists due to the high frequency of observations associated with CMEs. Based on white-light, microwave, and EUV remote-sensing observations, it is widely accepted that over 70% of all CMEs are associated with filament eruptions (e.g. Gopalswamy et al. 2003, Webb and Hundhausen 1987). The story of filament-CME relationship is less convincing on the in-situ front however. The cool filament plasma ($T{\sim}10^4$ K) foster a significant fraction of neutrals and low states of the various heavy ions. The most evident limitation of observing this compositional make-up in-situ is our inability to measure neutral atoms. Lepri & Zurbuchen (2010) introduced a novel method to identify cold filamentary material in *ACE*/SWICS observations using low charge states of carbon, oxygen, and iron. An example of an ICME with the cold filamentary material ('Cold ICME') is shown in Figure I.10. They reported that all cold events between 1998 and 2007 were associated with ICMEs, all but one Cold ICME were associated with filament eruptions in remote-sensing observations, and out of the 283 ICMEs identified by Richardson & Cane (2010) from 1998-2007, only 4% were Cold ICMEs.

This fraction is significantly lower than the 70% of CMEs observed near the Sun associated with filament eruptions. This could be due to the rigid definitions of what a

Cold ICME is according to the Lepri & Zurbuchen (2010). It could also be due to the low filling factor of the filament within the ICME. For instance, Lee & Raymond (2012) investigated 10 ICMEs observed in *SOHO*/UVCS and showed an average filling factor of ~10% of the low ionization state plasma in these events observed between 1.4 - 2.3 R_{SUN}. This could be taken as concrete evidence that the lack of low ionization states observed by *ACE* results from the small probability of the spacecraft intercepting these cold regions. A recent study by Ding and Habbal (2017) of spectroscopic observation of the March 20th, 2015 solar eclipse (Figure I.3) also found that 10% of redshifted plasmoids observed in Fe XIV emission had neutral and singly ionized plasma below $2x10^5$ K, observed in filament anchored at the Sun at that time. They also notably concluded that cold filaments nestled in CME fronts maintain their 'cold' ionic composition as they are expanding away from the Sun. However, how does the composition of the filament's plasma *evolve* in the low solar corona before freezing in? This is poorly understood.

Some numerical modeling efforts have attempted to address the unknowns of filament composition evolution in the low solar corona. The diagnostic method proposed by Landi et al. (2012) as well as the Gruesbeck et al. (2011) study, both described in Section I.3.3, used a freeze-in ionization code to compute the composition of CME plasmas in the low solar corona, using inputs of density, temperature, and speed from theoretical models. Lynch et al. (2011) computed two-dimensional spatial distributions of C, O, Si, and Fe for CME simulations comparing initiation by flux cancellation (Reeves et al. 2010) and magnetic breakout (Lynch et al. 2008) processes. They found evidence of enhanced heavy-ion charge states in the CME plasma formed as a consequence of flare heating during eruption initiation. Rakowski et al. (2007) investigated the time-evolution of ionization of various elements using a model of CME hydrodynamic evolution and compared them with in-situ ion composition measurements in CMEs. They concluded that the CME core plasma required further heating following filament eruptions, with the thermal energy input comparable to the kinetic energy. A following study by Rakowski et al. (2011) modeled a filament eruption as an expanding spheromak to understand the heating and evolution of CMEs via non-equilibrium ionization modeling. The investigation concluded that while the spheromak configuration was a reasonable approximation for the magnetic topology of CMEs, other means of energization are necessary to justify the degree of rapid heating observed. However, these models of ionization and heating are seldom constrained with observation-based estimates of filament dynamics and kinematics.

A fundamental assumption made in looking for filamentary material in in-situ data is the fact that plasma remains 'cold' when the charge states freeze-in; hence, low charge states are the evident observational signatures that are sought out. However, since measurements of the evolution of the composition of filamentary material in the low solar corona are rare, it is not well understood how the filamentary material is affected by well-documented low coronal processes, such as flare heating. For instance, the ICME shown in Figure I.10 also shows signatures of very hot plasma, in the form of high charge states of iron, indicating flare-heated plasma. It is plausible that (parts of) the filament also experiences heating in the low solar corona, hence altering their compositional make-up. The high density of filamentary material implies the charge states freeze-in much farther in the corona than what is expected of the ambient solar wind (Howard et al. 2015), giving it more time to evolve. **Quantifying how the composition of filamentary plasmas**

evolve in the low solar corona before freeze-in is essential to improving our understanding of Earth-incident ICMEs, connecting low coronal processes to ICME behavior in the Earth's neighborhood. This question drives the analysis and discussion presented in Chapters III and IV of this dissertation.

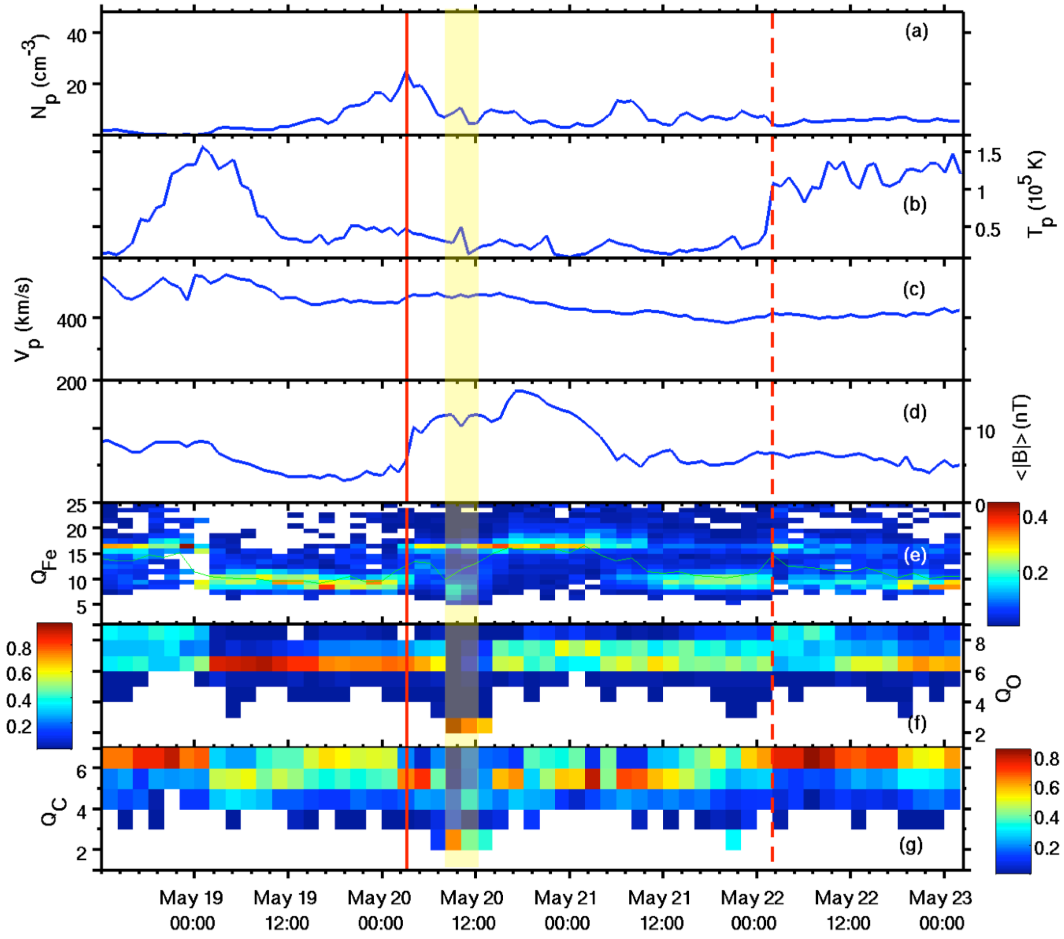

Figure I.10. Above is a multi-panel plot of ACE/*SWICS* observations of an ICME. The top panel is proton density (a), followed by proton temperature (b), proton speed (c), magnitude of magnetic field (d), followed by average charge states of iron (e), oxygen (f), and carbon (g). The start of the ICME is shown as the solid red line, and the end of the ICME is the dashed red line. The region within the ICME highlighted yellow is the cold plasma, identified by the low charge states of Fe, C, and O. [Lepri and Zurbuchen (2010)]

I.4.3. High Cadence Estimates of Filament Energetics Evolution in the Low Solar Corona:

Energy budgets are a prime starting point for understanding the physics of astrophysical phenomena. Quantifying the energy budget of CMEs is especially important due to their relevance to society and science (Section I.1). The energy budgets of CMEs include contributions from magnetic energy, kinetic energy, potential energy, thermal energy, energetic particles, and ionization energy (Murphy et al. 2011). Additionally, several studies over the past two decades have shown that heating plays a major role in the energy budget of CMEs (Akmal et al. 2001, Fillipov and Koutchmy 2002, Lee et al. 2009, Rakowski et al. 2007, Landi et al. 2010). CME models and simulations are seldom constrained by rigorous observations. Coupling between models and observations could lead to breakthroughs; however, models are not always built to predict many observables, and observations are often too limited to provide definitive answers. Bridging this gap between models and observations can help answer critical questions of processes leading up to eruption and through the CME evolution.

(a) In order to constrain models of CME birth and evolution, we need rigorous measurements of the evolution of the energetics of varying CME components over longer periods of time and at higher cadences.

In their analysis of the *Hinode*/EIS spectra of a CME core, Landi et al. (2010) concluded the core was made of two different plasma components moving coherently but with different temperatures, filling factors, and densities. This heterogeneity implies that performing averaged analysis over the largescale filament structures can introduce avoidable inaccuracies in subsequent measurements and over-simplify the physics involved, causing us to lose the nuances of the varying physical processes acting on the erupting filament.

(b) It is important that smaller regions of filamentary plasma be analyzed as separate entities while they are tracked at high cadences.

Estimates of how the different physical properties and energetics of CMEs evolves over time is the third open question explored in this dissertation. Points (a) and (b) mentioned above are goals incorporated into answering this question. This is addressed in Chapters III and IV of this dissertation.

I.5. Dissertation Map:

Coronal Mass Ejections (CMEs) are one of the largest manifestations of solar activity, consequential to an array of societal and scientific spheres, and studied through a diverse range of techniques and observations. This dissertation advocates the importance of, develops, and demonstrates techniques to study Earth-bound CMEs using an array of different instruments with different capabilities and measurement techniques. Three main scientific questions are posed, described in Section I.4.

What can we learn about processes that occur during CME initiation and acceleration via in-situ ICME observations?

In Chapter II of this dissertation we address this question through the detailed analysis of Interplanetary CMEs (ICMEs) which contain periods of anomalous heavy-ion charge state composition and peculiar ion thermal properties. Distinct intervals of significantly low abundances of fully-charged species of helium, carbon, oxygen, and nitrogen were uncovered. Defining ICME events with these intervals as 'Depleted ICMEs', 45% of all ICMEs measured by *ACE/SWICS* from 1998-2011 meet this criterion. Comparisons with CME model results were used to explore the connection between these ubiquitous ICME anomalies and the process of magnetic reconnection in the tail of CMEs.

How does the composition of filamentary plasmas evolve in the low solar corona?

In Chapter III, a case-study of an ICME observed at L1 is presented, and the ICME is traced back to the low solar corona using *SOHO/LASCO* and *STEREO/SECCHI* observations. The filament associated with this CME eruption is tracked in multi-wavelength *SDO/AIA* and *STEREO/EUVI* images in an attempt to monitor the behavior of its plasma at high cadence. The evolution of electron density and thermal structure are determined using an EUV absorption diagnostic technique, and kinematics are determined using synchronized multi-wavelength observations. These diagnostic results from remote-sensing observations are used to construct the ionization history of the CME core plasma in-order to connect to in-situ values after freeze-in.

How do the physical properties and energetics of different parts of CMEs evolve at high cadence in the low solar corona?

In Chapter III, high cadence measurements of density, temperature, and composition are presented for different plasma parcels tracked within the erupting filament. However, these measurements were based on column density and temperature determination from an existing diagnostic technique that neglected the He II emission contribution in the 304 Å channel from *SDO/AIA* measurements.

In Chapter IV a new diagnostic technique is presented that uses EUV and UV observations and notably allows for contributions from both absorption and emission to be considered. The diagnostic technique is applied to the filament eruption introduced in Chapter III and the results are compared. The results of this investigation allow for a more robust examination of the behavior of CME core dynamics at high cadence and determine the time evolution of the CME core energetics in the low solar corona.

CHAPTER II

Anatomy of Depleted Interplanetary Coronal Mass Ejections

Results presented in this chapter are published in the Astrophysical Journal | Vol 834 | # 2 article, 'Anatomy of Depleted Interplanetary Coronal Mass Ejections'

Results presented in this chapter are supported by analysis outlined in the Appendix

II.1. Preface:

In situ charge state measurements of oxygen and carbon have long been used as a diagnostic tool of the solar corona. For example, the O^{7+}/O^{6+} ratio is used in distinguishing between different solar wind types (Zurbuchen et al. 2000; Zhao et al. 2009, 2014). This is principally possible for two reasons. First, the oxygen charge states freeze-in close to the Sun 1.0–1.9 R_{SUN} for O^{7+} and O^{6+}. Second, oxygen is the most abundant element after hydrogen and helium (Grevesse & Sauval 1998, Grevesse et al. 2007), with measurements high enough and sufficiently well-resolved to be statistically relevant. Charge states of carbon ions can also be measured with comparable accuracy (von Steiger & Zurbuchen 2011), and C^{5+} and C^{6+} are predicted to freeze-in between 1.16 and 1.26 R_{SUN}, making carbon ion ratios an additional tool for robust solar wind diagnosis in the solar corona (Landi et al. 2012).

Figure I.7 (left) shows the schematic of the temperature profile of the corona, with the freeze-in location estimates for carbon, oxygen, silicon, and iron. Since carbon and oxygen charge states freeze-in in a similar region above the solar corona they are expected to have correlated behavior. Hence, we would expect the compound ratio **(C^{6+}/C^{5+})/(O^{7+}/O^{6+}) ("*R*" hereafter)** to be approximately constant after the freeze-in height in the low solar corona. Anomalies in this ratio in ICMEs were first reported by Cane & Richardson (2003), attributing them to potential instrumental effects. However, a recent study by Zhao et al. (2016) investigated the anomalies in R in the slow solar wind (v < 500 km s^{-1}), excluding ICME events. They found the anomalous slow wind to be denser and slightly slower than the average bulk slow wind, with approximately comparable charge state distribution, with the exception of a substantial decrease in the abundance of fully stripped ions as well as significantly lower ion temperatures. They suggest that this depletion of fully stripped ions in the slow wind could be a signature of magnetic reconnection between open field lines and closed coronal loops in the solar corona.

In-situ observations are gold mines of unique compositional traits consistently found in large populations of ICMEs that can be used as identifiers to isolate them from the ambient solar wind (Section I.3.2). In this study we examine the peculiar behavior of the R compound ratio measured during ICMEs by the *ACE*/SWICS instrument from 1998 to 2011. Similar to Zhao et al. (2016), we focus on the portion of solar wind measurements where the C^{6+}/C^{5+} ratios depart from their expected correlation with O^{7+}/O^{6+} by isolating instances of low R ratio. Instances of this deviation in in-situ solar wind data will be referred to as "**anomalous wind**." *This anomalous behavior is of interest because it* *challenges our understanding of the freeze-in process and holds potential clues to the acceleration of the solar wind and to physical processes that modified the plasma at its source in the corona*. We report the existence of the anomalous wind in a substantial population of ICMEs ("depleted ICMEs" hereafter) and study them in an effort to understand the processes occurring in the low corona during the onset of CMEs. We investigate the depleted ICMEs with three main goals: (1) to study the thermal and compositional structure of the depleted ICME plasma; (2) to scrutinize how these properties are different in the plasma surrounding the depleted ICME, and the ICMEs where this anomalous behavior is absent; (3) to understand the processes in CME initiation that shape this anomalous composition within the depleted ICME.

This chapter is organized in the following manner. Section II.2 describes the measurements used in this investigation. Sections II.3 introduces the compositional anomalies detected in the solar wind at L1 and their relationship with ICME observations. In Sections II.3.4.1 – II.3.4.2 present a comparative analysis of the plasma dynamics and plasma composition signatures of the different regions of the depleted ICME and the ICMEs where this anomalous behavior is absent. Section II.4 summarizes the major finding of this report and a potential hypothesis of processes at the coronal source of the depleted ICME are presented.

II.2. Overview of Measurements:

In this study, solar wind plasma data from 1998 February to 2011 August are considered. The analysis covered most of solar cycle 23 and a portion of the ascending phase of cycle 24. Plasma composition measurements from *ACE*/SWICS (described in Section I.3.2) are used. Two-hour cadence solar wind heavy-ion temperatures, speeds, and composition measurements are used from the *ACE*/SWICS data sets. This investigation also takes advantage of the recently released twelve-minute cadence solar wind proton data from the auxiliary channel on the SWICS instrument. These *ACE*/SWICS proton measurements are cross-calibrated and in good agreement with the *ACE*/SWEPAM and *WIND*/SWE proton measurements. The ionic charge states in the ICMEs that *ACE*/SWICS measures with statistically relevant resolution are considered: H^{1+}, He^{2+}, C^{4-6+}, N^{4-7+}, O^{5-8+}, Ne^{8-9+}, Mg^{8-10+}, Si^{9-12+}, S^{10-14+}, and Fe^{6-20+}. The ICME list compiled by Richardson & Cane (2004, 2010) from the *ACE* level 3 data product is used to identify ICMEs.

II.3. Observations:

II.3.1. Anomalous Wind:

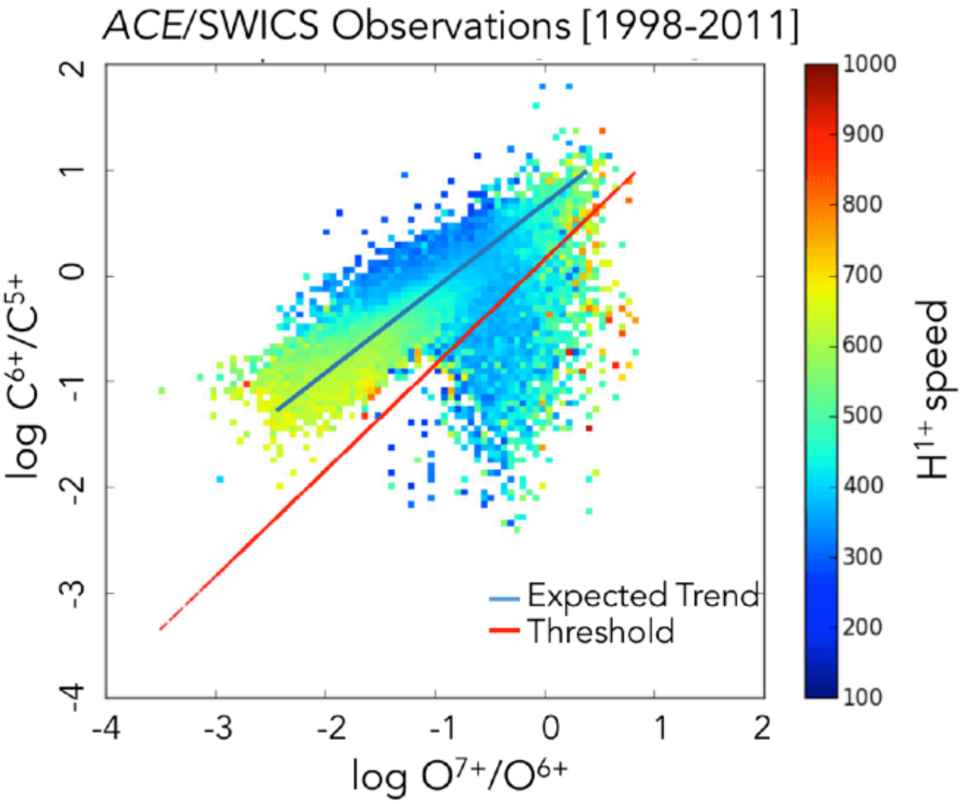

Figure II.1. C^{6+}/C^{5+} vs. O^{7+}/O^{6+} on logarithmic axes with proton speed on the third color-coded axis using *ACE*/SWICS measurements from 1998 to 2011. The blue line represents the expected trends between the carbon and oxygen charge states. The red line represents the threshold that isolates anomalous wind with low C^{6+}/C^{5+} density. All observations below the red line are anomalous solar wind observations.

Short and frequent intervals of anomalous wind (solar wind plasmas where C^{6+}/C^{5+} and O^{7+}/O^{6+} depart from a direct correlation) are observed between 1998 and 2011 in solar wind *ACE*/SWICS heavy-ion composition data (Zhao et al. 2016). Plotted in Figure II.1 is the logarithm of C^{6+}/C^{5+} (y-axis) and O^{7+}/O^{6+} (x-axis), with the average proton speed of measurements plotted as a color histogram in the z-direction. The main population in Figure II.1 shows the high correlation of the oxygen and carbon charge state ratios, with the blue line indicating a linear fit made between these two quantities. However, it is clear that *there is a leg that departs from the expected correlation where the plasma has high O^{7+}/O^{6+} values but a wide range of lower C^{6+}/C^{5+} values*. It is this leg that contains the anomalous wind, appearing during the anomalous slow wind events discussed by Zhao et al. (2016) and the depleted ICME events that will be described in detail in the following sections. Periods where the C^{6+}/C^{5+} and O^{7+}/O^{6+} density ratios defy the expected correlation (blue line) are separated by a threshold (red line). All measurements that fall below this red line are identified as the anomalous wind.

The threshold that separates the anomalous wind from the main body of solar wind observations was defined using the compound ratio R. The foremost criterion in the threshold choice was to isolate the largest pool of anomalous wind observations while excluding normal composition behavior. The threshold was chosen after following three approaches. (1) First, the average and standard deviation of the $-\log R$ of all the measurements between 1998 and 2011 are calculated, and the threshold is set as the average +2 standard deviations. (2) The second set of thresholds was obtained repeating the same procedure as (1) for each year, resulting in a set of annual thresholds. (3) The third set was determined by averaging all the thresholds obtained in (2), since their values turned out to be very similar. The threshold described in (3), where a single threshold value that is the average of the 14 annual values for 1998–2011, isolated the greatest population of anomalous wind. This represents 5.3% of solar wind measurements from 1998–2011 and is used in this analysis. Mathematically, the measurements where the following equation holds true are classified as anomalous wind:

$\log_{10}R < 0.15$ **Equation II.1**

where $R = (C^{6+}/C^{5+})/(O^{7+}/O^{6+})$

Figure II.2 shows a schematic of the different categories across which the anomalous wind exists, based on its proton speed. 48% of the anomalous observations have proton speeds less than 500 km s^{-1} (excluding all ICMEs, described in Zhao et al. 2016), and 51% of the wind coincides with ICMEs, which we investigate in this study. Only 1% of all anomalous observations coincide with non-ICME observations and have proton speeds greater than 500 km s^{-1}. These are excluded from this analysis. Additionally, 70% of the anomalous ICME observations have proton speeds less than 500 km s^{-1}, in addition to the anomalous non-ICME slow wind, as shown in Figure II.1.

While the current study isolates the anomalous wind using a technique different from that used by Zhao et al. (2016), both studies identify similar regimes of anomalous behavior: Zhao et al. (2016) found 49.4% of anomalous wind within ICMEs, 49.6% coinciding with slow non-ICME wind, and only 1% with fast non-ICME wind observations.

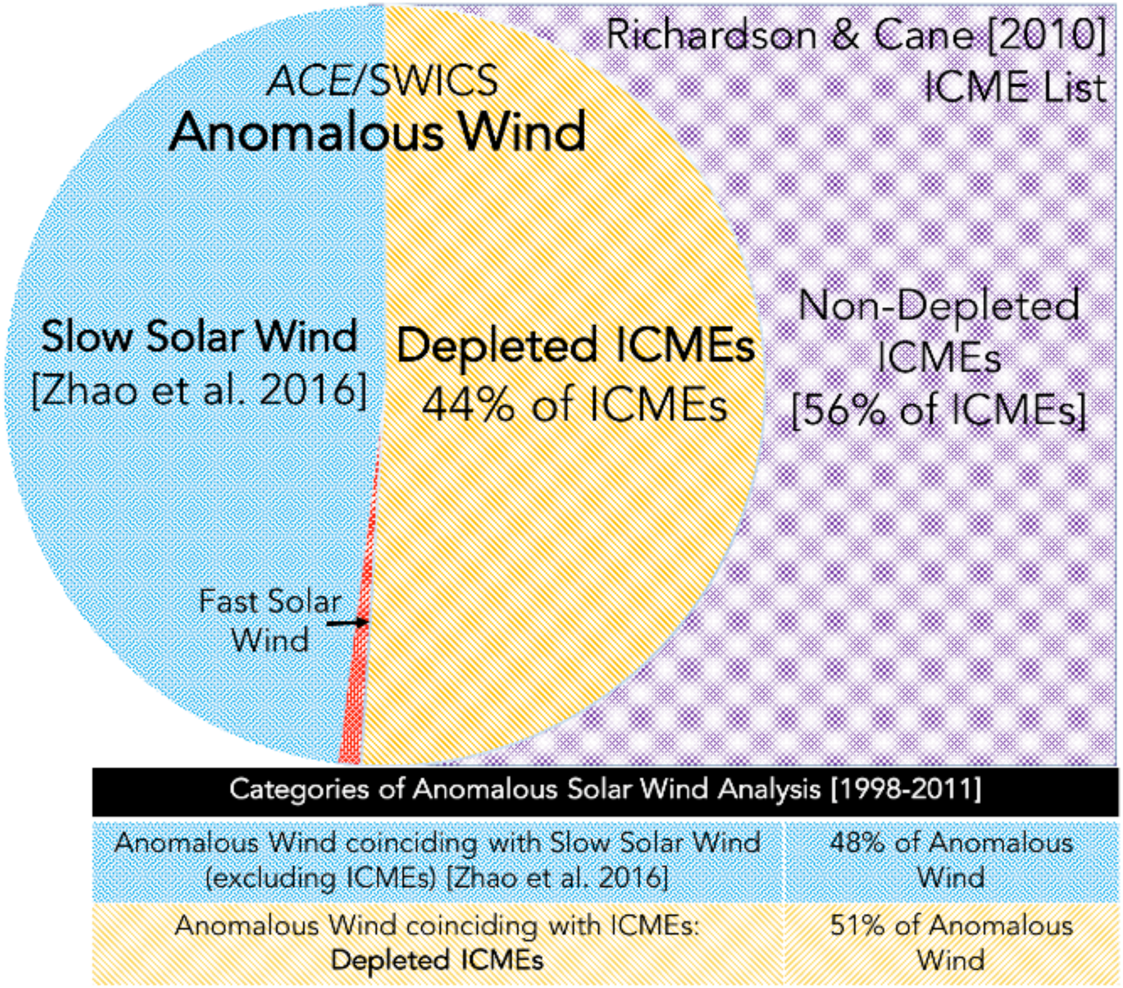

Categories of Anomalous Solar Wind Analysis [1998-2011]	
Anomalous Wind coinciding with Slow Solar Wind (excluding ICMEs) [Zhao et al. 2016]	48% of Anomalous Wind
Anomalous Wind coinciding with ICMEs: **Depleted ICMEs**	51% of Anomalous Wind

Figure II.2. Schematic depicting the different classes of anomalous wind. This consists mostly of slow proton speed wind (<500 km s^{-1}) (described in Zhao et al. 2016) and ICME observations (current study).

II.3.2. Depleted ICMEs and the Depletion Region:

Out of the 341 ICMEs reported by Richardson & Cane (2010) between 1998 and 2011, a total of 148 were found to contain periods of anomalous wind, representing approximately 44% of all ICMEs observed at 1 AU as seen in Figure II.2. These will henceforth be reported as "**depleted ICMEs**" and are the events under investigation in this report. The depleted ICMEs represent approximately 5% of all solar wind observations between 1998 and 2011. The number of depleted ICMEs is most abundant during the solar maximum years of 2000–2002, while no depleted ICMEs are reported from 2007 to 2009 during solar minimum.

Figure II.3 shows a depleted ICME from 2003 with the R ratio on the top panel followed by proton density, proton speed, and proton temperature. The proton temperature is calculated from the thermal speed reported by *ACE*/SWICS following Shearer et al. (2014) as:

$$T_{ion} = \frac{v_{th}^2 m_{ion}}{k_b}$$ **Equation II.2.**

where v_{th} is the thermal speed of the ion, m_{ion} is the mass of the ion, and k_{b} is the Boltzmann constant.

The five primary regions of the depleted ICME are marked 1–5 in the Figure II.3. Region 3 is called the "**Depletion Region**," and represents the portion of the depleted ICME where the anomalous wind is predominantly detected. For example, in the top panel of Figure II.3 the R ratio is predominantly below the black threshold line (M = 0.15) in the Depletion Region. Regions 2 and 4 indicate the remainder of the depleted ICME, i.e., the region of the depleted ICME where the anomalous wind is absent. Regions 1 and 5 represent the plasma within 6 hours before and 6 hours after the depleted ICME, respectively, and correspond to the unperturbed solar wind before and after the CME event. In order to ensure this wind is unperturbed we exclude statistics of the 20% of depleted ICMEs where we detected adjacent ICMEs in regions 1 and 5, from the analysis of these two regions.

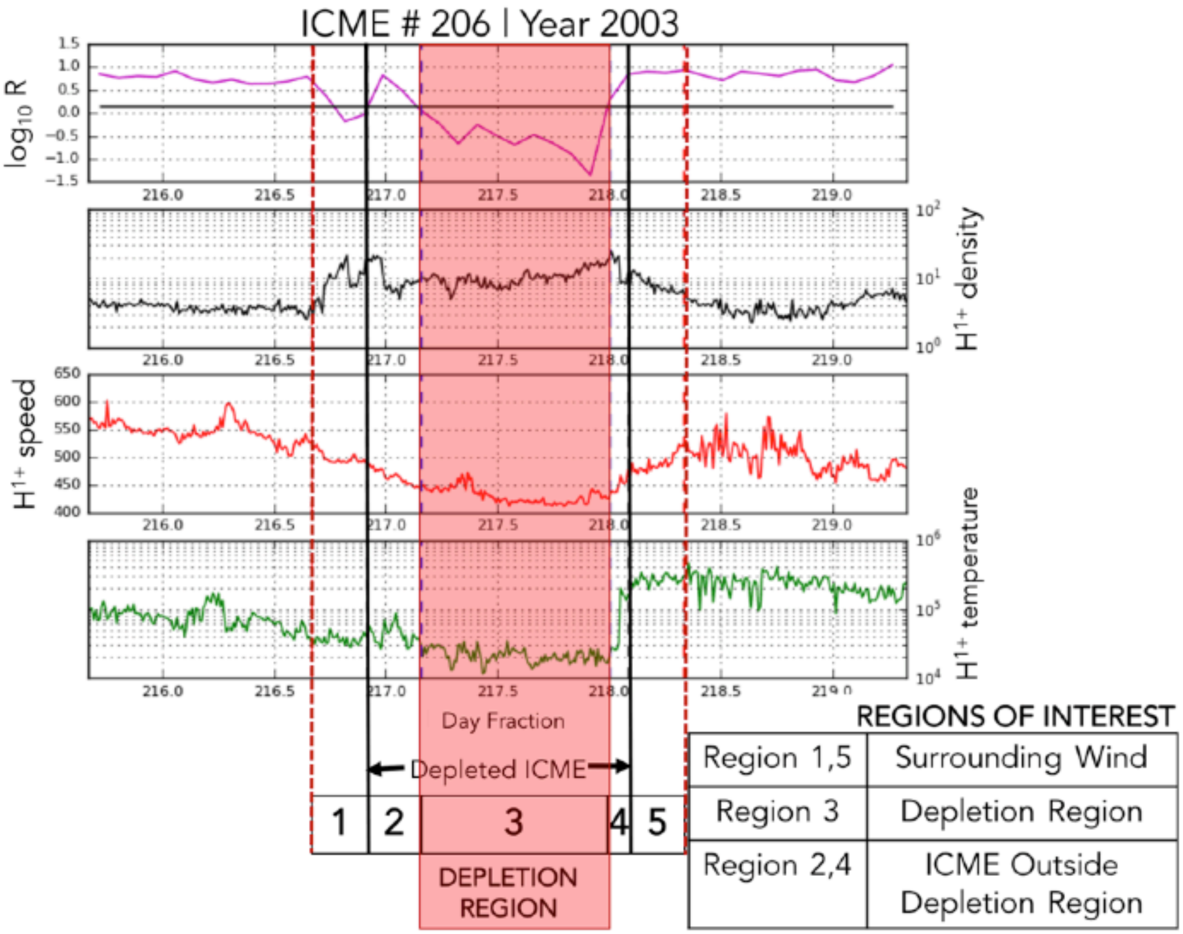

Figure II.3. A depleted ICME that intercepted *ACE*/SWICS between 2003 August 4–6, reported by Richardson & Cane (2010). The top panel shows $\log_{10} R$, with the threshold = 0.15 denoted by the horizontal black line. The successive panels show the proton parameters: density, speed, and temperature. The depletion region is highlighted in red (Region 3), remaining ICME labeled as Regions 2 and 4, and the surrounding wind labeled as Regions 1 and 5.

The location and size of the Depletion Region within the depleted ICME was variable across the 148 depleted ICME cases between 1998 and 2011. 40% of the depleted ICMEs had associated magnetic clouds compared to 30% of all ICMEs with associated magnetic clouds, according to the Richardson & Cane (2010) magnetic cloud list.

II.3.3. Relationship of the Depleted ICME with Common ICME Signatures:

The alpha-to-proton ratio is perhaps the oldest composition indicator used for ICME identification. Hirshberg et al. (1971) found regions where He^{2+}/H^{1+} values were enhanced following interplanetary shocks, compared to their normal solar wind values. The enhancement in He^{2+}/H^{1+} was confirmed as a sufficient signature of ICMEs by studies such as Richardson & Cane (2004); however, the enhanced He^{2+}/H^{1+} is not a necessary signature. The ratio of $O^{7+}/O^{6+} > 1$ was additionally found to be a sufficient indicator in some populations of ICMEs (Henke et al. 2001; Zurbuchen et al. 2003). CME modeling efforts by Lynch et al. (2011) predicted an enhanced ring of O^{7+}/O^{6+} around the core in their simulation of the flux cancellation initiation model (described in Reeves et al. 2010). Additionally, enhanced iron charge states have also been established as excellent indicators of ICMEs in in situ observations (Lepri et al. 2001; Lepri and Zurbuchen 2004). The Lynch et al. (2011) CME simulations also found mean high iron charge states in a similar ring around the core.

Studies have attributed enhanced He^{2+}/H^{1+} ratios to possible large-scale transport of helium ions by powerful CME explosions (Neugebauer et al. 1997), while enhanced iron charge states and high O^{7+}/O^{6+} compared to normal solar wind have been described as signatures of high-temperature reconnection material supplied to the CME during eruption. The depleted ICMEs and their corresponding Depletion Regions respond to these common ICME signatures (summarized in Zurbuchen and Richardson 2006) as follows:

A. Depleted ICME compared to its surrounding plasma:

The He^{2+}/H^{1+} ratio does not change significantly on average between the depleted ICME (Regions 2, 3, and 4) and its surrounding plasma (Regions 1 and 5). On the other hand, the O^{7+}/O^{6+} ratio and $\langle Q\rangle_{Fe}$ show significant enhancement in the depleted ICME compared to its surrounding plasma in a majority of the depleted ICME cases. Such enhancement is not unexpected, and similar to conclusions drawn for ICMEs by existing in situ and modeling studies (discussed above) that find strong evidence of heightened electron temperatures in CMEs in these parameters. However, the behavior of the He^{2+}/H^{1+} abundances in depleted ICMEs lack the expected enhancement observed by previous ICME studies.

B. Depletion Region compared to the remaining depleted ICME:

The He^{2+}/H^{1+} ratio is lower in the Depletion Region (Region 3) compared to the remaining plasma in the depleted ICME (Regions 2 and 4). Again, the O^{7+}/O^{6+} ratio and $\langle Q \rangle_{Fe}$ are further enhanced in the Depletion Region compared to the remaining plasma of the depleted ICME.

C. Depleted ICME plasma outside the Depletion Region compared to the non-depleted ICMEs:

He^{2+}/H^{1+}, O^{7+}/O^{6+}, and $\langle Q \rangle_{Fe}$ do not demonstrate any significant trends in the difference between their behaviors in the depleted ICME plasma outside the Depletion Region (Regions 2 and 4) and the non-depleted ICMEs.

While a majority of the depleted ICMEs demonstrate strong signatures of elevated plasma freeze-in temperatures (as discussed in (A)), our findings in (B) and (C) show that the signatures are strongest in the Depletion Region within the depleted ICMEs. Additionally, based on O^{7+}/O^{6+} and $\langle Q \rangle_{Fe}$, without the Depletion Region, the depleted ICMEs are indistinguishable from the non-depleted ICMEs. The significance of low helium/proton abundances in the Depletion Region is discussed in Section II.4.

II.3.4. Comparison of Different Regions of Interest:

Presented here is a comparative analysis of the in-situ properties of the five regions of the 148 depleted ICMEs along with the 193 non-depleted ICMEs using *ACE*/SWICS plasma composition measurements. *Since these composition measurements are* *determined by plasma properties near the Sun, trends in the ion thermal and compositional properties are useful to determine the conditions in the low solar corona where the depleted ICMEs and Depletion Regions were initiated, and additional processes that might have contributed to these anomalies.*

The three modes of comparison are as follows: (1) depleted ICME (Regions 2, 3, 4) with plasma surrounding the depleted ICME (Regions 1, 5), (2) Depletion Region (Region 3) with the remaining depleted ICME (Regions 2, 4), and (3) depleted ICME outside the Depletion Region (Regions 2, 4) with the non-depleted ICMEs. Comparing the plasma properties in these regions allows for inferences on the structure of the depleted ICMEs and the Depletion Region within, detailed statistics of which are provided in the Appendix of this dissertation. The key highlights of our findings are summarized here.

II.3.4.1. Anatomy of the Depleted ICME:

a. The proton temperature was lower in the depleted ICME compared to the plasma around it, consistent with previous studies that identify proton temperature depressions among the most prominent features of ICMEs (e.g. Richardson & Cane 1995, Mulligan et al. 1999), attributing the behavior to CME expansion during eruption and propagation through the heliosphere.

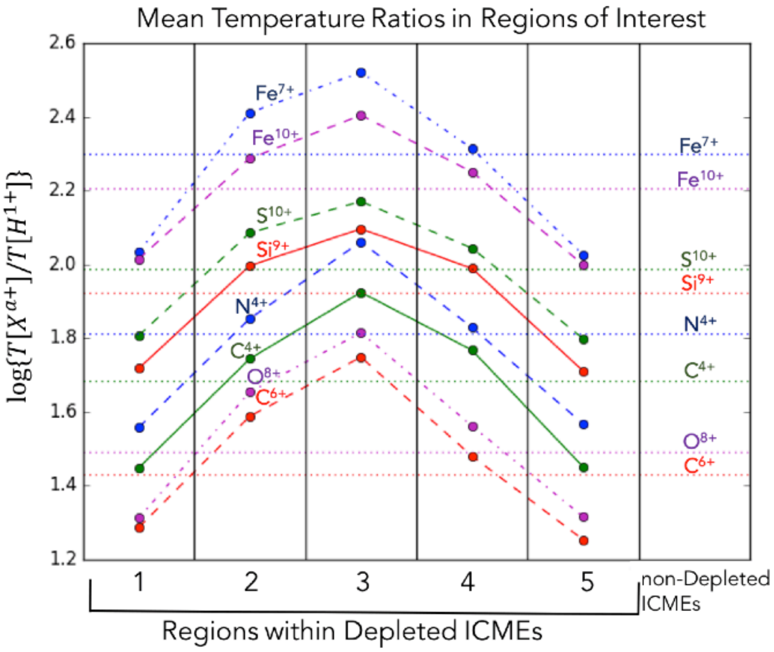

Figure II.4. Panels 1–5 show the mean values of the relative ion-proton temperature ratio of Fe$^{7,10+}$, S^{10+}, Si^{9+}, N^{4+}, C^{4+}, O^{8+}, and C^{6+} in five regions of interest within the depleted ICMEs. The corresponding mean relative ion-proton temperature ratios in non-depleted ICMEs are represented with horizontal dotted lines across all panels.

b. The absolute ion kinetic temperatures of a majority of heavy ions were also depressed in the depleted ICME compared to the plasma surrounding it, reiterating thermodynamic cooling due to CME plasma volumetric expansion.

c. Figure II.4 shows the mean values of the logarithm of the relative ion-proton temperature ratios ($T[X^{N+}]/T[H^{1+}]$) in the five regions of the depleted ICMEs as well as the non-depleted ICMEs for several ions. The ion/proton temperature ratios are higher in depleted ICMEs compared to plasma in the surrounding wind. *This is conceivably a signature of additional heating at the source region of the depleted ICME.* We suggest this heating competes with the cooling due to adiabatic expansion as discussed in (a) and (b) and surpasses it, resulting in the higher ion/proton temperature ratios.

d. The ionization distributions of Ne, Si, S, and Fe were skewed toward higher charge states in the depleted ICME compared to the surrounding wind, providing further evidence of elevated electron temperatures at the depleted ICME source.

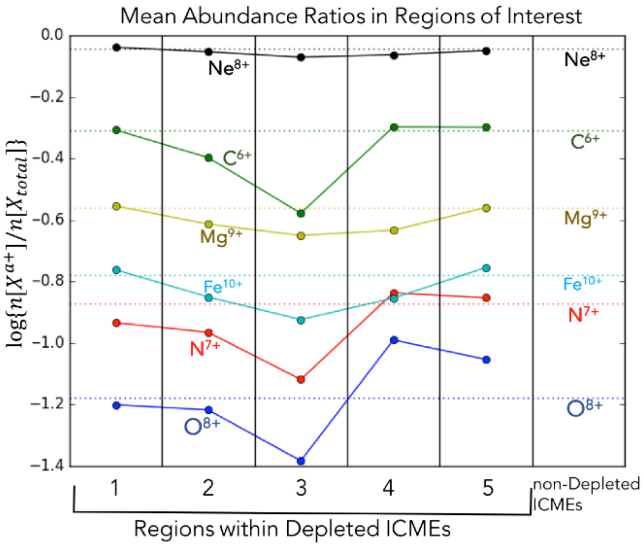

Figure II.5. Panels 1–5 show the mean values of the logarithm of the ratio of the abundance of [C^{6+}, N^{7+}, O^{8+}] (fully stripped) and [Ne^{8+}, Mg^{9+}, Fe^{10+}] to the total abundances of their respective elements in five regions of interest within the depleted ICMEs. The corresponding mean abundance ratios in non-depleted ICMEs are represented with horizontal dotted lines across all panels.

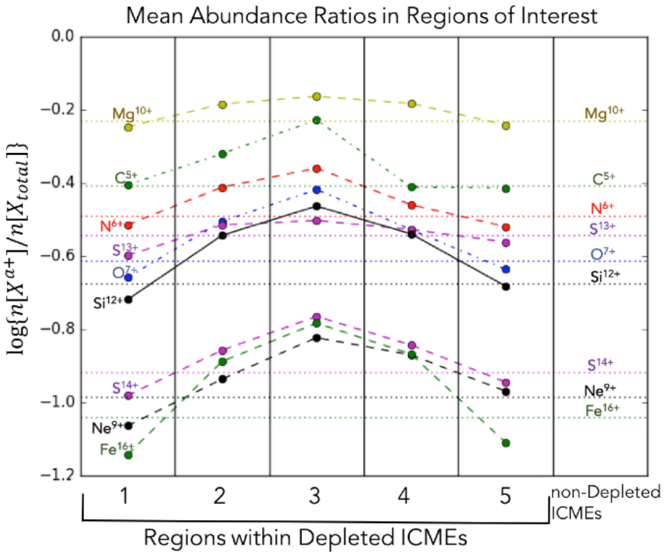

Figure II.6. Panels 1–5 show the mean values of the logarithm of the ratio of the abundance of Mg^{10+}, S$^{13\text{-}14+}$, Si^{12+}, C^{5+}, N^{6+}, O^{7+}, Ne^{9+}, and Fe^{16+} to the total abundances of their respective elements in the five regions of interest within the depleted ICMEs. The corresponding mean abundance ratios in non-depleted ICMEs are represented with horizontal dotted lines across all panels.

II.3.4.2. Anatomy of the Depletion Region:

Figures II.5 and II.6 show the mean values of the logarithm of the ratio of the abundance of the charge states of several ions to the total abundance of their respective elements ($n[X^{N+}]/n[X]$) in the 5 regions of the depleted ICMEs as well as the non-depleted ICMEs. Standard deviations are not depicted in Figures II.4 - II.6 due to their large values; instead, the distributions of the ion properties were analyzed. Figure II.7 summarizes our findings of the percentage of depleted ICMEs in which the ratio of the abundance of the charge states of an ion to the total abundance of its element [X^{N+}/X] are enhanced/depleted in the Depletion Region (Region 3) compared to the remaining plasma in the depleted ICME (Regions 2 and 4).

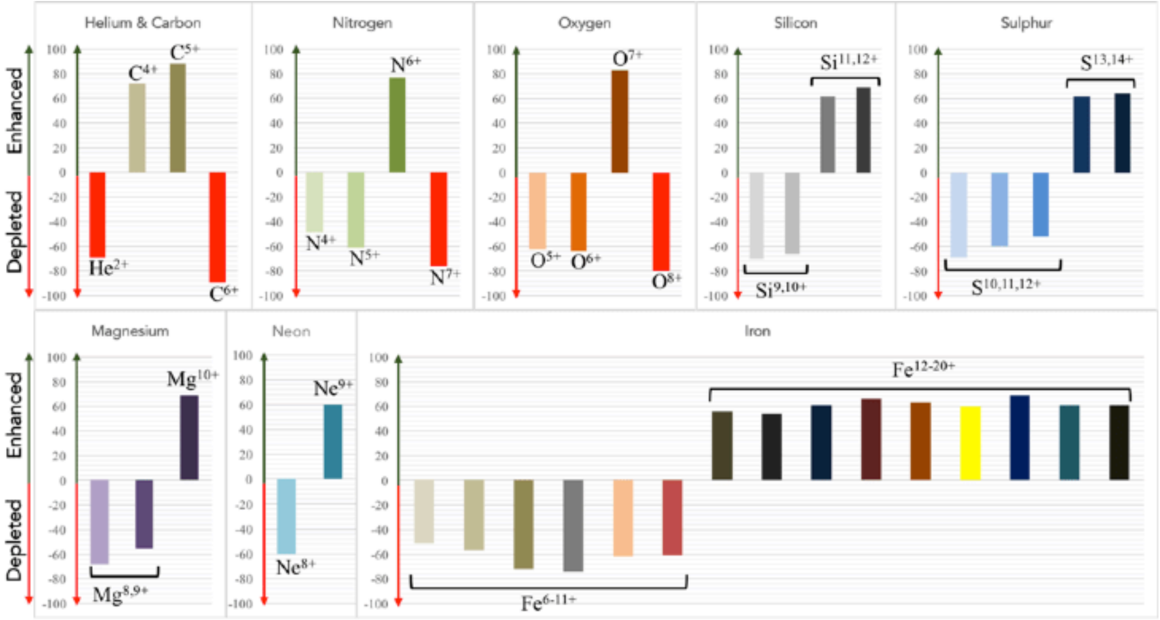

Figure II.7. In the above schematic, each bar represented the percentage of depleted ICMEs in which the ratio of the abundance of the charge states of an ion to the total abundance of its element [X^{n+}/X] are enhanced/depleted in the Depletion Region (Region 3) compared to the remaining plasma in the depleted ICME (Regions 2 and 4).

Figures II.5-II.7 reveal distinct ordering in the behavior of the ionic charge states in the Depletion Region compared to the remaining plasma of the depleted ICME. We summarize them here.

(1) The abundance ratios of the lower charge states of nitrogen (N^{4-5+}), oxygen (O^{5-6+}), neon (Ne^{8+}), silicon (Si^{9-10+}), sulphur (S^{10-12+}), and iron (Fe^{6-11+}) to the total abundance of their respective elements, are slightly lower in the Depletion Region compared to the remaining depleted ICME plasma. Mean values of these abundance ratios for Ne^{8+}, Mg^{9+}, and Fe^{10+} are shown in Figure II.5.

(2) The abundance ratios of the higher charge states (up to the second highest charge states) of nitrogen (N^{6+}), oxygen (O^{7+}), neon (Ne^{9+}), silicon (Si^{11-12+}), sulphur (S^{13-14+}), and iron (Fe^{12-20+}) to the total abundance of their respective elements, are slightly higher in the Depletion Region compared to the remaining depleted ICME plasma. Mean values of the abundance ratios for several of these ions are shown in Figure II.6.

(3) The abundance ratios of the fully stripped charge states of helium (He^{2+}/H) (see Section II.3.3), carbon (C^{6+}/C_{total}), oxygen (O^{8+}/O_{total}), and nitrogen (N^{7+}/N_{total}) are heavily depleted in the Depletion Region compared to the remaining ICME plasma by factors ranging from 1.25–1.7 on average. This is the most significant difference and the stark depletion of fully stripped ions compared to other ions in Region 3 is seen in Figure II.5.

(4) From Figures II.4-II.6 we can also infer that the ionic and compositional properties of the depleted ICMEs outside the Depletion Region (Regions 2 and 4) are similar to the non-depleted ICMEs.

II.4. Discussion:

The Depletion Region has a unique compositional anatomy, with depleted fully stripped ions as its most distinct feature. This section presents an investigation of the feasibility of some scenarios that could *preferentially remove the fully stripped ions from this plasma within depleted ICME, leaving its remaining composition mostly intact.*

The analysis presented in the previous sections suggests that *the signatures of thermal heating are most intense in the Depletion Region*, i.e., the ion/proton kinetic temperature ratios are higher and the ion abundances of the high charge states of Ne, Si, S, and Fe are further enhanced in the Depletion Region (Region 3) compared to the remaining plasma in the depleted ICME (Regions 2 and 4). Additionally, based on the thermal and compositional parameters summarized in Sections II.3.3 and II.3.4 it can be concluded that *the depleted ICME outside the Depletion Region is indistinguishable from all other ICMEs.* This means the Depletion Region plasma at the CME origin was subject to a process that did not affect the rest of the depleted ICME plasma. Also, the Depletion Region must have been formed near or beyond the freeze-in height because at coronal temperatures, ongoing ionization would replenish the fully stripped He, C, N, and O, which we do not see. This implies the density is low enough to shut down ionization in the Depletion Region source.

Zhao et al. (2016) proposed reconnection between a closed field line and an open magnetic loop in the corona as a possible scenario to create anomalous wind parcels, which had significantly depleted C^{6+}, similar to our Depletion Region. Since magnetic reconnection (Section I.4.1) plays a significant role in CME eruptions, we consider the possibility of a reconnection region being the source of the Depletion Region plasma based on the following arguments:

a. Magnetic reconnection can generate significant thermal energy, which could cause the rapid heating in the Depletion Region.

b. Reconnection in current sheets that trail CMEs can occur near the freeze-in regions of various ions, thus potentially acting on plasma with sufficiently low density to be beyond the freeze-in point.

The question arises whether our knowledge of processes within the reconnection region can explain the depletion of He^{2+}, C^{6+}, N^{7+}, and O^{8+} in the Depletion Region. In order to carry out a preliminary investigation of this we consider two state-of-the-art CME simulations: (1) Manchester (2003) presented a 2.5D MHD simulation of a CME eruption resulting from magnetically sheared arcades using the ZEUS-2D code (Stone & Norman 1992a, 1992b). The current sheet extends between 1.18–1.3 R_{SUN} and shows true tearing mode instabilities with magnetic islands. (2) Manchester et al. (2004) presented a 3D MHD model of the time-dependent generation and propagation of an Earth-bound CME using the Block Adaptive Tree Solar-Wind Roe Upwind Scheme (BATS-R-US) code (see Powell et al. 1999; Groth et al. 2000 for description). The current sheet in this simulation extends between 3 and 7 R_{SUN}. The current sheet in the Manchester (2003) simulation is formed close to the expected freeze-in region, and that in the Manchester et al. (2004) simulation is formed well beyond the freeze-in region, providing us with a range of qualitative estimates for the location above the corona we expect the Depletion Region to be formed. Instants in both CME eruptions were chosen where the current sheet appeared to be well formed with minimum thickness, strong outflows, and substantial length.

We proposed that in order for the fully stripped ions to be depleted in a large fraction of ICMEs, these ions were either:

(1) accelerated out of the plasma by a process in the reconnection region; we examined the behavior of an energetic proton beam produced in the reconnection region to investigate this possibility; or

(2) left behind from the plasma parcel from the very beginning due to a differential pick-up ion scenario; we examined the findings of Drake et al. (2009) to investigate this possibility.

An energetic beam created in the reconnection region that favored the acceleration of fully stripped charge states over all other charge states would explain the compositional anatomy we see in the Depletion Region. Protons are the most abundant element in the solar atmosphere and possess the greatest potential to impart substantial momentum to the ions. Energetic electrons, on the other hand, are too light to provide such momentum, and other heavy ions are too few to have significant effect on the plasma. Hence, we propose that the energetic protons would Coulomb collide with the fully stripped ions and accelerate them out of the plasma parcel while the energetic electrons could ionize the plasma, thus depleting the lower ionization states and increasing the higher ionization states of all elements, as observed.

The Coulomb collision cross-section between two charged particles is given by:

$$\sigma_{ss'}(V,\chi) = \frac{e_s^2 e_{s'}^2}{64\pi^2 \epsilon_0^2 \mu_{ss'}^2 V^4 \sin^4(\chi/4)}$$

Equation II.3

where $\sigma_{ss'}$ is the Coulomb cross-section, V is the relative velocity between the particles, χ is the scattering angle, $\mu_{ss'}^2$ is the reduced mass, and e_s and $e_{s'}$ are the charges of the two particles. It is inferred from the above equation that the Coulomb cross-section for proton–ion collisions is mainly dependent on the square of the charge of the particle the proton is colliding with. This implies that a fully stripped ion (e.g., C^{6+}) would have a Coulomb cross-section only ~30% greater than the second highest charge state (e.g., C^{5+}). Ignoring the factor of scattering angle and reduced mass, Coulomb collisions between the protons of an energetic beam and the plasma alone could not explain the large depletion of fully stripped ions compared to other ions in the Depletion Region.

How energetic are protons in CME current sheets? Recent studies have attempted to estimate how energy is partitioned in solar eruptive events in order to provide useful constraints on our understanding of energy release processes during eruptions (e.g., Emslie et al. 2004, 2005, 2012). However, estimates of proton energy within the reconnection current sheet have proven difficult to determine. Since current sheets can extend as far as 10 R_{SUN} long, proton energies are expected to vary greatly along its length. While in situ and remote-sensing capabilities do not provide us with reliable magnetic field and density measurements in CME current sheets in the low solar corona, various modeling efforts have attempted to describe the conditions in which CMEs are initiated and evolve.

The proton kinetic energy profile in the current sheet is a function of the reconnection jet outflow speed, which is predicted to be a fraction of the Alfvén speed of the plasma, and is computed as follows (Karimabadi et al. 2013 and references therein):

$$E_{proton} = \frac{\frac{1}{2} m_p \alpha^2 |B|^2}{\mu_o \rho} \qquad \textbf{Equation II.4}$$

with, $v_p = \alpha \, V_{Alfvén}$. Here, m_p is the proton mass, $|B|$ is the magnetic field strength, μ_o is the magnetic permeability constant, ρ is the density of the local plasma, v_p is the proton speed, $V_{Alfvén}$ is the Alfvén speed, and α is the fraction of the Alfvén speed which can be used to calculate the jet outflow speed. $|B|$ and ρ estimates from the Manchester (2003) and Manchester et al. (2004) CME models are used.

Dissent arises in the factor α since different CME theoretical and modeling studies predict different factors for the relationship between the Alfvén speed and reconnection jet outflow speed. For instance, Karimabadi et al. (2013) estimated outflow speeds to be typically less than the Alfvén speed. Lynch et al. (2016) analyzed the properties of a reconnection current sheet of a magnetic breakout-initiated CME finding outflow velocities to be of the order of the Alfvén speed using a globally averaged Alfvén speed of ~1400 km s^{-1}. In the previous study (Lynch and Edmondson 2013), where they described the modeling of the evolution of the CME using the Adaptively Refined MHD Solver (ARMS) code (DeVore and Antiochos 2008), they similarly found Alfvénic flare reconnection jets providing ≥1500 km s^{-1} outflows, corresponding to $\alpha \sim 1$. However, the Lynch and Edmondson (2013) study also reported variation in localized reconnection rates over their current sheet, with Alfvénic reconnection jet outflows reaching ~4000 km s^{-1} during the impulsive phase of the flare reconnection and corresponding to $\alpha \sim 3$.

Figure II.8 shows proton energy estimates of the two currents sheets formed beyond and near the ionization freeze-in regions respectively. The top plot of Figure II.8 shows the proton energy variation as a function of height using current sheet estimates from the Manchester et al. (2004) CME eruption simulation for $\alpha = (0.5, 1, 2, 3, 4, 5)$. Similarly, the bottom plot of Figure II.8 shows the proton energy variation as a function of height in the current sheet from the Manchester (2003) CME eruption simulations for $\alpha = (0.5, 1, 2, 3, 4, 5)$. Notice that the bottom plot has a distinct proton energy peak while the top does not. This is because the current sheet in the Manchester et al. (2004) simulation is formed higher in the corona by which point the proton energy has already peaked. On the other hand, the current sheet in the Manchester (2003) simulation forms lower in the corona such that the proton energy peaks within the current sheet. Large proton energies are possible at high α values, which potentially correspond to localized transient flows. However, (1) more analysis is required to understand how proton beam energies relate to differential Coulomb collisions of fully stripped ions versus all other charge states of ions, and (2) further work is needed to better constrain the factor α in reconnection current sheets. These are beyond the scope of the study presented here.

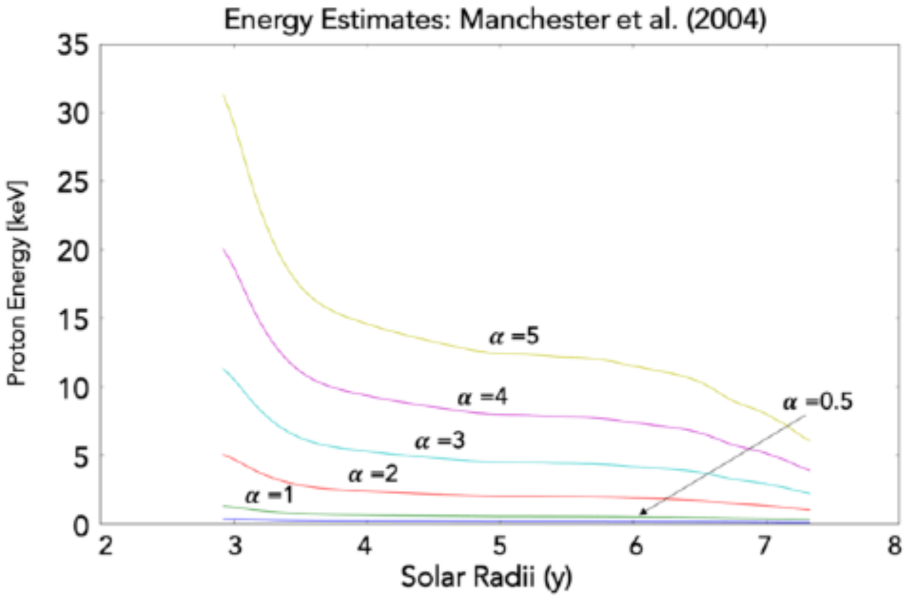

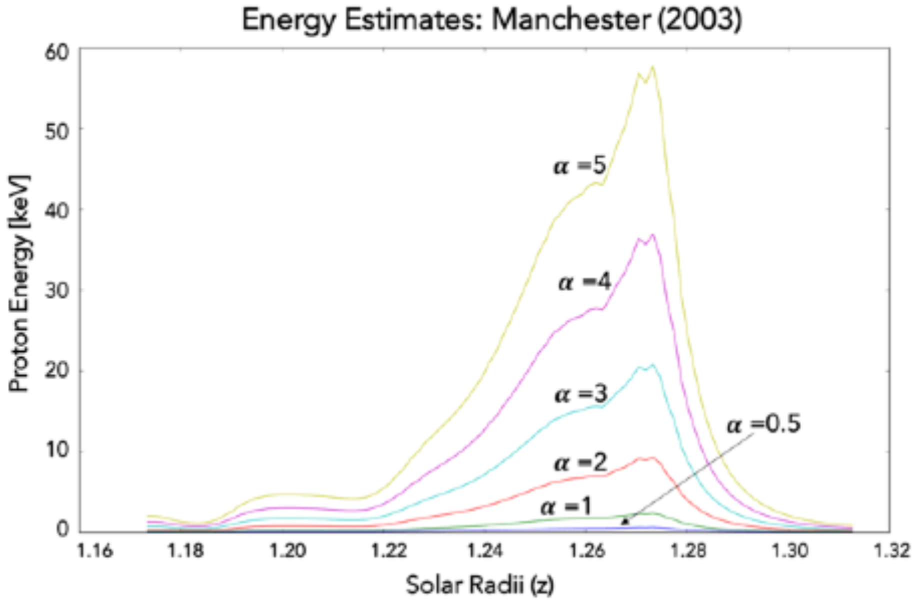

Figure II.8. (Top) Proton energy estimates for different values of α are plotted as functions of solar radius for the current sheet that forms in the CME simulation described in Manchester et al. (2004). (Bottom) Proton energy estimates are plotted for current sheet formed in the arcade eruption model of Manchester (2003). The radial distance is normalized to the model of Manchester et al. (2004). Plots are made for several values of α.

The second hypothesis proposed for the depletion of fully stripped ions in ICMEs involved the possibility that those ions were left behind from the plasma due to some process occurring during a reconnection event. Drake et al. (2009) explored the question of ion heating in impulsive flares by means of simulations and analytical models. They present the following threshold to investigate what happened to individual ions entering the reconnection region:

$$\frac{m_i}{m_p z_i} > \frac{10}{\pi\sqrt{2}B_{ox}}\sqrt{8\pi\left(T_e + T_p\right)n}$$ **Equation II.5**

where, m_i is the mass of the ion, z_i is the charge of the ion, m_p is the mass of the proton, B_{ox} is the reconnecting field strength, n is the plasma density, T_e and T_p are electron and proton temperatures respectively. They proposed that during magnetic reconnection, ions with mass/charge exceeding the threshold given by Equation II.5 behave as pick-up ions that is, they find themselves at rest in the high-velocity magnetized plasma and as a result gain a convective velocity equivalent to the reconnection exhaust speed, and experience significant heating, while ions with mass/charge below the threshold do not become heated. The scenario where this threshold could be used to distinguish the peculiar behavior of the fully stripped ions compared to all other ions is considered. There are two open questions in applying the Drake et al. (2009) threshold picture to the Depletion Region composition. (1) If the threshold is such that all ions but the fully-stripped one are picked up and experience heating, do they also get accelerated differently? (2) Moreover, if the threshold that differentiates fully stripped behavior from the behavior of other charge states is met, we would expect to see the fully stripped ions less heated than all other ions. Is this concurrent with measurements?

The temperature, density, and magnetic field estimates from the Manchester et al. (2004) and Manchester (2003) CME simulations were employed to calculate the threshold of Equation II.5. Computations were made assuming completely ionized hydrogen plasma with equal electron and proton temperatures. In the case of the Manchester et al. (2004) simulation, the current sheet region between 2.9 and 3.4 R_{SUN} had mass/charge threshold above and sufficiently close to 2, such that the fully stripped ions were the only ones that were not picked up in the reconnection exhaust. This implied that CME plasma originating from reconnection in this region could have produced fully stripped ions that were less heated while all other charge states behaved as pick-up ions and experienced more heating.

In addition to being less heated, if the fully stripped ions were also less accelerated than the other charge states in the plasma, we would expect to see no fully stripped charge states in the Depletion Region. Though in abnormally low quantities, we do observe fully stripped ions. This could be a product of ionization of the second highest charge states of their respective elements before freeze-in.

No significant trend was seen in *ACE*/SWICS measurements of ion temperatures that suggested that fully stripped ions were systematically cooler than the other charge state of their respective ions within the Depletion Region. The high temperatures of the fully stripped ions are justified within the proposed hypothesis, since they would have been picked-up and heated before being ionized into their fully stripped state. However, in order to confidently attribute the Depletion Region to this theory, an understanding of how the low mass/charge and high mass/charge ions get accelerated differently is necessary.

As the CME propagates outward into the interplanetary medium, it continues to reconnect with other magnetic field lines, hence morphing out of the exact ordering seen at its birth. However, *somehow the compositional structure of the Depletion Region is preserved, neither changed by reconnection nor diluted by mixing*. This happens because the Depletion Region plasma must have been created in regions close enough to or above the freeze-in heights of most major ions. This ensures the peculiar composition of the Depletion Region is maintained with its distinction from the remaining ICME plasma preserved. The reconnection that punctuates the tumultuous journey of the ICME to the *ACE*/SWICS instrument reorders the plasma and explains the finding that the Depletion Region has no distinct ordering in where it is located within the depleted ICME by the time it reaches L1. However, these reconnection events do not affect the magnetic structure of the Depletion Region since the Depletion Region plasma does not mix with the plasma in the rest of the ICME.

The anomalous events in the slow wind reported by Zhao et al. (2016) represented ~11% of all slow wind measured by the *ACE*/SWICS instrument. The relatively small percentage of slow wind in which the anomalous signatures are observed is not unexpected as recent studies have found that reconnection is not the only mechanism responsible for the origin of the slow solar wind (Stakhiv et al. 2015), and additionally the different magnetic field configurations vary across different slow wind sources. This means that certain configurations might not be able to harness the sufficiently energetic proton beams that we expect to drive out the fully stripped ions seen in the anomalous slow wind or create a threshold low enough to deplete only the fully stripped ions in the Drake et al. (2009) scenario. In the investigation presented in this chapter, we find similar anomalous wind within Depletion Regions that exists in ~44% of all ICMEs between 1998 and 2011; thus, these anomalous plasma packets are much more ubiquitous than in the slow wind.

It is possible that the Depletion Region would be a defining characteristic of many more ICMEs. The Depletion Region may go unobserved for two reasons. (1) In the current analysis, anomalous wind observations in ICMEs that were shorter than three continuous data points in extent were not qualified as Depletion Regions, consequently classifying some ICMEs with shorter and sporadic anomalous points as non-depleted ICMEs. (2) Also possible is that smaller filling factors of Depletion Region plasma within the entire ICME results in the Depletion Regions going undetected by the *ACE*/SWICS spacecraft, rendering our counts of depleted ICMEs an underestimate.

CHAPTER III.

Tracking Filament Evolution in the Low Solar Corona using Remote-sensing and In-situ Observations

Results presented in this chapter are published in the Astrophysical Journal | Vol 860 | # 1 article, 'Tracking Filament Evolution in the Low Solar Corona using Remote Sensing and In Situ Observations'

III.1. Introduction:

A filament eruption is studied using extensive multi-instrument analysis of remote-sensing and in-situ observations in an attempt to piece together the complete evolution of filamentary plasma from its birth through L1. In multi-wavelength *SDO/AIA* images, three plasma parcels within the filament are tracked at high-cadence along the solar corona. The Landi and Reale (2013) diagnostic technique is applied to the filament material travelling along the three chosen trajectories to compute the column density and temperature evolution in time. Kinematics of the filamentary material are estimated using STEREO/*EUVI* and STEREO/*COR1* observations. The Michigan Ionization Code uses inputs of these density, temperature, and speed profiles for the computation of ionization profiles of the filament plasma.

Through this investigation, this chapter explores the open questions discussed in Section I.4.2-1.4.3. (1) How do dynamics and kinematics of filaments evolve in the low solar corona? (2) What is the ionization history within filament plasmas before freeze-in? and (3) How can we use measurements of the ionization history to reconcile the disconnect between in-situ and remote observations of filaments? A possible framework is presented that comprises of remote-sensing observations, in-situ measurements, an ionization model and diagnostic techniques to study solar transients. This framework can utilize current and future observational capabilities.

Section III.2 describes the multi-instrument in-situ and remote-sensing observations of the filament eruption used to execute this study and how they were used to connect the same event at L1 and at the Sun. Section III.3 describes the technique to track the plasma evolution within the filament eruption in *AIA* images. Column density and temperature determination of the filament plasma using absorption diagnostics are described in Section III.4. Kinematics of the filament plasma in the low solar corona are presented in Section III.5. The neutral hydrogen, proton, and electron density determination and results are presented in Section III.6. In Section III.7 we estimate the ionization history of the filament plasma using results from the previous sections as inputs to the Michigan Ionization Code (MIC, Landi et al. 2012). A discussion of the results of this investigation is presented in Section III.8.

III.2. Multi-Instrument Observations of a Coronal Mass Ejection: *ACE/SWICS, SOHO/LASCO, STEREO/SECCHI, SDO/AIA*

The research presented in this chapter is enabled in part by observations of ICMEs from the sensors on board the Advanced Composition Explorer (ACE). The Richardson and Cane (2004, 2010) list (RC list) identifies ICMEs that arrived at Earth using plasma and magnetic field ICME signatures in the *ACE/SWICS, ACE/MAG* (MAGnetic Field Experiment), and *ACE/SWEPAM* (Solar Wind Electron, Proton and Alpha Monitor) measurements. Additionally, the RC list frequently identifies the corresponding *SOHO/LASCO* CME, allowing us to trace the ICME back to the Sun. The CME under scrutiny in this study was chosen based on its visibility in observations from a majority of instruments on board *ACE, STEREO, SOHO*, and *SDO* (described in Section I.3.1 – I.3.2).

This analysis utilized the case of a filament eruption at the Sun associated with an ICME that arrived at the Lagrange 1 (L1) point on August 5th, 2011. The RC list identified the arrival of this intense storm on August 5th, 2011 at 17:51 UT. This geo-effective ICME was tracked back to the solar corona using a combination of multi-instrument remote-sensing and imaging observations to perform time-evolution diagnostics of the properties of the eruption during the initial hours of its journey while it was still in the low solar corona. At the time of the CME eruption, *SDO* was operational, allowing for the use of high-cadence *SDO*/AIA measurements. Furthermore, the twin *STEREO* spacecraft were in near-quadrature with *SDO*; that is, the same CME observed by *STEREO* at the solar limb was observed by *SDO* close to the disk center, minimizing the uncertainty in the 3D reconstructions of the CME plasma.

The RC list pointed us in the direction of the *LASCO* CME associated with our ICME under scrutiny. In the C2 coronagraph the CME eruption was seen starting at ~04:12 UT on August 4th, 2011 shortly after which a partial halo enveloped the solar disk off the west limb (Figure III.1(h)). The C3 coronagraph observed the CME eruption starting at ~04:42 UT after which the CME partially enveloped the solar disk (Figure III.1(e)).

The ICME of interest was observed in EUVI, COR1, and COR2 instruments on *STEREO A* and *STEREO B*. *STEREO A/*EUVI observed a flare starting ~03:46 UT followed by the filament eruption at ~04:06 UT, shortly after which the front of the eruption was outside the field of view of the instrument. The flare was not observed in *STEREO B/EUVI* images but the filament eruption observations were similar to that of *STEREO A/EUVI*. Figure III.1(c) shows the *STEREO A/EUVI* image of the Sun in 304 Å at 04:36:15 UT, and Figure III.1(a) shows the *STEREO B/EUVI* image of the Sun in 304 Å at 04:36:55 UT. A distinct front was seen in *COR1* and *COR2* coronagraphs on both *STEREO* spacecraft starting in images at ~04:10 UT followed by a bright jet-like filament eruption that formed the core of the CME further out in the corona.

In order to uniquely determine the source region of this eruption measured in-situ and by instruments onboard *SOHO* and *STEREO*, the following observations were used: (1) X-ray observations from the Geostationary Operational Environmental Satellite (*GOES*), (2) the Global High-Resolution H-alpha Network (*GHN*), and (3) multi-wavelength observations from *SDO/*AIA.

(1) X-ray observations from *GOES* identified an M9.3 class flare at ~3:41 UT from active region 11261. This active region was also close to the Sun center indicating that a CME eruption here, associated with the highly energetic flare (also observed in *STEREO A/EUVI*), could possibly have been geo-effective.

(2) H-alpha images from 18:30:36 UT on August 3rd, 2011 and 08:04:50 UT on August 4th, 2011 indicated the disappearance of filaments near active region 11261 between the times the images were taken.

(3) Shortly after the flare eruption, time series of *SDO*/AIA images confirmed the eruption of a filament in the vicinity of the AR 11261 at ~04:10 UT. It is anticipated that the flare and filament eruption resulted from significant reorganizing and shearing of the magnetic topology associated with magnetic reconnection in the low solar corona. The filament eruption was clearly visible as a dark absorption feature in *AIA*'s high cadence images during in the initial fifty minutes of its eruption from AR 11261. Figure III.1 (b) shows a snapshot of this eruption at ~04:36 UT in the 304 Å channel.

Using the instruments described above, the August 5th, 2011 ICME disturbance observed by *ACE* at L1 at 17:51 UT was traced back to a filament eruption near active region 11261 on August 4th, 2011 at ~04:10 UT and observed during its evolution. As an additional test, the WSA-ENLIL (Jian et al. 2015) was used, a 3D time-dependent MHD model that predicts the arrival of Earth-directed CMEs capable of inducing geomagnetic storms by mapping the flow evolution out to Earth. It uses white-light images from the *LASCO* and *STEREO* coronagraphs. This model traced the origins of the August 5th, 2011

ICME at L1 to a solar event on August 4th, 2011 at ~04:10 UT, confirming the multi-instrument analysis described above.

The use of multi-wavelength images from *SDO*/AIA to perform diagnostics, as the progress of the filament eruption associated with this CME in the low solar corona is followed, are described in the following sections of this chapter.

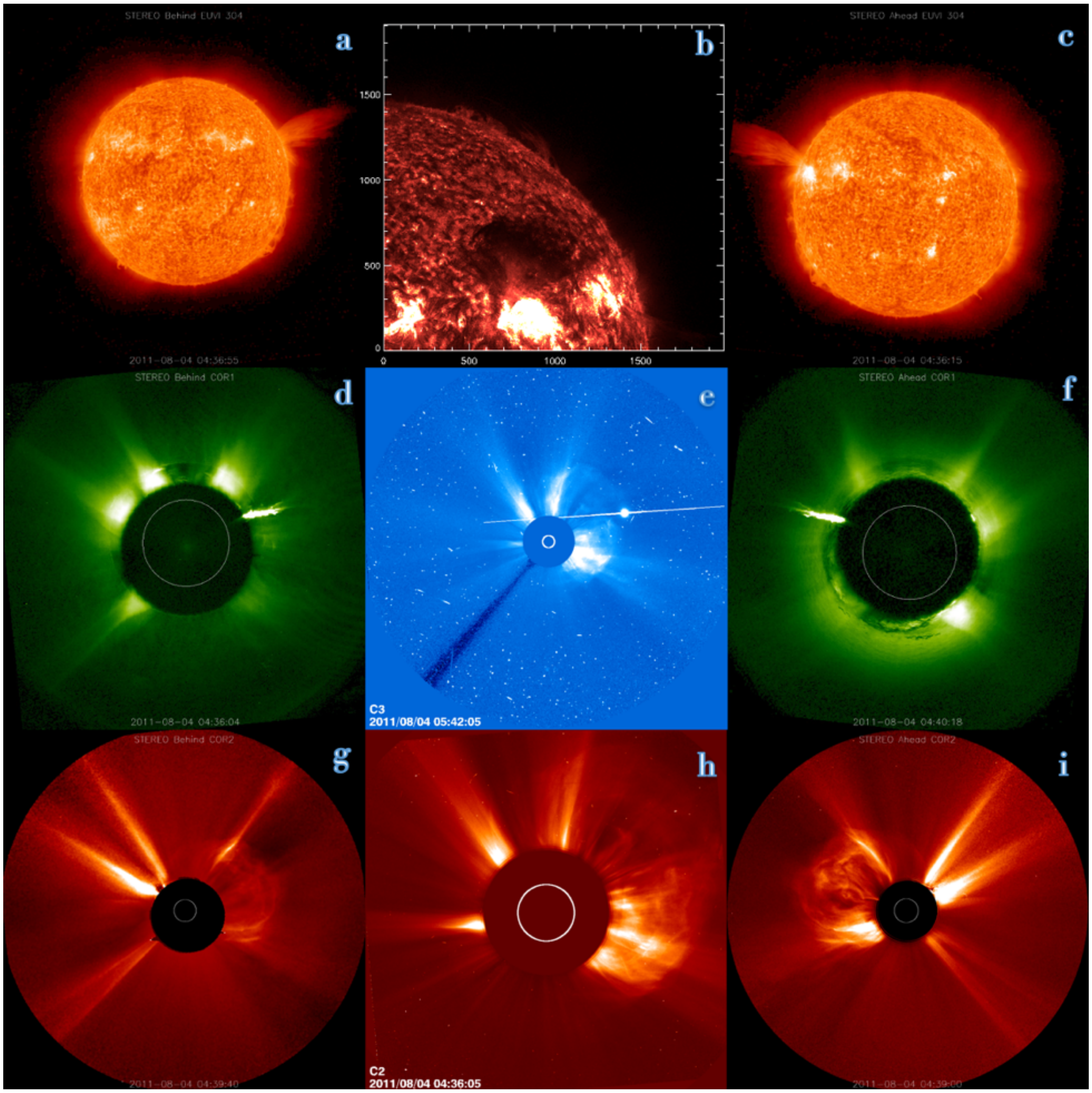

Figure III.1. Multi-instrument observations of an ICME disturbance detected in-situ by *ACE*/SWICS at 17:51 UT, August 5th, 2011 and reported by the RC list. a: *STEREO B*/EUVI 304 Å, b: *SDO*/AIA 304 Å, c: *STEREO A*/EUVI 304 Å, d: *STEREO B*/COR 1, e: *LASCO*/C3, f: *STEREO A*/COR 1, g: *STEREO B*/COR 2, h: *LASCO*/C2, i: *STEREO A*/COR 2. Note that the left column are images taken from the left of the Sun (STEREO Behind), the middle column are images taken along the Sun-Earth line, and the right column are images taken from the right of the Sun (STEREO Ahead).

III.3. Time-dependent Tracking of the Plasma within the Filament Eruption in the Low Solar Corona:

The first step in determining the time evolution of the erupting filament's properties is charting possible paths travelled by the plasma within the eruption, while attempting to ensure the 'same plasma' is tracked over time. *AIA* images of the eruption from 03:45 UT – 05:15 UT, August 4th, 2011 were used to carry out this investigation. They were secured from the Solar Software (SSW) cutout service available online[4] in 171 Å, 193 Å, 211 Å, 304 Å, and 335 Å wavelength channels. The justification of the choice of these five wavelength channels is presented in Section III.4.1. The filament was observed as an expanding dark absorption feature in the north-western hemisphere of the Sun near active region 11261.

The multi-wavelength Flexible Image Transport System (*fits*) files were prepared for analysis using two steps: (1) The Automatic Exposure Control (AEC) effect due to the flare that preceded the filament eruption resulted in a reduced dataset with 24 second cadence during certain periods instead of the expected 12 seconds in some of the channels. Due to these data gaps, the data sets in all wavelength channels were reduced so that each image in one channel corresponded to the image at the closest time-step in all the remaining channels. This produced *fits* files for the eruption in five wavelength regions with time cadences between 12 and 24 seconds. (2) The aia_prep.pro[5] IDL routine was then used to convert all *fits* files from level 1.0 to level 1.5, performing image rotation, translation, scaling, and updating the header information.

[4] https://www.lmsal.com/get_aia_data/

[5] http://www.heliodocs.com/php/xdoc_print.php?file=$SSW/sdo/aia/idl/calibration/aia_prep.pro

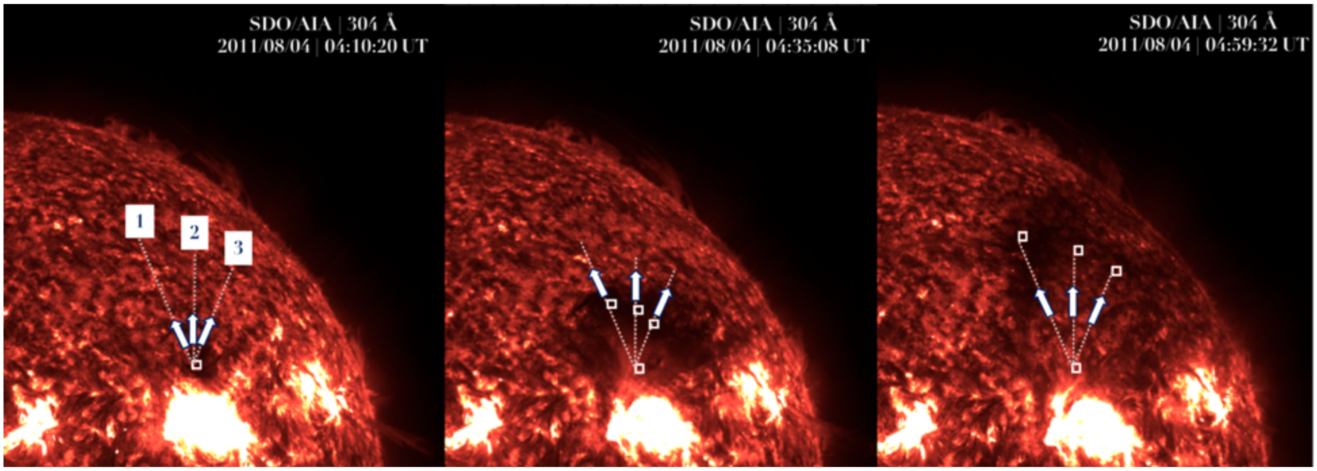

Figure III.2. 304 Å *SDO/*AIA images of the August 4th, 2011 filament eruption at 04:10:20 UT (left), 04:35:08 UT (middle), and 04:59:32 UT (right). The dotted white lines 1, 2, and 3 represent the paths chosen to describe possible trajectories of the plasma within the white box (30x30 pixel) as the filament travelled through the low solar corona.

The method used to determine paths of plasma as the filament erupted using the high-cadence processed *AIA* images is described here. First, a 30x30 pixel parcel was picked within the absorbing plasma at 04:10 UT (Figure III.2, left), which is nearly the size of the entire absorption feature at this time. This is the first observation when the eruption was visible in absorption. Subsequent measurements were obtained every 12-24 seconds, while the filament expanded rapidly in the north-western hemisphere of the Sun over the following 50 minutes during the CME initiation phase. The filament plasma became visible in the small pixel box at ~04:10 UT and expanded in all directions. The evolution of the filament's behavior can be quantified by tracking the plasma in any of these directions. Three paths were picked to cover the range of directions of the expanding plasma and loosely followed specific discernable features within the filament eruption, in an effort to track the same plasma parcel. Along each of these directions, the 30x30 pixel box was stepped out at nearly constant rate to match the movement predicted during the initiation phase of an expanding filament. Care was taken to ensure the chosen boxes contained absorbing plasma (i.e., remained dark) at each time-step under analysis. While this tracing technique is limited due to the projection of 3D structures viewed in 2D, it provides for a unique analysis of the filamentary plasma as: (1) the plasma parcels along each path are shifted in accordance with the near constant speed expansion phase of the CME in *SDO/AIA*, (2) it minimizes averaging effects that would have resulted from performing diagnostics on large portions of the erupting plasma, and (3) allows for a thorough comparative analysis on different parts of the filament considering that there are three possible paths.

III.4. Density & Temperature Diagnostics of the Filament Plasma in the Low Solar Corona:

III.4.1. Absorption Diagnostic Technique:

The absorption diagnostic technique of Landi & Reale (2013) was used to measure the column density and electron temperature of the absorbing plasma within the erupting filament. This technique capitalized on the EUV absorption properties of the filament material through bound-free transitions due to the fact that in four wavelength ranges from 100-1000 Å [100-228 Å, 228-504 Å, 504-912Å, 912-1000Å] the absorption coefficient has a unique temperature sensitivity depending on which ions (H I, He I, He II) absorb. The abovementioned wavelength ranges are defined by the absorption edges of each of these ions, that is the wavelength beyond which the ion stops absorbing, 228 Å for He II, 504 Å for He I, and 912 Å for H I. The temperature diagnostics from absorption are based on the fact that the relative abundance of those ions depend on the electron temperature; thus, it can be applied only to plasmas hotter than 15,000 K (below which H and He are almost entirely neutral) and cooler than ~100,000 K, where the abundance of H I, He I, He II are too small to provide significant absorption. The ability to uniquely observe the filament eruption as distinct absorption features in 171Å, 193 Å, 211 Å, 304 Å, and 335 Å channels of *SDO*/AIA allows for the implementation of this absorption diagnostic technique on *SDO*/AIA high-cadence images since these five passbands were within two of the four wavelength ranges.

By neglecting the filament's own emission, the amount of radiation absorbed by a plasma parcel can be computed using Beer's law which states:

$$F_{abs} = F_{inc}\, e^{-\tau} \qquad \textbf{Equation III.1}$$

Where, F_{inc} is the intensity of incident radiation on an absorbing plasma parcel, F_{abs} is the intensity measured after absorption, and τ is the optical depth. Equation III.1 implicitly assumes that the filament itself is not emitting at the wavelengths used for diagnostics. This is true for all *AIA* channels we considered except, in principle, the 304 Å channel, which is dominated by the strong He II 303.7 Å transition which could contribute to observed counts. In this chapter, it is assumed that for the 304 Å channel He II emission is negligible; however, the importance of considering the emission is elaborated on in Chapter IV.

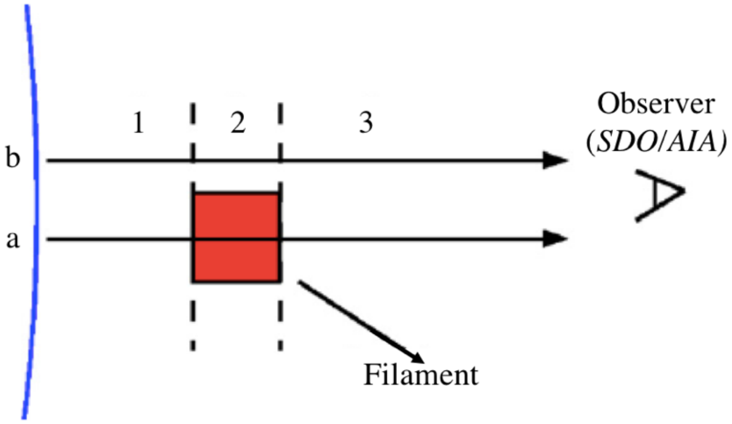

Figure III.3. Schematic showing a simplified version of the geometry described in Section III.4.1, when the absorbing plasma is against the solar disk. Regions 1, 2, and 3 are the 'background', 'filament' (absorbing plasma), and 'foreground' regions, respectively, for lines of sight *a* and *b*. Adapted from Landi & Reale (2013).

Adapted from Landi and Reale (2013), Figure III.3 shows a simplified geometry of an absorbing filament plasma parcel in the low solar corona. Here, F_a and F_b are measured EUV intensity values observed along two lines of sight: '*a*' intercepts the absorbing filament plasma, and '*b*' can be envisioned as the intensity at the location in the absence of the filament plasma. The line of sight can be divided into three regions: finite depth of the filament, region behind the filament (background), and region between the observer and the filament (foreground).

In order to simplify the number of unknowns, Landi and Reale (2013) outlined three different cases to execute the diagnostic technique based on reasonable approximations on the absorbing plasma. In testing the three cases, the scale height of coronal emission was estimated by taking a 30-pixel high horizontal cut in all 102 *AIA* images used between 04:10 UT – 5:00 UT in the northern hemisphere near the western limb. The distance at which the intensity dropped by a factor of 1/*e* from the edge of the solar disk was approximately 0.06 solar radii with insignificant uncertainty. Since the filament eruption was already at 1.7 solar radii by 04:10 UT (determined using *STEREO A* observations, Section III.5*)* the case where the absorbing material (filament) is located at altitudes significantly greater than the scale height of the coronal emission in the solar atmosphere is followed. Hence, the foreground emission along the line of sight can be neglected in comparison with the background emission i.e., $F_3 << F_1$. Estimates of the line of sight depth of the absorbing plasma (Section III.6) show that $F_2 << F_1$ could also be assumed.

Furthermore, Equation III.1 and Figure III.3 can be directly related since F_{abs} is F_a and F_{inc} is F_b, allowing for the estimation of optical depth from the measured values of F_a and F_b as follows:

$$\tau = -\ln (F_a/F_b) \qquad \textbf{Equation III.2}$$

where $F_2 << F_1$ and $F_3 << F_1$, based on our corroborated geometric assumptions.

The optical depth is also defined as follows, where n_H is the neutral hydrogen density, dl is the line of sight depth integrated over a parcel of thickness S, and k_{eff} is called the effective absorption coefficient:

$$\tau = \int_0^S n_H k_{eff} dl = n_L k_{eff} \qquad \textbf{Equation III.3}$$

In the above equation, the integral of the neutral hydrogen density (n_H*)* over the line of sight (*L)* is re-written as the column density n_L per the following equation:

$$n_H = n_L/L$$ **Equation III.4**

and $k_{eff} = f(\mathrm{HI}, T)k_{H1} + A_{He}[f(\mathrm{HeI}, T)k_{He1} + f(\mathrm{HeII}, T)k_{HeII}]$ **Equation III.5**

k_{eff} is the effective absorption coefficient with unique temperature dependencies in the four wavelength ranges described earlier in this section. Respectively, k_{H1}, k_{He1}, and k_{HeII} are absorption cross-sections of H I, He I, and He II, which were calculated from the photo-ionization cross-sections from Verner et al. (1996), the f functions are the temperature-dependent fractional abundances of each species which were taken from the CHIANTI database (Del Zanna et al. 2015; Dere et al. 1997) under the assumption of ionization equilibrium, and A_{He} is the helium abundance relative to hydrogen. We assume the helium-to-hydrogen abundance ratio, $A_{He} = 0.05$.

Landi and Reale (2013) defined the L(T) function as:

$$L(T) = -\frac{1}{k_{eff}(T)}\ln\left(\frac{F_a}{F_b}\right)$$ **Equation III.6**

Using Equations III.2 and III.3, the value of L(T) at the absorption plasma's temperature is equal to the column density (n_L) regardless of the channel used to measure F_a and F_b. Using Equation III.6, we can define the L(T) function at all temperatures for each AIA channel, as shown in Figure III.4. The intersection point of these curves gives values of the column density and the corresponding temperature of the absorbing plasma. Results from this diagnostic technique for the filament under consideration are described in Section III.4.3.

While the helium abundance (A_{He}) is expected to vary within each filament, it was set as 5% for the purposes of this analysis. The diagnostic results using A_{He} = 1% and 10%, compared with the results using A_{He} = 5% show within an order of magnitude difference in column density and no change in temperature. This is expected because the temperature only depends on He I and He II and changing A_{He} only changes the point at which the L(T) crossing takes place vertically in Figure III.4.

Since the Landi and Reale (2013) diagnostic technique used CHIANTI ion fractions, it implicitly assumes the plasma is in ionization equilibrium, while the CME plasma may depart from this condition. A test and discussion of this assumption is presented in Section III.8.1 of this chapter.

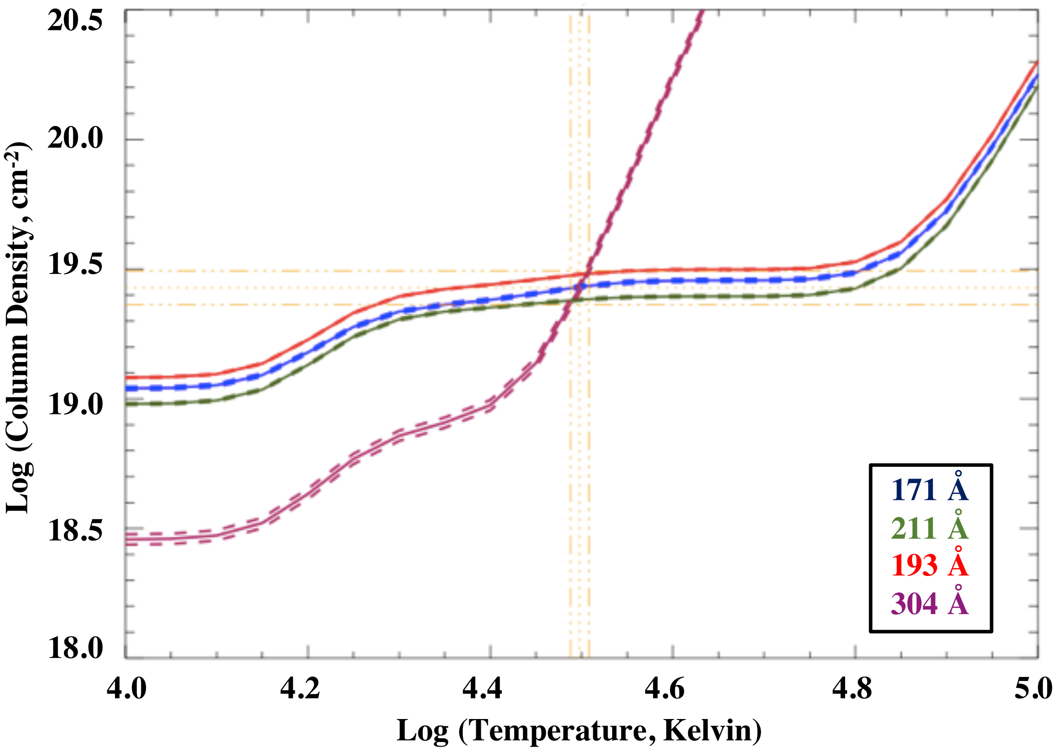

Figure III.4. Diagnostic results for the absorbing plasma parcel location at 04:23 UT along Path 1. The y-axis is the L(T) function or the column density (cm^{-2}) and the x-axis is the logarithm of temperature (K). The point where the L(T) curves for 171 Å, 193 Å, 211 Å, 304 Å intersect gives the measure of the column density and temperature of the absorbing plasma at that time and location.

III.4.2. Estimation of F_b :

In order to determine F_b (Equation III.2), reasonable approximations needed to be made based on the time-dependent geometry of the filament. One method to approximate the value of F_b is to assign the measured intensity at a point close to the filament but outside of it (e.g. Gilbert et al. 2005). Since we considered 102 timestamps over the course of 50 minutes where the filament geometry changes considerably, we chose instead a relatively quiescent period before the flare and filament erupted when no transient structures were apparent. If the intensities at the locations of the plasma parcels (Figure III.2) did not vary considerably, we could use them as a proxy for F_b.

Before the flare erupted at ~03:45 UT, the intensities at each location of the plasma parcels were monitored from 03:00 UT to 03:44 UT using the 12 to 24 second cadence processed *SDO/AIA* images. The means, uncertainties of intensities at each location, and their intensity profiles over time in the 193 Å and 304 Å channels were analyzed. While there was some variability in the time-scales of the cadence of *AIA* observations, the intensities in the plasma parcels did not change significantly over timescales of a few minutes, and the trends in intensity remained intact over the 40 minutes analyzed. It was concluded that the intensities at ~03:40 UT were reasonable approximations for F_b of the absorbing plasma along the three paths under scrutiny because (1) the mean intensity at this time was comparable to the mean values over the 40 minutes analyzed with reasonable uncertainty, and (2) the uncertainty of intensities from 03:00 - 03:40 UT for a majority of the plasma parcels analyzed was within 10% of the mean.

III.4.3. Results of Diagnostics:

In the diagnostics discussed here, the 335 Å channel was not considered due to the low signal-to-noise ratio in the data. The results of the diagnostic technique for one time-step along Path 1 are shown in Figure III.4. Here [171 Å, 193 Å, 211 Å] and 304 Å belong to wavelength regions with different temperature functions of the effective absorption coefficient, enabling us to measure the column density and temperature of the 30x30 pixel plasma parcel at that time and location from the crossing of all the curves. The crossing point is well-defined and allows for accurate diagnostics.

Diagnostic results such as those shown in Figure III.4 were produced for 102 timestamps between 04:10 UT – 05:00 UT for all three plasma trajectories within the filament (Figure III.2). Distinct intersections in the L(T) curves were obtained for approximately the first 20-25 minutes of analysis for the three plasma paths, allowing for reliable measurements of column density and temperature at these times. These results are shown in Figure III.5 - III.6. The intersecting points and the associated uncertainties for the final few minutes of analysis were higher than the remaining period and are shaded red. The bottom x-axis for plots in Figure III.5 - III.6 show time, and the top x-axis shows the corresponding height of the filament (see Section III.5). Figure III.5 shows logarithm of the column density for Paths 1, 2, and 3 respectively, and Figure III.6 show logarithm of the temperature for Paths 1, 2, and 3. Between ~4:40 UT and 5:00 UT for Path 1 and between ~04:32 UT and 5:00 UT for Paths 2 and 3, the L(T) curves for passbands in the two wavelength domains either did not intersect or did so with unreasonable uncertainty. They are hence excluded from these results. This can either be attributed to the temperature of the absorbing material falling below 15,000 K at which point the diagnostic technique does not work, or the absorption features were not consistently strong enough in all the wavelength channels.

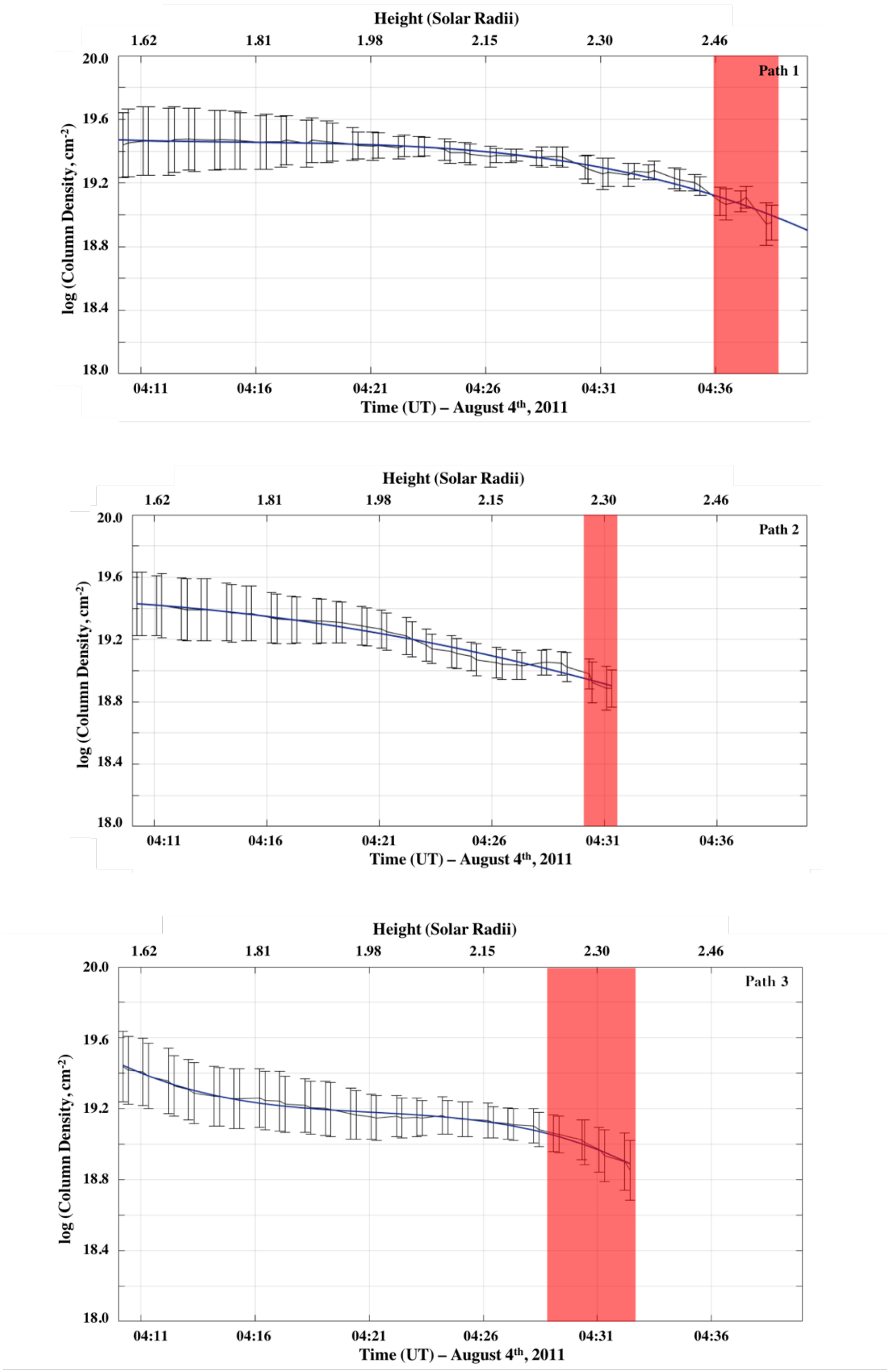

Figure III.5. The y-axis shows logarithm of column density (cm^{-2}) versus time (UT) on the bottom x-axis and the corresponding approximate height (solar radii) of the filament plasma parcels on the top x-axis, for Paths 1, 2, and 3. The colored lines represent fits to the data. The regions shaded red had very high uncertainties in measurements from the diagnostic technique.

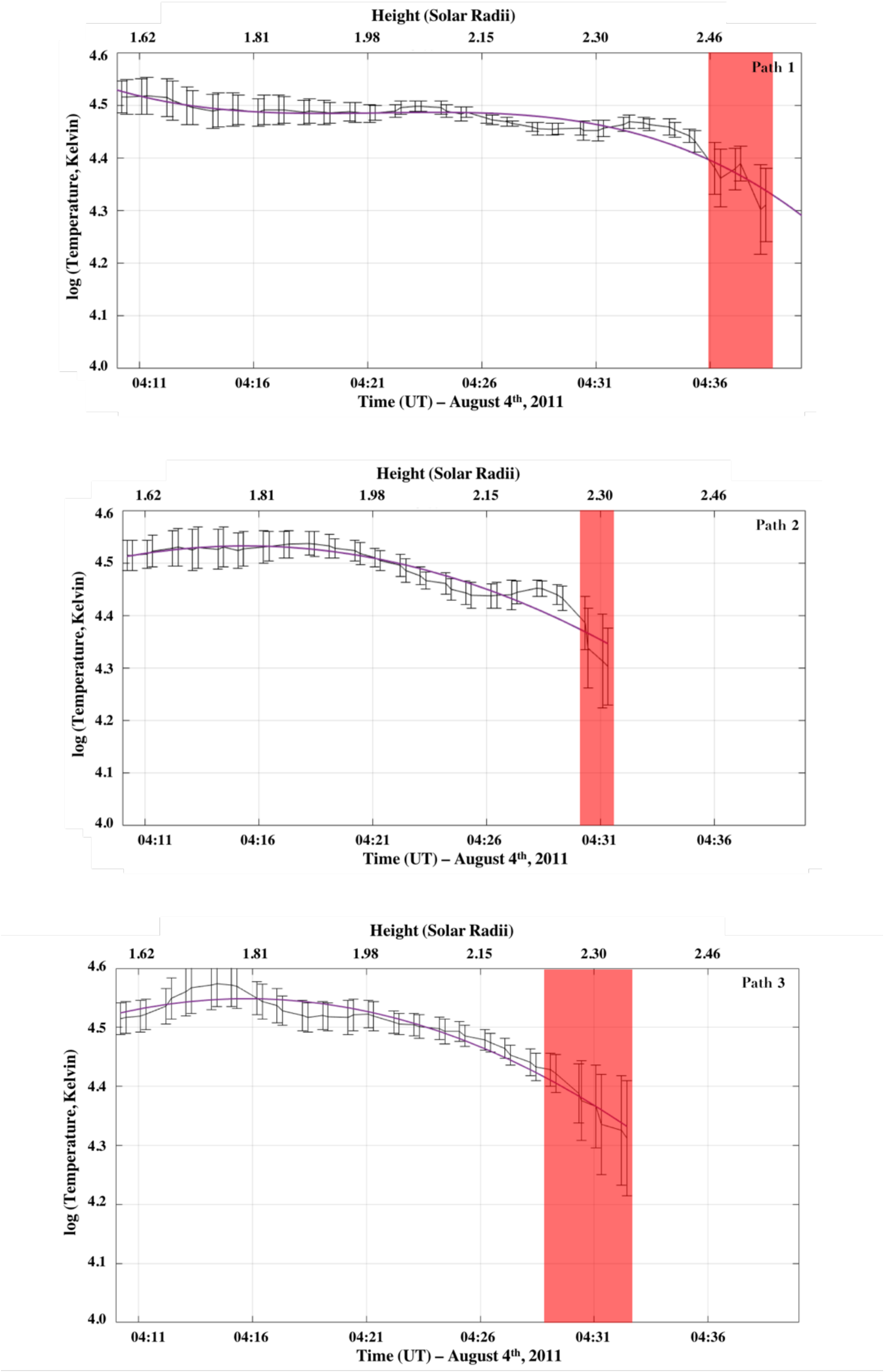

Figure III.6. The y-axis shows logarithm of temperature (Kelvin) versus time (UT) on the bottom x-axis and the corresponding approximate height (solar radii) of the filament plasma parcels on the top x-axis, for Paths 1, 2, and 3. The colored lines represent fits to the data. The regions shaded red had very high uncertainties in measurements from the diagnostic technique.

III.5. Kinematics of the Filament Plasma in the Low Solar Corona

In order to determine the height and speed evolution of the plasma parcels as they travel along the three paths (Figure III.2) as part of the erupting filament, *STEREO A* EUVI, COR1, and COR2 observations were utilized. The *STEREO A* instrument suite was chosen over *STEREO B* since it had a marginally better view of the active region. The filament eruption is often identified as the brightest part of the CME in white-light images (Parenti 2014) and since *STEREO* was in near quadrature with *SDO* at this time, the tip of the filament eruption seen in the time-series images was taken to roughly correspond to the height at which the plasma parcels within the filament were observed. All *SECCHI* images were first processed from level 0.5 to level 1.0 using the secchi_prep.pro[6] SolarSoft routine. The tip of the filament remained in the field of view of EUVI till ~4:10 UT after which we measured the height using COR1. Speed evolution approximations were determined from the height evolution profiles. Results of this analysis are shown in Figure III.7.

Accurate estimates of the height of the plasma parcels within the filament were limited by the fact that this was a surge CME (Vourlidas et al. 2003, Vourlidas et al. 2017) with indistinguishable parts. This made it unfeasible to precisely identify the plasma observed in AIA to the corresponding *STEREO* plasma. The uncertainties in speed values presented in Figure III.7 are hence considered in the computation of composition described in Section III.7.

[6] http://www.heliodocs.com/php/xdoc_print.php?file=$SSW/stereo/secchi/idl/prep/secchi_prep.pro

All three filament plasma parcels analyzed were assumed to be at the same height and traveling at the same speed which may not be a realistic approximation, and thus is a limitation to be considered in interpreting the outcome of this analysis.

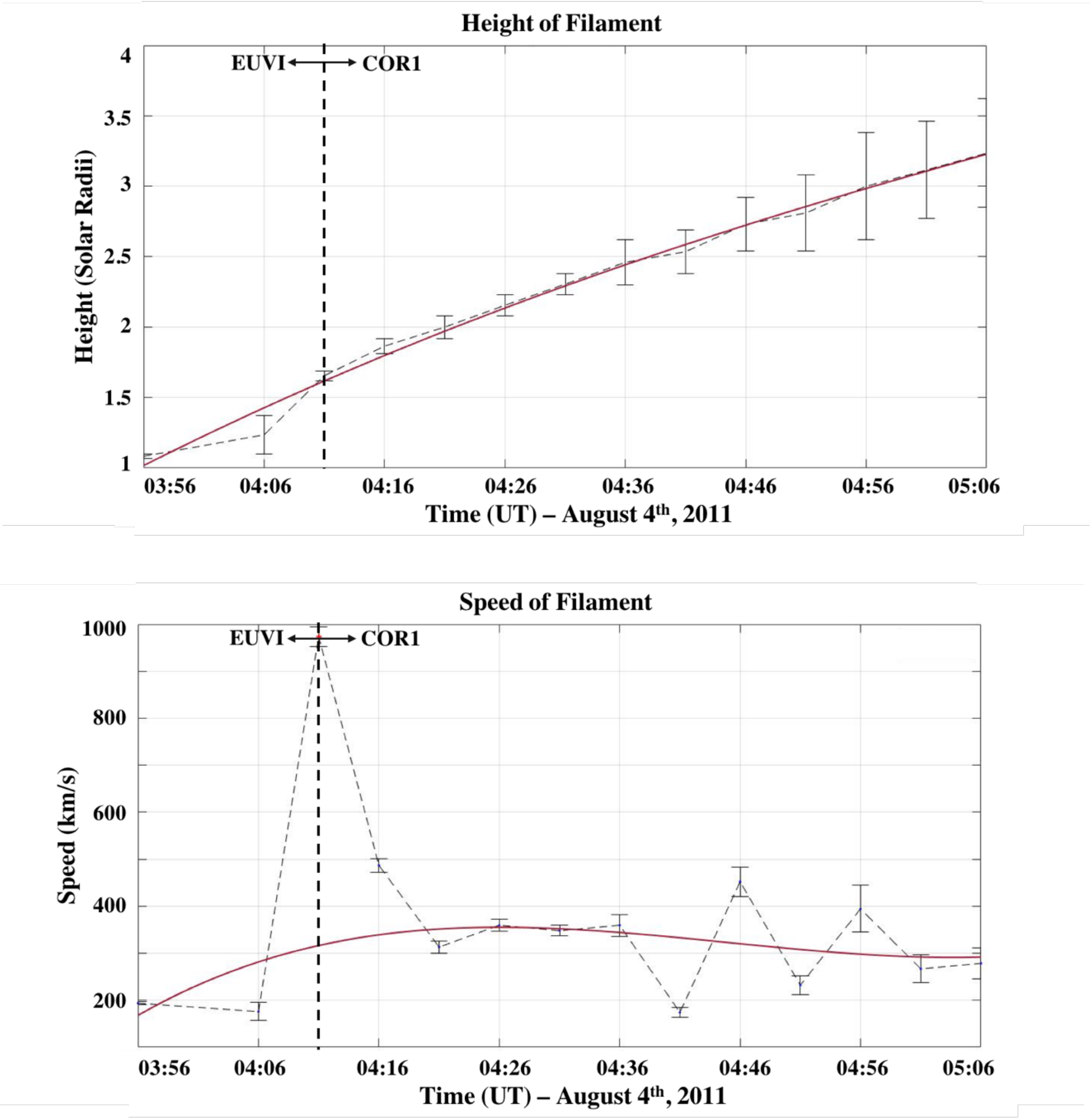

Figure III.7: (top) A plot of height of the filament eruption as seen by *STEREO A* EUVI and COR 1 versus time. (bottom) A plot of speed of the filament eruption derived from the height vs time measurements. In the speed/time plot, the measurement at 04:11 UT is treated as an outlier for fitting purposes.

III.6. Neutral Hydrogen Density, Proton Density & Electron Density of the Filament Plasma in the Low Solar Corona

The average lower limit to the neutral hydrogen density can be directly computed from the column density if the line of sight depth of the absorbing parcel is known as done in Landi & Reale (2013), following Equation III.4. Assuming homogenously absorbing plasma parcels, a unity 1D line of sight filling factor is used, giving a lower limit of the neutral hydrogen density. While previous studies (e.g. Landi & Reale 2013) have assumed arbitrary values of this depth, time series of the depth of the absorbing plasma are determined using *STEREO A/*EUVI and COR 1 images that observe the filament eruption. At each time stamp where *STEREO A/*EUVI and COR 1 images are available, the latitudes at which the plasma parcels are tracked along the three paths were recorded. The depth of the absorbing plasma as seen by EUVI and/or COR 1 at each of these latitudes on the Sun was used as an approximation of the depth along the line of sight at that instant. Profiles for line of sight depth of the plasma are shown in Figure III.8. It is noted that there is little variation between the depth profiles for the three paths, and the values of the depth are large due to the large angular scale of the filament eruption. Appropriate fits to the data are chosen to match the column density measurements. This process is limited by the low cadence *EUVI* and *COR 1* observations, and the fact that at certain timestamps the filament line of sight was outside the field of views of *EUVI* and *COR 1* despite the field of view overlap. Results for the neutral hydrogen density for Paths 1, 2, and 3 are shown in Figure III.9.

The proton density is computed using the read_ioneq.pro[7] CHIANTI code. Ratios of neutral hydrogen abundance to proton abundances are drawn under conditions of ionization equilibrium from temperature in the range of 10^4 to 10^9 Kelvins. Using these ratios, the measured neutral hydrogen density (Figure III.9) and temperature (Figure III.6), proton density profiles are derived. As discussed in Section III.4.1, an ionization equilibrium approximation is a critical caveat for these computations since this might not be a realistic approximation. This approximation is discussed in Section III.8.1. Results for the proton number density, under these approximations, for Paths 1, 2, and 3 are shown in Figure III.10. The error bars on proton density represent the uncertainties propagated from the uncertainties in temperature and neutral hydrogen density measurements using standard propagation methods.

Figure III.10 shows that the measured values of proton density drop just under two orders of magnitude for all three paths. However, since almost an order of magnitude of this total drop occurs in the region of measurements marked in red, corresponding to higher uncertainties in temperature and column density measurements, this trend is treated with extreme caution. This decrease is largely due to the drop in temperature occurring in the same time frame, which implies, under ionization equilibrium, a sharp reduction in hydrogen ionization. As discussed in Section III.4.1, a higher helium abundance results in lower values of column density. Due to these uncertainties, it is likely that the proton densities do not drop as rapidly as shown in the red region of Figure III.10 and the drop is likely closer to an order of magnitude.

---

[7] http://www.heliodocs.com/php/xdoc_print.php?file=$SSW/packages/chianti/idl/read/read_ioneq.pro

The electron number density was then computed from the proton number density using proton_dens.pro[8] SolarSoft code. Temperatures measured and reported in Section III.4.3 were used as inputs to the code to compute the ratio of proton density to electron density using abundances and ion balance files.

---

[8] https://hesperia.gsfc.nasa.gov/ssw/packages/chianti/idl/utilities/proton_dens.pro

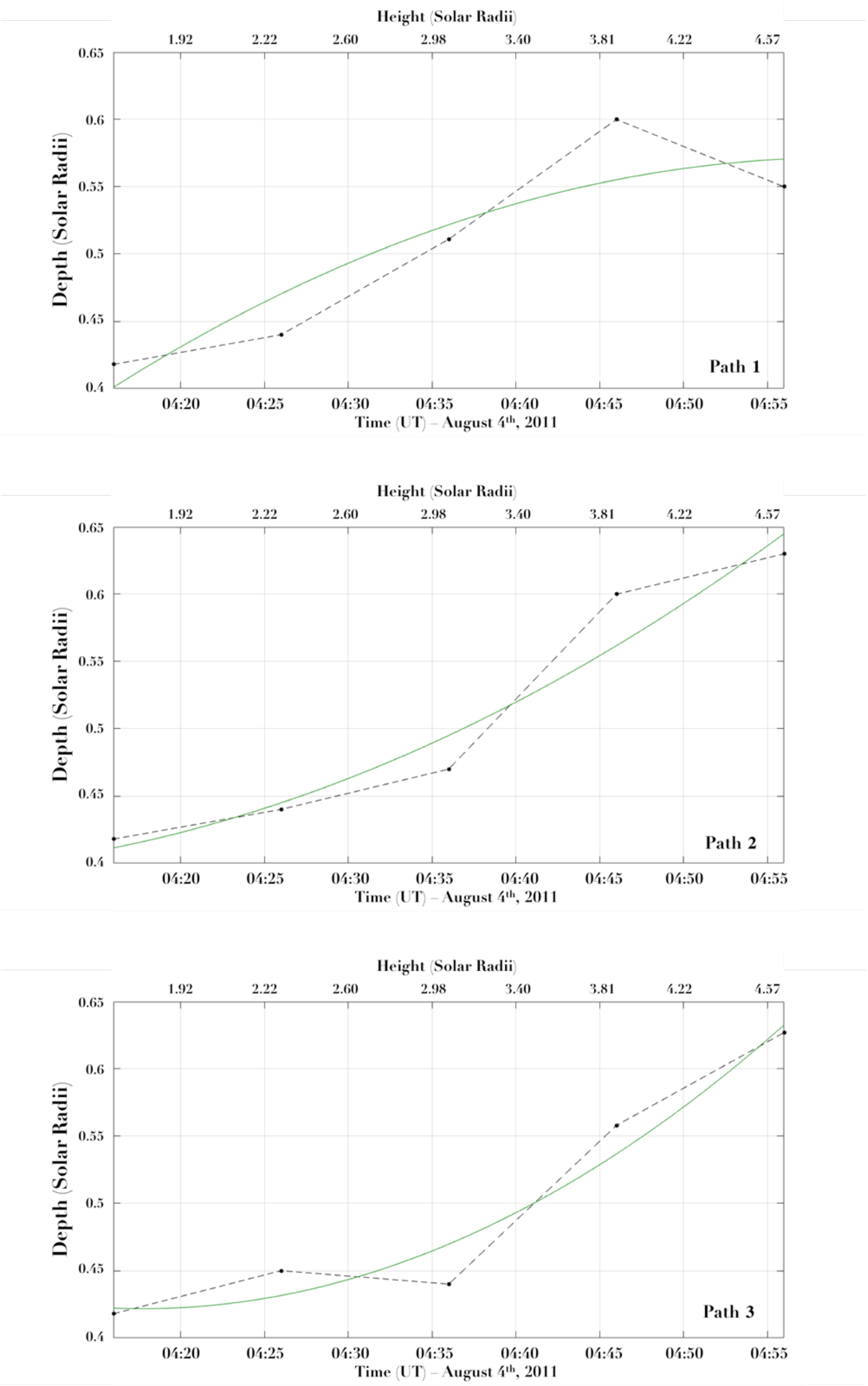

Figure III.8: Depth of the absorbing plasma (solar radii) versus time (UT) on the bottom x-axis and the corresponding approximate height (solar radii) of the filament plasma parcels on the top x-axis, for Paths 1 (top), 2 (middle), and 3 (bottom) computed using *SDO/AIA, STEREO A/EUVI and COR1* images. The green curves are fits to the data.

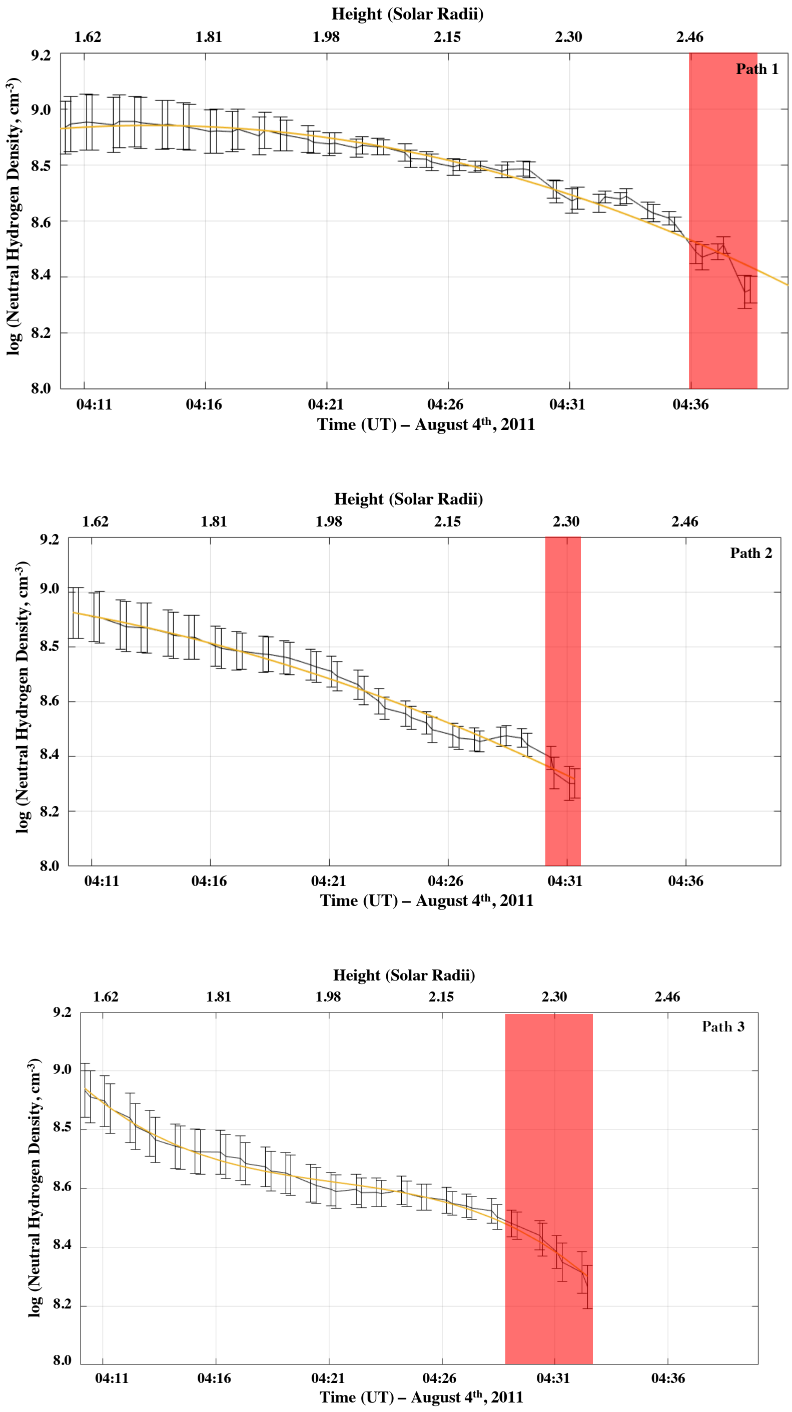

Figure III.9: Number density of neutral hydrogen (cm^{-3}) versus time (UT) on the bottom x-axis and the corresponding approximate height (solar radii) of the filament plasma parcels on the top x-axis, for Paths 1 (top), 2 (middle), and 3 (bottom), computed using Equation 4 and line of sight depth profiles shown in Figure III.8. The orange curves are fits to the data. The regions shaded red had very high uncertainties in measurements from the diagnostic technique.

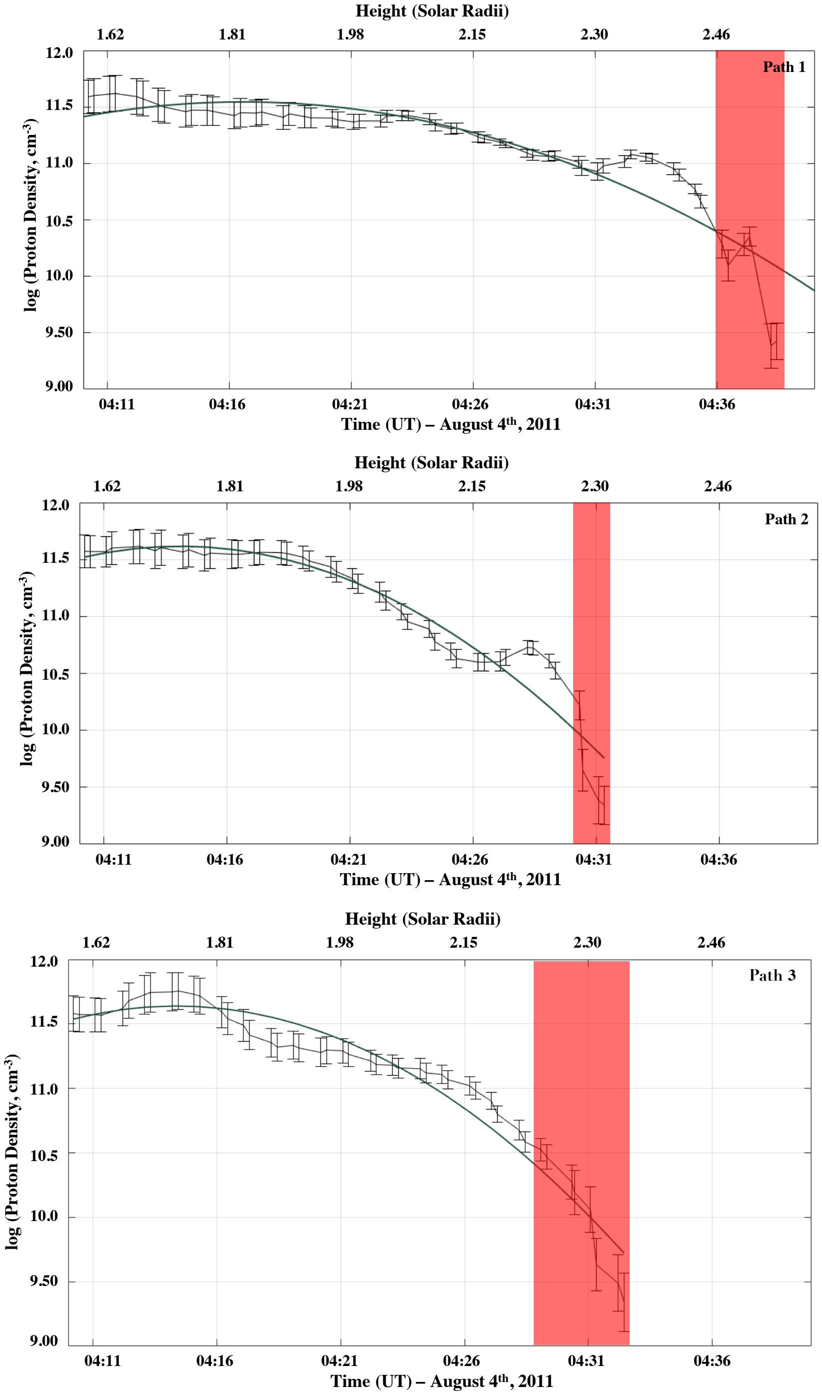

Figure III.10: Proton number density (cm^{-3}) versus time (UT) on the bottom x-axis and the corresponding approximate height (solar radii) of the filament plasma parcels on the top x-axis, for Paths 1 (top), 2 (middle), and 3 (bottom). The green curves are fits to the data. The regions shaded red had very high uncertainties in measurements from the diagnostic technique.

III.7. Ionization History of the Filament Plasma in the Low Solar Corona:

In order to determine the ionization history of the plasma parcels the Michigan Ionization Code (MIC) developed by Landi et al. (2012) is used. MIC is an ion composition model that predicts the evolution of the ion abundances of wind plasma from the source region out through the freeze-in point and beyond to Earth. It solves for ionization and recombination processes for a chosen element as it travels outward from the Sun using the following set of equations:

$$\frac{\partial y_m}{\partial t} = n_e[y_{m-1}C_{m-1}(T_e) + y_{m+1}R_{m+1}(T_e)] + y_{m-1}P_{m-1} - y_m[n_e(C_m(T_e) + R_m(T_e)) + P_m]$$

Equation III.7

$$\Sigma_m y_m = 1,$$

Equation III.8

where the photoionization term, P_m, is given by

$$P_m = \int_{\upsilon_m}^{\infty} \frac{4\pi J(\upsilon)\sigma_m(\nu)}{h\upsilon} d\upsilon$$

Equation III.9

where T_e is the electron temperature, n_e is the electron density, R_i and C_i are the total recombination and ionization rate coefficients, y_m is the fraction of the element X in charge state m, h is the Planck constant, c is the speed of light, σ_m is the photoionization cross section for the ion m, ν_m is the frequency corresponding the ion’s ionization energy, and $J(\nu)$ is the average spectral radiance of the Sun at frequency ν. While charge transfer, as discussed in Arnaud & Rothenflug (1985), can be important at temperatures smaller than 25,000 K, we neglect it as the temperature of the filament plasma remains above this value for most of the time under consideration. Equations III.7 – III.8 for each element are solved numerically as a set of stiff ordinary differential equations using a fourth-order Runge-Kutta method (Press et al. 2002). To ensure computational efficiency, the step size is set adaptively and the accuracy of the integrator is tested.

MIC was run for the plasma parcels within the filament for Paths 1, 2, and 3. The effects of photoionization on the charge state composition of the filament plasma were taken into account following the discussion in Landi & Lepri (2015), where they found that photoionization had significant effects on the charge state distribution of C, N, and O. They also documented significant effects on Fe charge states in CMEs. MIC also accounted for the impact of the energetic M9.3-class flare that erupted prior to the filament liftoff on the ionization states. The flare spectrum for an X1.0-class flare as discussed by Landi and Lepri (2018) is used in the computation presented here. Inputs to the MIC were as follows:

1. *Electron temperature* – Values are described in Section III.4.3 and shown in Figure III.6.
2. *Bulk speed of plasma* - Two ionization profiles were produced using the polynomial fits to the (mean values ± uncertainties) of the speeds (Figure III.7, bottom). This was done to account for the uncertainty in the speed determination. However, results from both sets of speeds did not show significant variation hence the results using the mean value of speeds are presented in this report.
3. *Electron density* – Values are described in Section III.6.

Results of the MIC are shown in three sets of plots in Figure III.11. The top set of plots is for Path 1, the middle set is for Path 2, and the bottom set is for Path 3. The bottom panel in each set shows the evolution of the relative abundance, represented with color bars, of the charge states of C, N, O, and Fe to the total abundance of their respective elements, as the plasma parcels within the filament travel from 1.6 – 2.4 solar radii. The top panel in each set shows the relative abundance of the charge states of C, N, O, and Fe to the total abundance of their respective elements at the maximum height of the plasma parcels along the measured trajectories. These plots are similar to those in Gruesbeck et al. (2011) and can be used to compare with in-situ values to test the freeze-in condition.

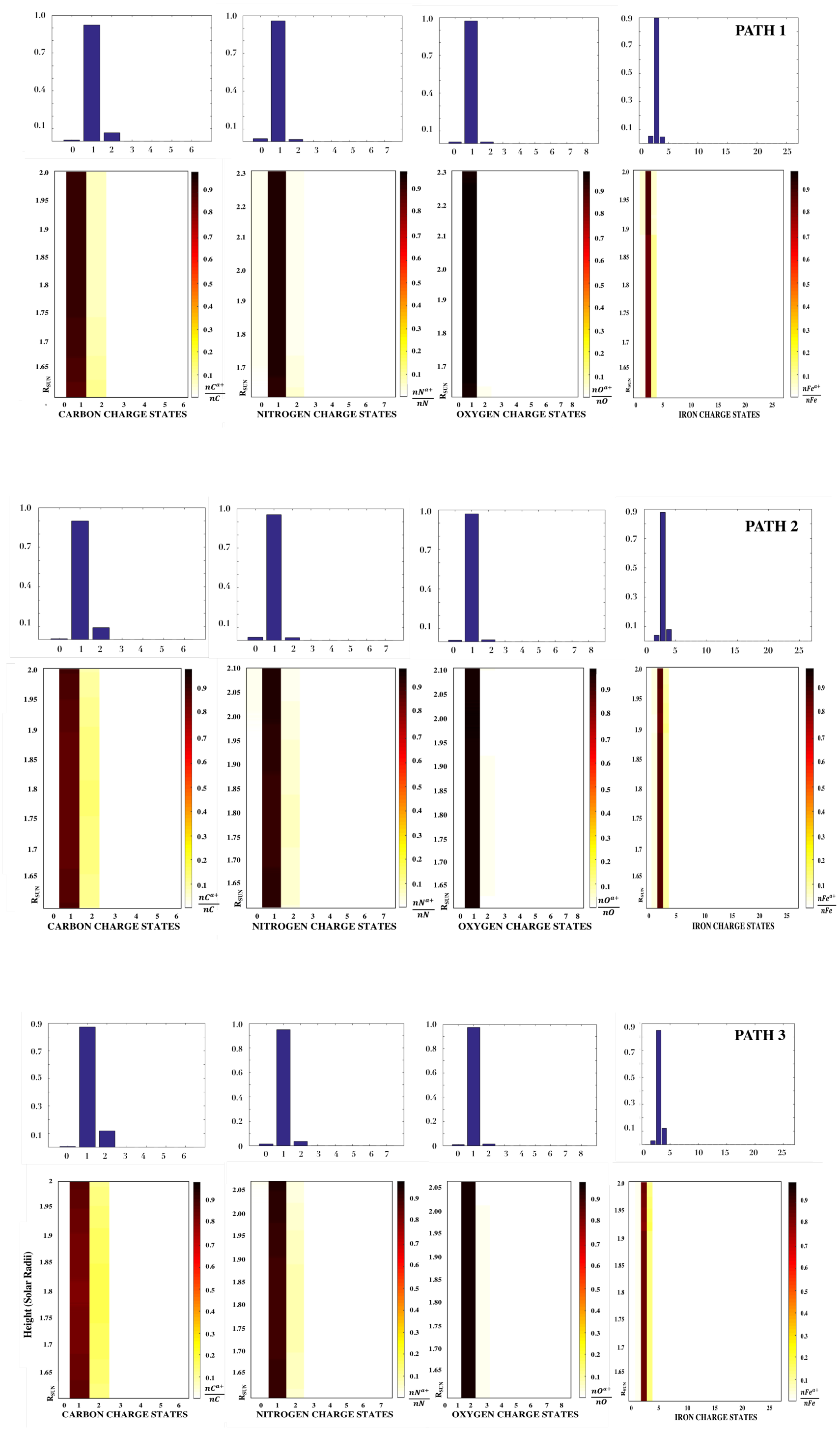

Figure III.11: Results from Michigan Ionization Code using the measured values of density, temperature & speed for Paths 1(top), 2(middle), and 3(bottom). For each path: the bottom set of panels show the evolution of the charge states of Carbon, Nitrogen, Oxygen, and Iron with height, and the top set of panels show the final charge states predicted at the maximum height.

III.8. Discussion

III.8.1. Ionization Equilibrium:

The absorption diagnostic technique (Section III.4.1) was implemented under the assumption of ionization equilibrium since the ion fractions used from CHIANTI are computed under this assumption. Additionally, Section III.6 describes the proton density calculations from the neutral hydrogen density, also assuming ionization equilibrium. In order to test the validity of this approximation, the ionization profiles of H I, He I, and He II described in Section III.7 were compared with the equilibrium profiles of the same ions along the three plasma parcel trajectories. It is found that the departure from equilibrium was within 10% for the three ions, justifying the approximation under which the calculations presented in this chapter were performed.

The recombination and ionization time scales at the measured temperatures for H I, He I and He II were calculated using the CHIANTI routines recomb_rate.pro and ioniz_rate.pro (Dere et al. 2009). For the temperature measurements along all three plasma paths within the filament, the ionization and recombination time scales for the ions ranged between 10-100 seconds. It is useful to compare these with the timescales at which the large-scale plasma processes are evolving. For instance, we find the expansion time of the plasma to be between 500-1000 seconds through its trajectory. The atomic processes taking place at a faster rate than the change in the physical properties of the plasma support the ionization equilibrium approximation.

III.8.2. Freeze-in Condition in Filament Plasma:

The disturbance from the ICME associated with the filament eruption under scrutiny was registered by the RC list at 17:51 UT on August 5th, 2011, with the ICME duration from 22:00 UT, August 6th, 2011 – 22:00 UT, August 7th, 2011. The heavy ion charge states during the ICME period and in the 12 hours before and after were analyzed. No signatures of cold plasma in the form of low charge states of carbon, nitrogen, oxygen, and iron were recorded in the in-situ observations at 1 AU by *ACE,* following the criteria outlined in Lepri and Zurbuchen (2010). Since filamentary signatures were not detected, the 5% He/H abundance value assumed to calculate the effective absorption coefficient was not validated. This lack of low-ionization plasma in the measurements could be due to two causes. First, the filament plasma was not frozen in at the maximum height (~2.4 solar radii) observed in this analysis. The measured high density of the filament plasma also supports this scenario. As a result, the plasma may have continued to ionize due to additional heating at larger heights. Conversely, if the plasma continued to cool, most of the material could end up in the neutral state, in which case *ACE* would not be able to detect the filament composition due to lack of neutral particle sensors onboard. Second, the lack of low ionization states in in-situ measurements of the CME plasma could also be a direct measure of the low filling factor of the filamentary material within the ICME. In fact, even though ~70% of all CMEs (e.g. Gopalswamy et al. 2003) are associated with filament eruptions, only ~4% of all CMEs incident at L1 have signatures of cold filament material (Lepri and Zurbuchen 2010). The Lee and Raymond (2012) investigation of 10 ICMEs observed in *SOHO/UVCS* showed average covering factors of ~10% of the low ionization state plasma in these events, concluding that the lack of low ionization states observed by *ACE* results from the small probability of the spacecraft intercepting these low ionization regions. To investigate connections between the coronal charge states of the core plasma with in-situ values, the filament eruption needs to be analyzed in observations at larger heights. This will be addressed in future studies utilizing observations of CMEs further out in the solar corona.

III.8.3. Heterogeneous & Heated Plasma:

The temperature and density measurements (Figures III.5, III.6, III.9, III.10) indicate that the plasma parcels within the filament eruption traveling along the three paths (Figure III.2) behaved differently; thus, the filament plasma was heterogeneous. Likewise, in their analysis of the *Hinode*/EIS spectra of a CME core, Landi et al. (2010) concluded the core was made of two different plasma components moving coherently but with different temperatures, filling factors, and densities.

Measured profiles of density and temperature of the filament plasma were compared with density and temperature profiles for an adiabatically expanding plasma parcel using the initial temperature and density measured for each parcel trajectory as boundary conditions. This comparison provided strong evidence for the presence of additional sources of heating throughout the observed filament trajectory because the measured density and temperature profiles did not decrease as rapidly nor in a manner similar to an adiabatically expanding plasma. The filament plasma had to be continuously heated throughout its trajectory, also leaving the question open as to whether the erupting filament is still subject to additional heating beyond the heights observed by AIA. Such additional heating, if present, would be critical to our understanding of CME evolution. This conclusion is in agreement with the findings of Filippov and Koutchmy (2002) who observed fast heating within prominence plasmas as EUV observations revealed a sudden change from absorption to emission during the eruptive phase. They suggested that this was a result of shock heating of the pre-eruptive state being transformed into heat through collision processes of counteracting flows. The specifics of heating in the filament under consideration will be revisited in Chapter IV of this dissertation.

CHAPTER IV

EUV Diagnostics of Optically Thick Plasmas using the 304 Å Channel

Results presented in this chapter are current in preparation for submission to the Astrophysical Journal

IV.1. Challenges in Utilizing 304 Å Observations:

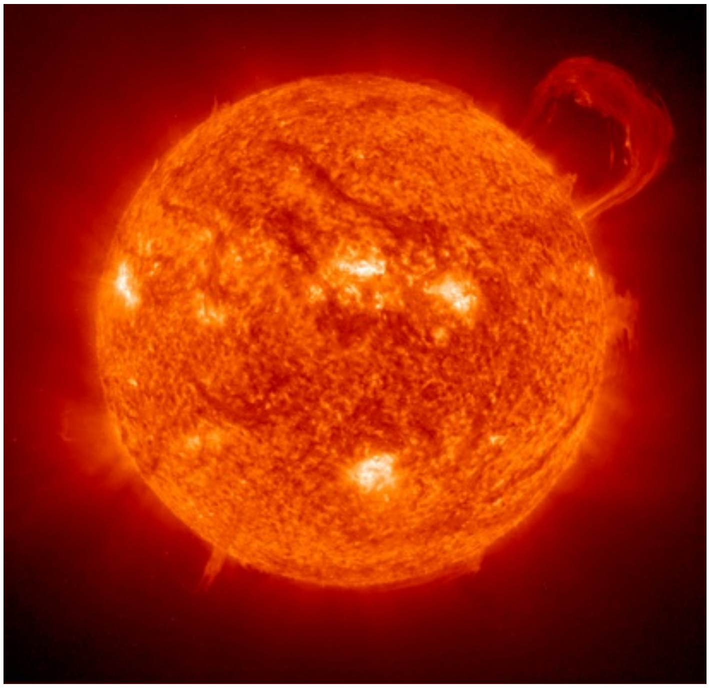

Figure IV.1. Solar disc observed by *SOHO*/EIT 304 Å on September 14th, 1999
Credit: *ESA*/NASA – *SOHO*/EIT

The 304 Å line is emitted by He II at around 50,000 K from the chromosphere and transition region. This very bright spectral line has been critical to CME science for over two decades, as it was selected as the principle emission line in one of the narrow-band filters of Sun-observing telescopes such as *SOHO*/EIT, *STEREO*/EUVI, and most recently *SDO*/AIA. Figure IV.1 shows a brilliant prominence that erupted on September 14th, 1999, observed by *SOHO*/EIT. Also seen in the image are dark quiescent filaments nestled in the chromosphere.

Filaments erupting close to the Sun center, like the August 4th, 2011 filament eruption shown in Figure III.2, are observed as dark absorption features in 304 Å. This is because the filament structures lie along a line of sight ahead of the chromosphere which is very bright in the 304 Å channel, and since the filament temperature is very low, H and He neutral species are very abundant and can absorb the 304 Å radiation. In fact, large fractions of geo-effective CMEs are associated with filaments that erupt close to the Sun center (Gopalswamy et al. 2003) making these transient observations in 304 Å absorption critical to our knowledge of geo-effective space weather. Current EUV diagnostic techniques for optically thick plasmas however, are unable to accommodate the line of sight emission contributions in 304 Å observations by the filament itself and/or its hotter background. The evident way to overcome this issue is to avoid the 304 Å observations (e.g. Williams et al. 2013, Lee et al. 2017) and instead use a channel such as 335 Å which does not have emission contamination, although its lower effective area causes it to detect significantly lower count rates.

However, this prevents us from taking advantage of the excellent 304 Å observations which are available from numerous Sun-observing telescopes. Since filaments are cold, they emit lines from low ionization ions, and the only *SDO/*AIA channel dominated by such lines is 304 Å. As discussed in Chapter III, 304 Å is essential for diagnostics when the count rates of the 335 Å channel are not large enough to participate in diagnostic analysis. Surpassing the controversies of the 304 Å channel is important for an accurate quantification of filament dynamics and energetics and will be central to the discussion in this chapter.

IV.2. Quantifying Emission in 304 Å Observations of the August 4th, 2011 Filament Eruption:

The measurements for the temperature and density of the filament eruption presented in Chapter III would be valid only in the absence of emission in 304 Å. Since this may not be true, it is important to quantify how significant the emitted flux is along the line of the sight for these observations. The flux of photons observed by *SDO/*AIA along the line of sight can be estimated by the following equation:

$$F_{SDO/AIA} = \frac{1}{4\pi d^2} N_e^2 G(T, N_e) AL$$ **Equation IV.1**

The above equation assumes an isothermal plasma at constant density. *d* is the distance between the Sun and spacecraft, N_e is the electron density, $G(T, N_e)$ is the contribution function from CHIANTI as a function of temperature and electron density, A is the area of an AIA pixel in cm^2, and L is the line of sight depth of the filament plasma.

The contribution function includes the atomic physics necessary for the line formation, is mostly independent of electron density for the He II 304 Å line at the high densities of the plasma under scrutiny, but peaks sharply with temperature owing to their dependence on ion abundance. The *gofnt.pro*[9] CHIANTI code gives the $G(T, N_e)$ function described in Equation IV.2. Note that different codes define G(T, N_e) slightly differently.

$$G(T, N_e) = \frac{1}{4\pi} * \frac{N(X_j^{m+})}{N(X^{m+})} * \frac{N(X^{m+})}{N(X)} * \frac{N(X)}{N(H)} * \frac{N(H)}{N_e}$$

Equation IV.2

In the above equation, the red term is the relative level population, which is the fraction of ions in the volume that are in the upper level of the 304 Å transition, calculated using the interplay between excitation and de-excitation processes. The green term is the relative ion population, which depends on the interplay between ionization and recombination processes. The olive term is the abundance of the ion X relative to hydrogen. Finally, the orange term is the ratio of the total hydrogen density to electron density, calculated using the *proton_dens.pro* CHIANTI code. The red, green, orange, and olive terms can be accessed from the CHIANTI database and computed using ionization equilibrium, which we can safely assume for the filament plasma under consideration as discussed in Section III.8.1.

[9] http://www.heliodocs.com/php/xdoc_print.php?file=$SSW/packages/chianti/idl/emiss/gofnt.pro

One way to qualitatively assess the emitted flux from the filament along the line of sight by the He II 304 Å and incident on the AIA detectors is to *investigate the temperature dependence of Equation IV.1. This would aid in understanding of how emission evolves in the temperature range of the filamentary plasma under scrutiny*, without having to compute the line of sight filling factors which cannot be obtained with high certainty. The electron density is calculated from the measured values of column density using temperature-dependent functions from *read_ioneq.pro* and *proton_dens.pro* as described in Section III.6. For the purposes of this analysis, the temperature-dependent portion of Equation IV.1 is contained in the contribution function and electron density. The electron density can be rewritten as:

$$N_e = \frac{n_L}{L} * \frac{nH_{total}}{n_{H\,I}} * \frac{n_e}{nH_{total}}$$ **Equation IV.3**

The electron density is expanded into three terms: (1) the neutral hydrogen density (*$n_{H\,I}$*) which can be computed from the measured values of column density *(n_L)* and line of sight depth (*L*) following Equation III.4, (2) $n_{H\,I}/nH_{total}$ is the ratio of neutral hydrogen density to total hydrogen density from *read_ioneq.pro*, and (3) nH_{total}/n_e is the ratio of total hydrogen density to electron density from *proton_dens.pro*. Terms (2) and (3) take temperature as an independent variable input; hence, the temperature dependent portion of Equation IV.1 can be written as the following function F_{temp}:

$$F_{temp} = G(T, N_e) * \frac{1}{[\frac{n_{H\,I}}{nH_{total}} * \frac{nH_{total}}{n_e}]^2}$$ **Equation IV.4**

Figure IV.2. shows a plot of F_{temp} versus temperature. nHI/nH_{total} and nH_{total}/n_e drop rapidly between log T (K) = 4.0 - 4.5 and G(T) peaks around log T (K) = 5.0. Hence, the F_{temp} function drops very rapidly from 10^5 K to 10^4 K in the temperature range of the filamentary plasma, implying *the emission contribution drops significantly as the plasma cools down.* Furthermore, an inspection of the $G(T, N_e)$ of the 304 Å doublet shows that its emission peaks at around Log T=4.9, so that the measured temperatures imply a rather low emissivity for this line.

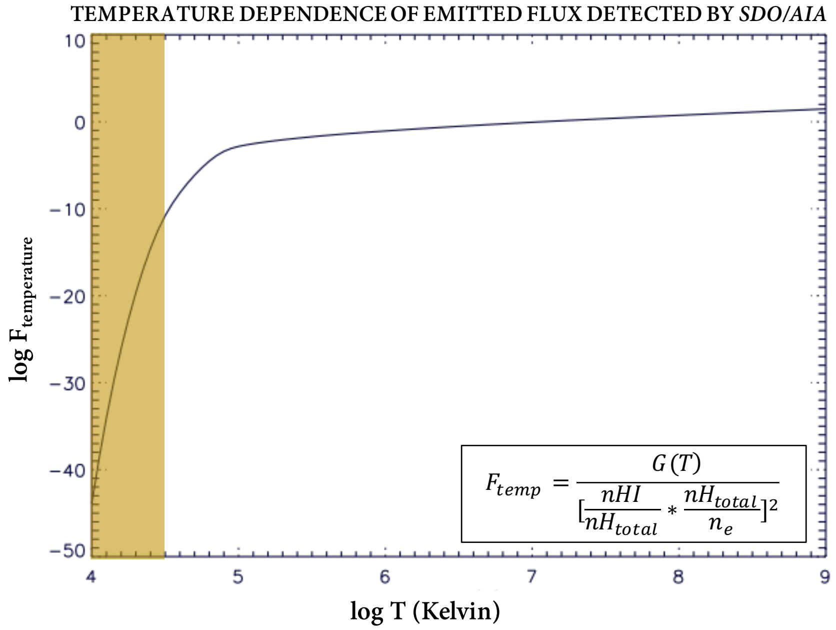

Figure IV.2. The above graphic shows the temperature dependent function (F_{temp}) within the emitted flux incident on an SDO/AIA detector (Equation IV.4) in the 10^4 – 10^9 Kelvin. The shaded area in the plot represents the range of temperature seen in the filamentary plasma analyzed in Chapter III, where a drastic drop in emission contribution is observed.

In order to estimate the expected emission in 304 Å, we make some crude estimates using Equation IV.1. With $N_e=10^{11}\ cm^{-3}$ (based on estimates in Section III.6), $G(T)=1.06\ x\,10^{-16}$ *photon* $cm^3\ s^{-1}\ sr^{-1}$ at $log\ T(K) = 4.5$ for He abundance=0.05, $L=0.3$ *solar radii*, $A=1.96\ x\ 10^{15}\ cm^{-2}$ and an AIA calibration factor[10] of *0.038* , $F_{SDO/AIA} \sim 582\ DN/s$. An extremely low filling factor is required to bring down these values to observed levels (5-10 DN/s), rendering our approximation of unity filling factor invalid.

Furthermore, a 0.05 decrease in log temperature values to $log\ T(Kelvin) = 4.45$ reduces the contribution function by an order of magnitude, hence reducing the emission contribution significantly to a value of *~ 56 DN/s,* as demonstrated in Figure IV.2. These counts are still significant and require a very small filling factor to be comparable with the observed *AIA* counts. However, since part of the observed count rates were due to line of sight emission, the temperature of the filament plasma is expected to be lower than the values reported in Chapter III.

As stated previously, this line of sight emission in 304 Å will decrease the temperature of the crossing point in diagnostic plots such as Figure III.4. The column density would not change significantly, since the L(T) values for the others channels are almost constant for large temperature changes. However, corresponding estimates of neutral hydrogen density, proton density, and electron density will be impacted by the shift in temperature estimates.

[10] http://www.heliodocs.com/php/xdoc_print.php?file=$SSW/sdo/aia/idl/response/aia_get_response.pro

The other factor to note is the filament plasma might be heated beyond the maximum height of observation in AIA, in which case it is expected that the line of sight emission contributions increases. A diagnostic technique that does not account for critical emission physics from important 304 Å observations would be insufficient in such cases.

The Landi and Reale (2013) diagnostic technique did not take into account the presence of this emission contribution which limits its application to a variety of solar transient observations. In this chapter we present an improved diagnostic technique, which extending the diagnostic capabilities on 304 Å observations to include contributions from He II emission along the line of sight. More realistic measurements of the filament's physical properties will allow for rigorous, observation-based discussion of the evolution of the heating and energetics of the filamentary plasma at high cadence, an open question in CME science.

The new EUV diagnostic technique is described in the following Section IV.3. This technique is applied to the August 4th, 2011 filament eruption. The results of column density and temperature, in comparison with results from Chapter III, obtained using the Landi and Reale (2013) technique are presented. Section IV.4 described the results of neutral hydrogen density, proton density, electron density, and ionization history of the filament plasma, along with a comparison with values presented in Chapter III. Section IV.5 is a discussion of the energetics of the August 4th, 2011 filament eruption.

IV.3. New EUV Diagnostic Technique:

The diagnostic tool proposed in this chapter builds on the Landi and Reale (2013) diagnostic technique (Section III.4.1) by expanding its applicability to a wider range of observations where emission contributions may be substantial and improving the accuracy of the corresponding diagnostic results.

Similar to Landi and Reale (2013), this new EUV diagnostic technique capitalizes on the temperature dependence of the effective absorption coefficient in three EUV wavelength regions [100-228 Å, 228-504 Å, 504-912 Å] when the plasma temperature exceeds 15,000 K. Each of these wavelength ranges are defined by the absorption edge of one of these three ions: 228 Å for He II, 504 Å for He I, and 912 Å for H I, beyond which the ions stop absorbing. We account for the behavior of H I, He I, and He II only since they are the most abundant elements of the solar plasma. In order to incorporate the contributions from the line of sight emission in the observations of the optically thick plasmas we revert to the Swartzchild Equation of radiative transfer which states that:

$F_{obs} = F_{inc}e^{-\tau} + \int_0^\tau F_{em}e^{-\tau}d\tau$ **Equation IV.5**

where, $F_{em} = \frac{1}{4\pi d^2} N_e^2 G(T, N_e) AL$ **Equation IV.6**

Here, F_{inc} is the flux hitting the plasma from behind, away from the detector and, F_{abs} is the measured flux that also includes the emission contribution, τ is the optical depth, and F_{em} is the emission from the plasma parcels along the line of sight. The first part of

Equation IV.5 is the ‘sink term’ describing the attenuation of the line of sight emission due to absorption (Equation III.1), and the second half of Equation IV.5 is the ‘source term’ describing the enhancement of the intensity due to line of sight emission.

Integrating the source term in Equation IV.5 from [0, τ] and assuming F_{em} is constant, we isolate τ to one side of the equation. The optical depth of the absorbing and emitting plasma is:

$$\tau = -\ln\left(\frac{F_{obs}-F_{em}}{F_{inc}-F_{em}}\right)$$ **Equation IV.7**

We can hence define a new L function for any spectral line or narrow-band imaging channel we consider. The L function is the column density at the absorbing temperature and can be written as the optical depth divided by the effective absorption coefficient (Equation III.3). Hence,

$$L(T,\ N_e) = -\frac{1}{k_{eff}}\ln\left(\frac{F_{obs}-F_{em}}{F_{inc}-F_{em}}\right)$$ **Equation IV.8**

Since the column density is a property of the absorbing material, the L function would have the same value at the absorbing temperature for all spectral lines. If you set F_{em} to zero in Equation IV.8, it takes the form of Equation III.6 from the Landi and Reale (2013) diagnostic technique. This implies that this new technique can be equally applied to emitting and non-emitting EUV channels, and it indicates that the Landi and Reale (2013) equation was a specific case of this function; one in which there is no emission from the plasma parcels.

This proposed technique is tested on observations of the August 4th, 2011 filament eruption described in Chapter III. This will allow for: an all-encompassing comparative analysis of the results from the two techniques; to quantify the effects of He II 304 Å line of sight emission; and to test the strength of this technique. Observations from 171 Å, 193 Å, 211 Å, and 304 Å *SDO/AIA* channels are used for plasma parcels with the filament eruption along the three paths described in Figure III.2.

In Equation IV.8, $F_{em} = 0$ for 171 Å, 193 Å, and 211 Å because no lines from ions formed below log T (Kelvin) ~ 5.0 are strong enough to contribute with emission in their band passes. Therefore, $L(T, N_e)$ for these channels are identical to the functions used in the previous diagnostic technique. The $L(T, N_e)$ function for the 304 Å channel requires a range of temperature and column density values to compute the $G(T, N_e)$ values.

A closer look at Equation IV.8 shows that the both sides of the $L(T, N_e)$ function are dependent on column density, due to the added factor of F_{em} (Equation IV.6) on the right hand side. In the Landi and Reale (2013) diagnostic technique, the right hand term in Equation III.6 was simply proportional to the column density. In order to satisfy the column density and temperature dependence of the right-hand side of Equation IV.8, presented here is a theoretical method to compute F_{em} over a range of independent variable inputs for temperature and column density.

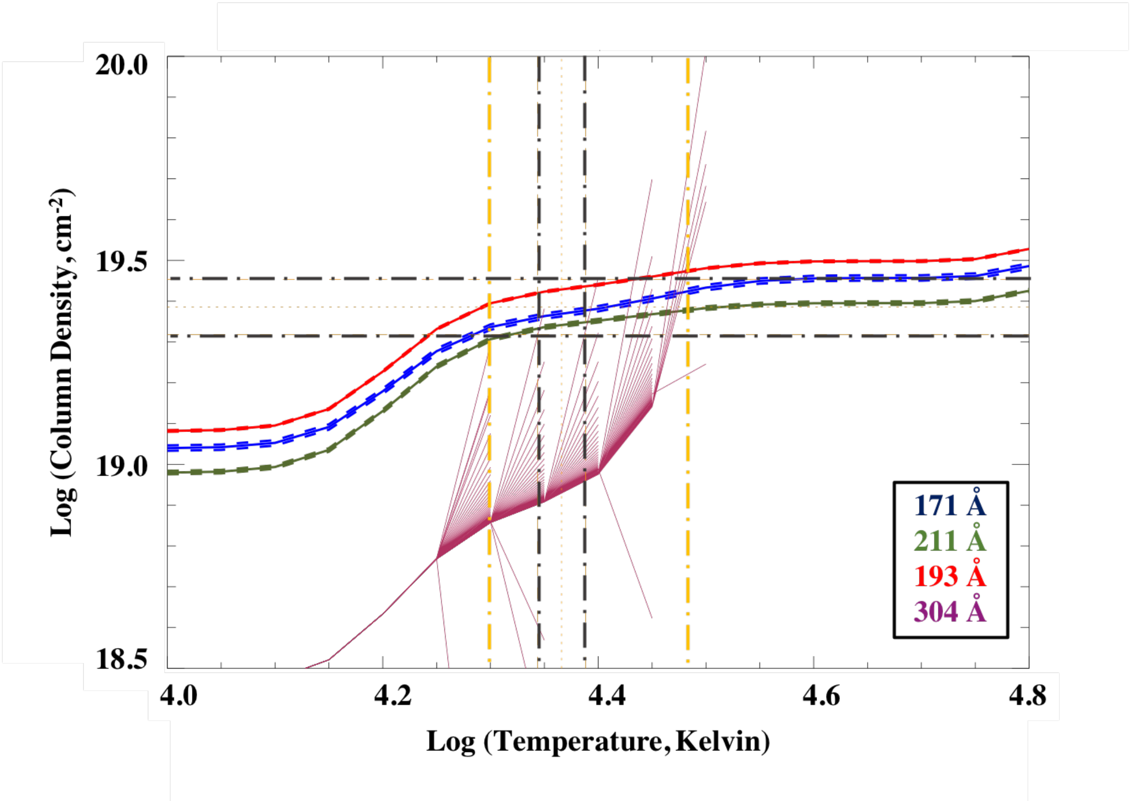

Figure IV.3. Diagnostic results for the absorbing plasma parcel location at 04:23 UT along Path 1. The y-axis is the L(T, N_e) function or the column density (cm^{-2}) and the x-axis is the logarithm of temperature (K). The region where the range of 304 Å L-functions intersect with the remaining L-functions is contained within the vertical dashed yellow lines and the horizontal black dashed lines. The final range of temperature values is determined by the vertical black dashed lines, representing the range of temperatures within which the 304 Å L functions have self-consistent column density values.

Temperature is varied between log T (Kelvin) = [4, 9] and column density is varied between log n_L (cm^{-2}) = [17, 22] to compute a grid of values for $G(T, N_e)$ following Equation IV.2. Substituting the contribution function grid into Equation IV.6 gives 2D arrays of F_{em} and corresponding $L(T, N_e)$ values for the 304 Å channel can be computed from Equation IV.8. Hence in 304 Å, for each potential value of column density, we have L-function profiles over a range of temperatures. The $L(T, N_e)$ functions for 171 Å, 193 Å, 211 Å, and 304 Å channels are plotted for each time step between 4:10 UT – 05:00 UT for the 30x30 pixel plasma parcels along Paths 1, 2, and 3. The *$L(T, N_e)$* plot for the timestep corresponding to Figure III.4 along Path 1 is shown in Figure IV.3.

The first notable difference between Figure IV.3 and Figure III.4 is the many 'prongs' of the 304 Å line. Each of these lines represents the 304 Å L(T) function for a distinct value of column density between log n_L (cm^{-2}) = [17, 22]. The horizontal black dashed lines represent the range of intersections along the y axis, giving us a minimum and maximum limit for column density for the plasma parcel for this location and time. The yellow vertical dashed lines represent the range of intersections in the x-range. Within these yellow lines lie a number of purple 304 Å prongs that were each computed theoretically using a different value of column density over a range of temperatures. It needs to be ensured that each of these 304 Å lines within this box are consistent with the column density range on the y-axis of this plot (horizontal black lines). However, some of the 304 Å prongs are inconsistent with the column density range, reducing the range of temperature values. This new temperature range is represented by the vertical dashed lines.

Diagnostic results such as those shown in Figure IV.3 were produced for 102 timestamps between 04:10 UT - 05:00 UT for all three plasma trajectories within the filament (Figure III.2). Similar to the results from the Landi and Reale (2013) diagnostic technique, distinct intersections in the *$L(T, N_e)$* were obtained for approximately the first 20-25 minutes of analysis for the three plasma paths, allowing for good measurements of the column density and temperature at these times. The resulting column density values are shown in Figure IV.4. and the resulting temperature values are shown in Figure IV.5. Also seen in Figures IV.4 – IV.5 are dashed lines, which are the measurements derived using with the Landi and Reale (2013) diagnostic technique.

Comparing the results of diagnostics where He II emission in 304 Å was not considered (Figure III.4) with where the emission is accounted for (Figure IV.3), we see the crossing point of the curves distinctly shifts to the left, implying a lower temperature value, reported in Figure IV.5. This corroborates the preliminary estimation of how the results would change in Section IV.2. The trends from the regions marked red are ignored due to higher uncertainties in measurement. Figure IV.4 shows that the column density decreases by a small factor as well.

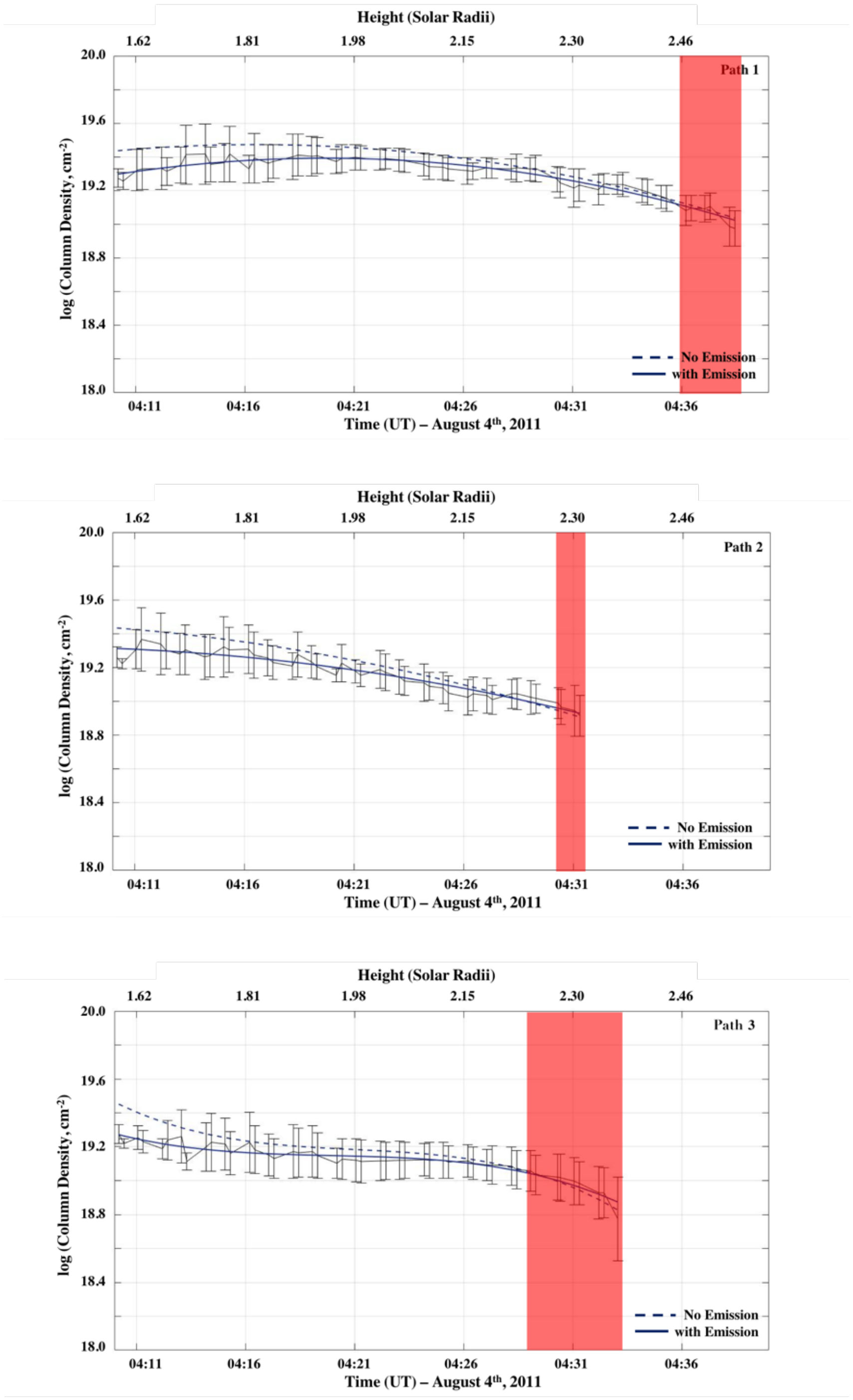

Figure IV.4: The y-axis shows logarithm of column density (cm^{-2}) versus time (UT) on the bottom x-axis and the corresponding approximate height (solar radii) of the filament plasma parcels on the top x-axis, for Paths 1, 2, and 3. The dotted lines are results from the Landi and Reale (2013) diagnostic technique where He II 304 Å emission was not considered. The solid lines are results from the new diagnostic technique, described in Section IV.2. The regions shaded red had very high uncertainties in measurements from the new diagnostic technique.

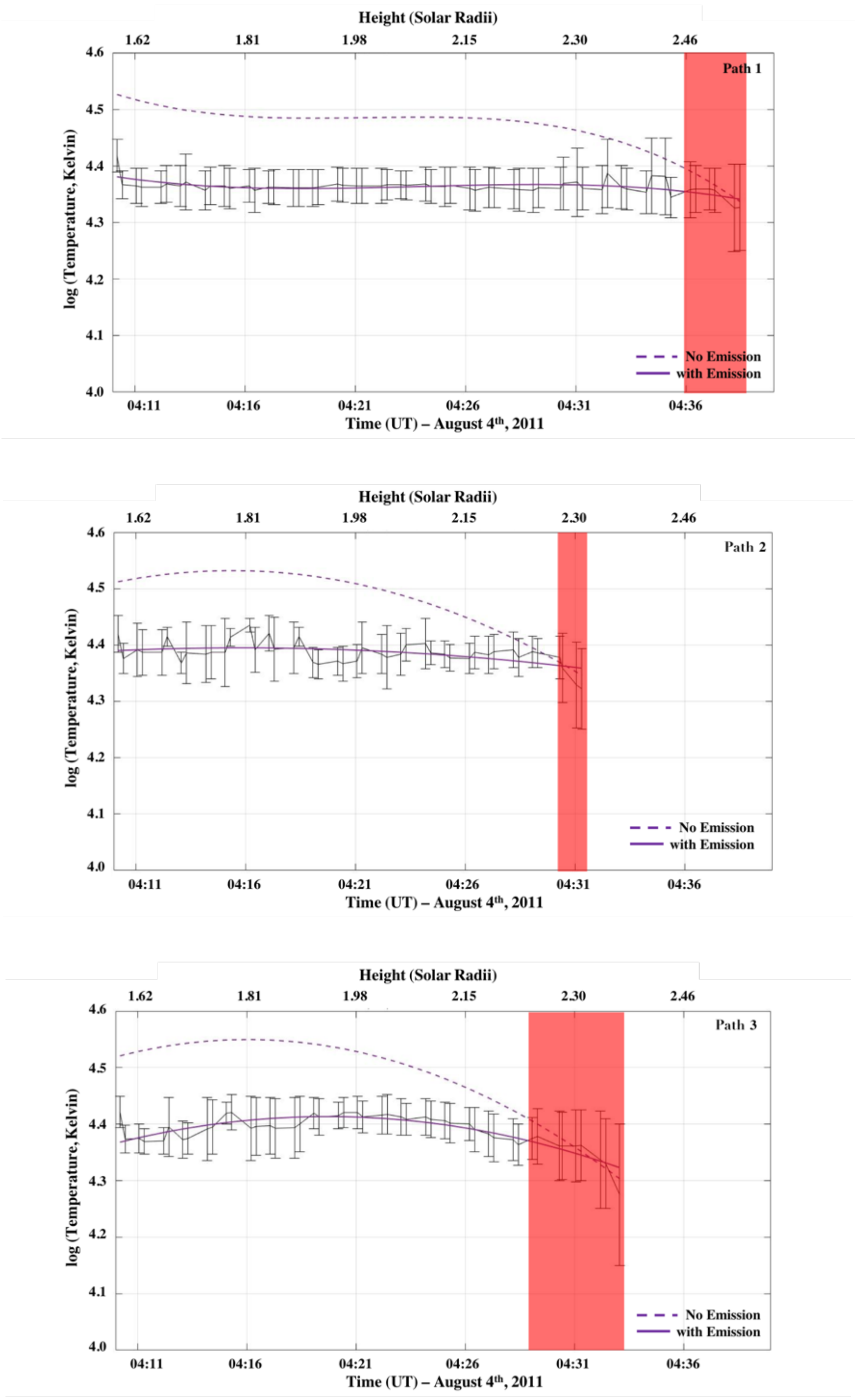

Figure IV.5: The y-axis shows logarithm of temperature (Kelvin) versus time (UT) on the bottom x-axis and the corresponding approximate height (solar radii) of the filament plasma parcels on the top x-axis, for Paths 1, 2, and 3. The dotted lines are results from the Landi and Reale (2013) diagnostic technique where He II 304 Å emission was not considered. The solid lines are results from the new diagnostic technique, described in Section IV.2. The regions shaded red had very high uncertainties in measurements from the new diagnostic technique.

IV.4. Comparing the Two Diagnostic Techniques:

Neutral H density, Proton Density, Electron Density, Ionization History

Using the measurements of column density and temperature from the new diagnostic technique (Section IV.3) and under the tested condition of near ionization equilibrium, the evolution of hydrogen and electron densities are estimated over the course of the filament plasma trajectory. The average lower limit to the neutral hydrogen density can be directly computed from the column density if the line of sight depth of the absorbing parcel is known following Equation III.4. Evolution of neutral hydrogen density is shown in Figure IV.6. The proton density (Figure IV.7) is computed using the read_ioneq.pro CHIANTI code, and the electron density (Figure IV.8) is computed using the proton_dens.pro CHIANTI code. The dotted lines in Figures IV.6 – IV.8 represent the corresponding values computed using the Landi and Reale (2013) diagnostic technique where 304 Å He II emission was not considered (Figures III.9 – III.10).

The values of all parameters are found to be lower from the estimates made using the Landi and Reale (2013) diagnostic technique. The trends of neutral hydrogen density remain mostly unchanged, when computed with or without 304 Å He II emission, but their values were slightly lower when emission was taken into account. More notably, the values of proton and electron densities are over an order of magnitude lower for most of the measurement period. This is due to the lower temperatures, which reduces the fraction of ionized hydrogen, leading to a lower overall hydrogen content.

These lower density measurements are more consistent with the results of estimates of filament plasma densities. The proton and electron densities also drop more gradually than the values reported in Section III.6. It is possible that the filament was exposed to a greater rate of heating during this initiation phase of its evolution in the low solar corona than reported in the previous chapter, since even though the temperatures are lower, they remain essentially constant. Conversely, the total hydrogen content is also lower, implying the heating might in fact be lower compared to the results computed ignoring 304 Å He II emission.

As describes in Section III.7, the ionization history of the filament plasma is determined using the Michigan Ionization Code (MIC), including impacts of photoionization and flare heating. Determining the ionization history of the filament plasma using the more accurate diagnostic results is imperative to determining if the plasma is indeed in ionization equilibrium and whether the charge states in the filamentary material were frozen in around the maximum height where it was observed in absorption.

Results of the MIC are shown in three sets of plots in Figure IV.9. The top set of plots is for Path 1, the middle set is for Path 2, and the bottom set is for Path 3. The bottom panel in each set shows the evolution of the relative abundance, represented with color bars, of the charge states of C, N, O, and Fe to the total abundance of their respective elements, as the plasma parcels within the filament travel from 1.6 to 2.3 solar radii. The top panel in each set shows the relative abundance of the charge states of C, N, O, and Fe to the total abundance of their respective elements at the maximum height of the plasma parcels along the measured trajectories.

The charge states are not yet frozen in, the ionization equilibrium assumption is valid, and a single charge state dominates each ion. However, there are some notable differences between the ionization plots in Figure IV.9 and ionization plots computed with data where 304 Å He II emission was not considered (Figure III.11). Iron shows lower ionization states while carbon, nitrogen, and oxygen have higher ionization states (oxygen showing the most notable difference), compared to the values computed without emission. This can be ascribed to lower density and temperature values estimated with a more accurate diagnostic technique. A colder and less dense plasma would imply lower ionization of the iron charge states. The higher oxygen charge states could be because oxygen does not recombine as much due to the lower plasma densities, and mostly constant temperatures. In the results where 304 Å He II emission was ignored, the filament plasma was cooling more rapidly and had much greater electron density, hence recombination was much more effective.

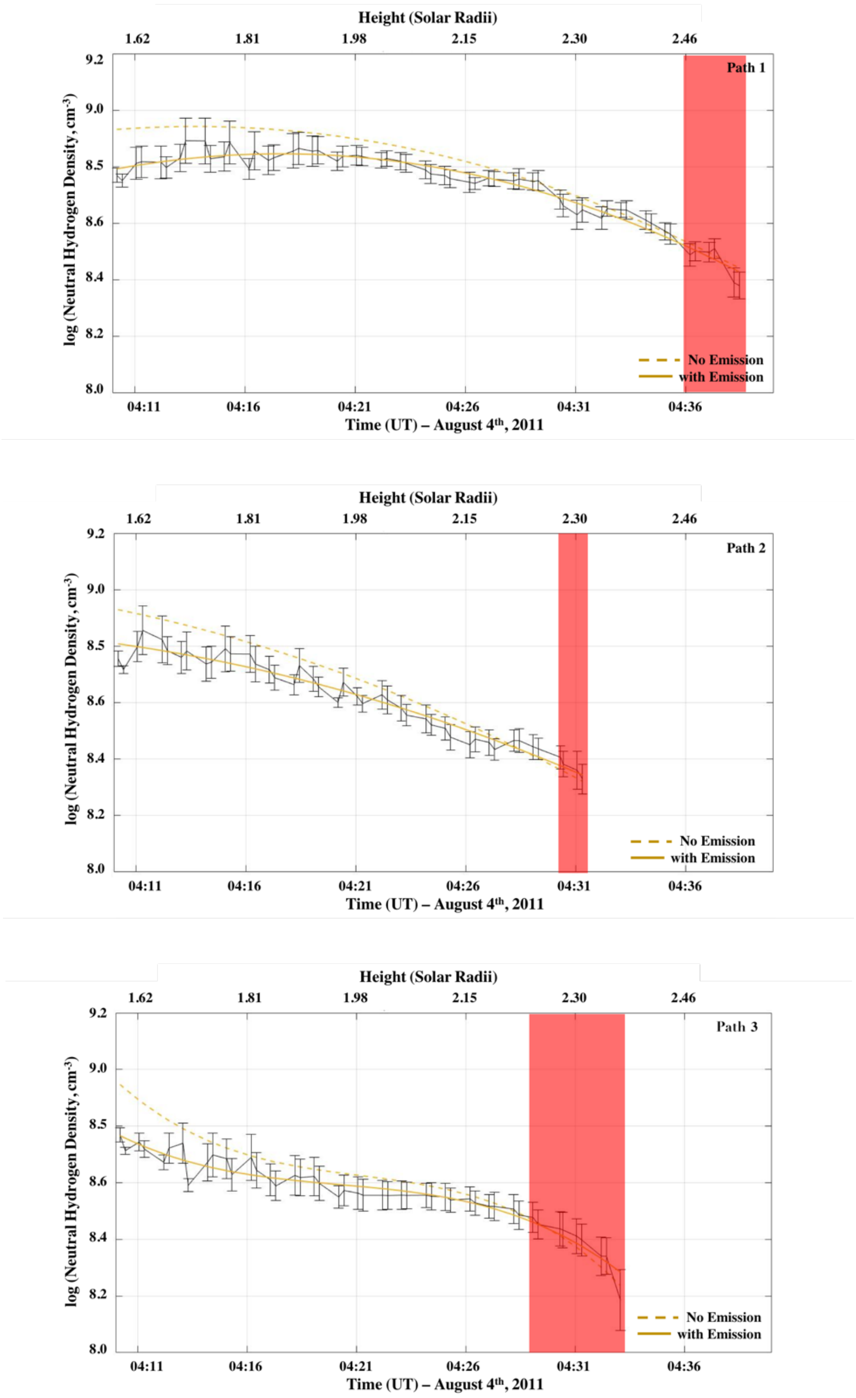

Figure IV.6: The y-axis shows logarithm of neutral hydrogen density (cm^{-3}) versus time (UT) on the bottom x-axis and the corresponding approximate height (solar radii) of the filament plasma parcels on the top x-axis, for Paths 1, 2, and 3. The dotted lines are results from the Landi and Reale (2013) diagnostic technique where He II 304 Å emission was not considered. The solid lines are results from the new diagnostic technique. The regions shaded red had very high uncertainties in measurements from the new diagnostic technique.

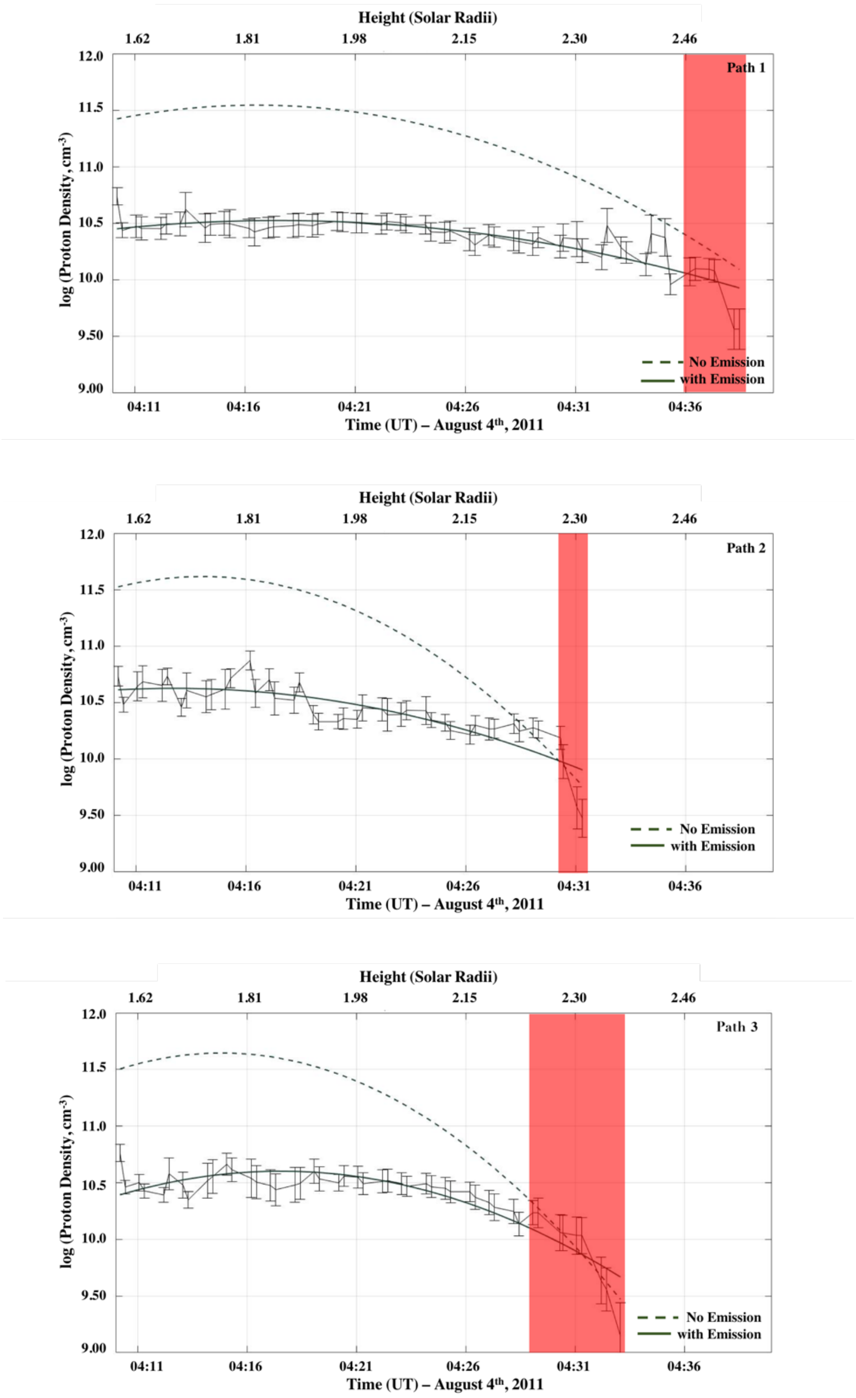

Figure IV.7: y-axis shows logarithm of proton density (cm^{-3}) versus time (UT) on the bottom x-axis and the corresponding approximate height (solar radii) of the filament plasma parcels on the top x-axis, for Paths 1, 2, and 3. The dotted lines are results from the Landi and Reale (2013) diagnostic technique where He II 304 Å emission was not considered. The solid lines are results from the new diagnostic technique. The regions shaded red had very high uncertainties in measurements from the new diagnostic technique.

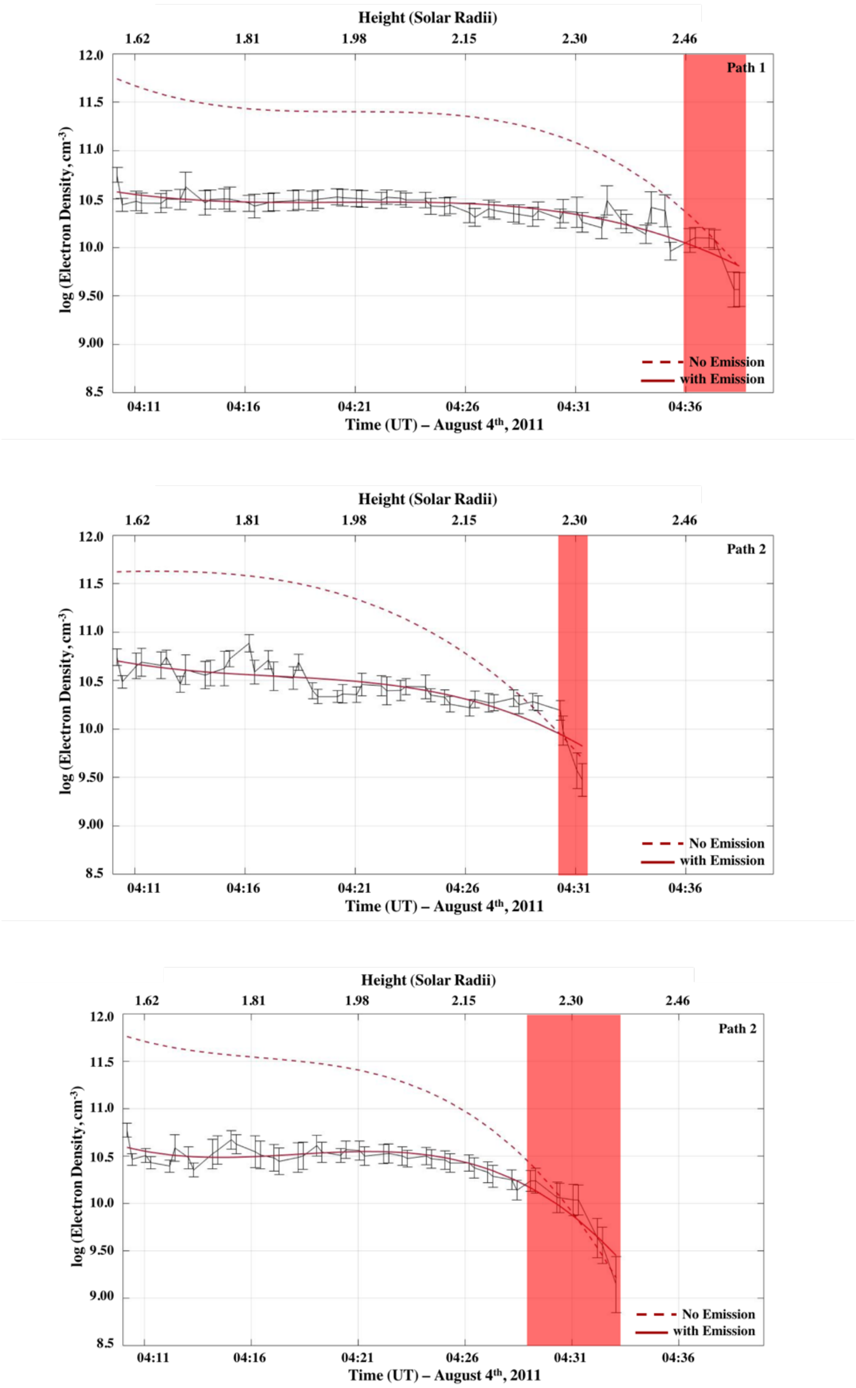

Figure IV.8: y-axis shows logarithm of electron density (cm^{-3}) versus time (UT) on the bottom x-axis and the corresponding approximate height (solar radii) of the filament plasma parcels on the top x-axis, for Paths 1, 2, and 3. The dotted lines are results from the Landi and Reale (2013) diagnostic technique where He II 304 Å emission was not considered. The solid lines are results from the new diagnostic technique. The regions shaded red had very high uncertainties in measurements from the new diagnostic technique.

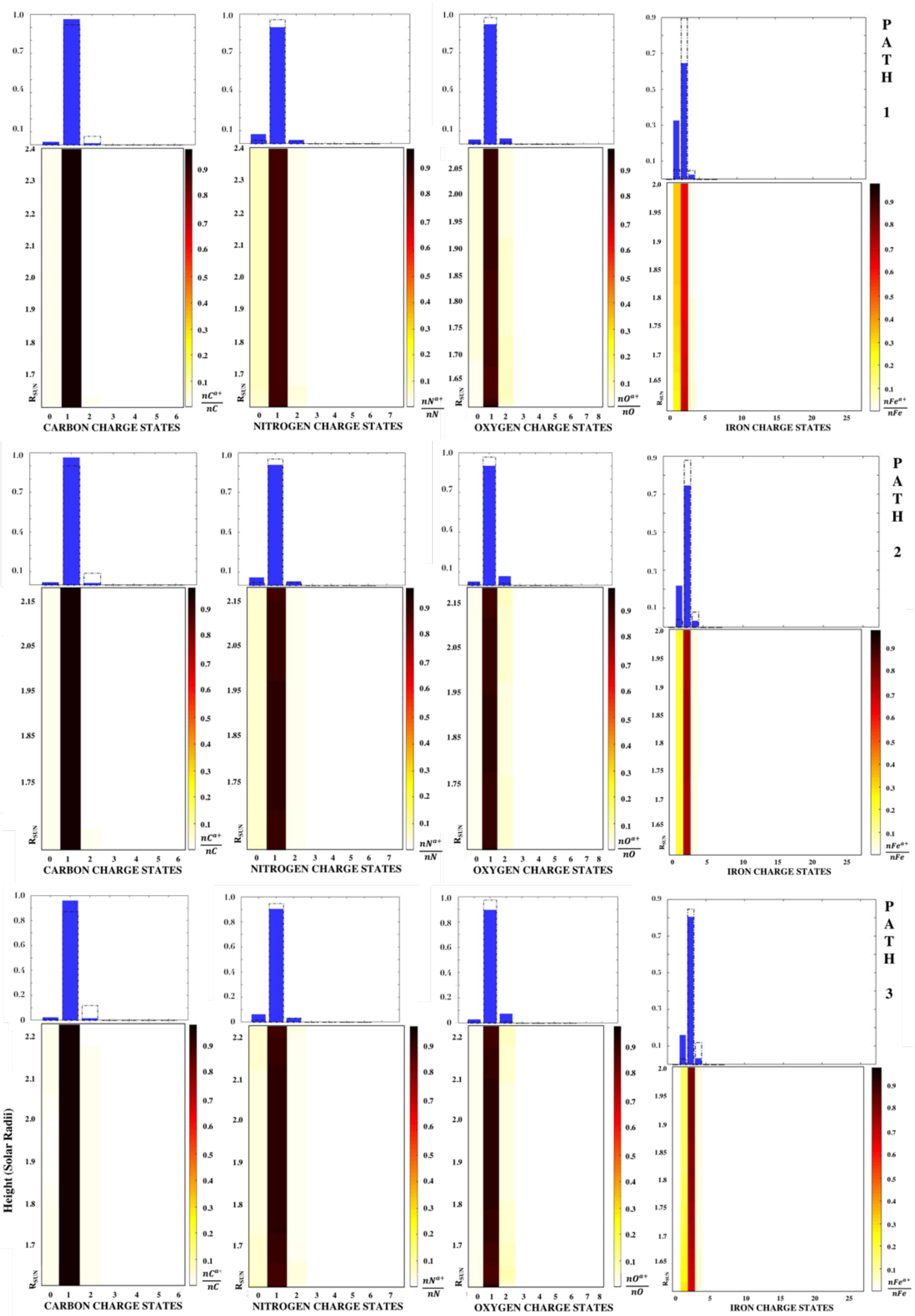

Figure IV.9: Results from Michigan Ionization Code using the measured values of density, temperature from the new diagnostic technique and speed (Section III.5) for Paths 1 (top), 2 (middle), and 3 (bottom). For each path, the bottom set of panels show the evolution of the charge states of Carbon, Nitrogen, Oxygen, and Iron with height, and the top set of panels show the final charge states predicted at the maximum height. The dotted lines in the top panel represent the values of final charge states predicted at the maximum height when 304 Å He II emission was not considered.

IV.5. Energetics of the Filamentary Material

The energy budgets of CMEs include contributions from magnetic energy, bulk kinetic energy, ionization energy, gravitational potential energy, thermal energy, and energetic particles (e.g. Murphy et al. 2011, Emslie et al. 2005). Given the available estimates of kinematic evolution, and thermodynamics using a more realistic diagnostic technique, computation of certain energy terms per unit volume is possible for the filamentary plasma. The magnetic energy of the precursor active region will be estimated by vector magnetograms in a future investigation. Presented in this section are kinetic energy, gravitational potential energy, thermal energy, and radiative cooling per unit volume following the calculations from Lee et al. (2017). The **kinetic energy (KE) per unit volume** is computed using the following equation, where m_p is the mass of protons, n_p is the proton density (Figure IV.8), and v_{bulk} is the bulk velocity of the plasma (Figure III.7, bottom):

$$\frac{KE}{Volume} = \frac{1}{2} m_p n_p v_{bulk}^2$$ **Equation IV.10**

Units of Joules/m^3

The **thermal energy (TE) per unit volume** is computed using the following equation, where n_p and n_e are the proton and electron densities (Figures III.7 – III.8), k_B is the Boltzmann constant, and T is the plasma temperature (Figure III.5):

$$\frac{TE}{Volume} = 3(n_p + n_e) k_B T$$ **Equation IV.11**

Units of Joules/m^3

The **gravitational potential energy (PE) per unit volume** is computed using the following equation, where G is the gravitational constant, M_{Sun} is the solar mass, R_{Sun} is the solar radius, R_{LOS} is the line of sight depth (Figure III.8):

$$\frac{PE}{Volume} = GM_{Sun}m_p n_p \left(\frac{1}{R_{Sun}} - \frac{1}{R_{LOS}}\right)$$ **Equation IV.12**

Units of Joules/m^3

The **radiative cooling term (RC)** is computed using the following equation, where P(T) is computed using the *rad_loss.pro*[10] CHIANTI routine, nH_{total}/n_e is computed using *proton_dens.pro*[5] CHIANTI routine, and Δt is the time interval between successive time steps

$$\frac{RC}{Volume} = \left[\frac{nH_{total}}{n_e}\right] * n_e^2 * P(T) * \Delta t$$ **Equation IV.13**

Units of Joules/m^3

The different energy terms described in Equations IV.10 – IV.13 are shown in Figure IV.10 for Paths 1, 2, and 3. For the radiative cooling term, a smooth quadratic fit is used to remove the localized fluctuations of Δt between 12-24 seconds in consecutive time steps. For all three paths, in the time where the measurements were trustworthy:

Gravitational Potential Energy > Kinetic Energy > Radiative Cooling > Thermal Energy

---

[10] http://www.heliodocs.com/php/xdoc_print.php?file=$SSW/packages/chianti/idl/emiss/rad_loss.pro

The kinetic energy and potential energy increased slightly until ~1.8 - 1.9 R_{SUN} followed by a gradual decrease. The thermal energy and radiative cooling terms remain mostly constant followed by a steady drop between 2.15 R_{SUN}.

Some notable results of CME energy budgets from Akmal et al. (2001), Lee et al. (2009), Landi et al. (2010), and Murphy et al. (2011) were mentioned in Chapter I of this dissertation. The findings presented here are consistent with those of studies such as Akmal et al. (2001) and Lee et al. (2009) who found heating to be a significant portion of the energy budget of the CMEs.

While the results of this investigation have similar trends as those discussed in Landi et al. (2010) for their observations of the April 9th, 2008 CME core at 1.1 R_{SUN} and 1.9 R_{SUN}, there are some notable differences. The radiative loss estimates for the filament analyzed in this study are lower than those estimated for the CME core described in Landi et al. (2010) because the very cold filamentary material analyzed here has a significantly lower radiative loss rate based on CHIANTI estimates. Also, while the CME analyzed in Landi et al. (2010) has similar kinetic and thermal energies, the thermal energy is much smaller than the kinetic energy for the filament investigated here. This can be attributed to a few differences between the cases utilized in the two investigations: (1) the erupting filament analyzed in this study is colder, and (2) the filament eruption in the current study is analyzed at higher heights in the corona where the speed is three to four times greater than the eruption considered in Landi et al. (2010).

Furthermore, the Differential Emission Measure (DEM, which described the thermal structure of a multi-thermal plasma) analysis conducted in Landi et al. (2010) used spectral lines corresponding to temperature's greater than log T (Kelvin) = 4.9, leaving out crucial information on colder core plasma. The results of filament energetics presented here are expected to be more accurate since the new diagnostic technique introduced in this chapter covers a wide range of plasma temperatures, specifically accounting for the very cold plasmas.

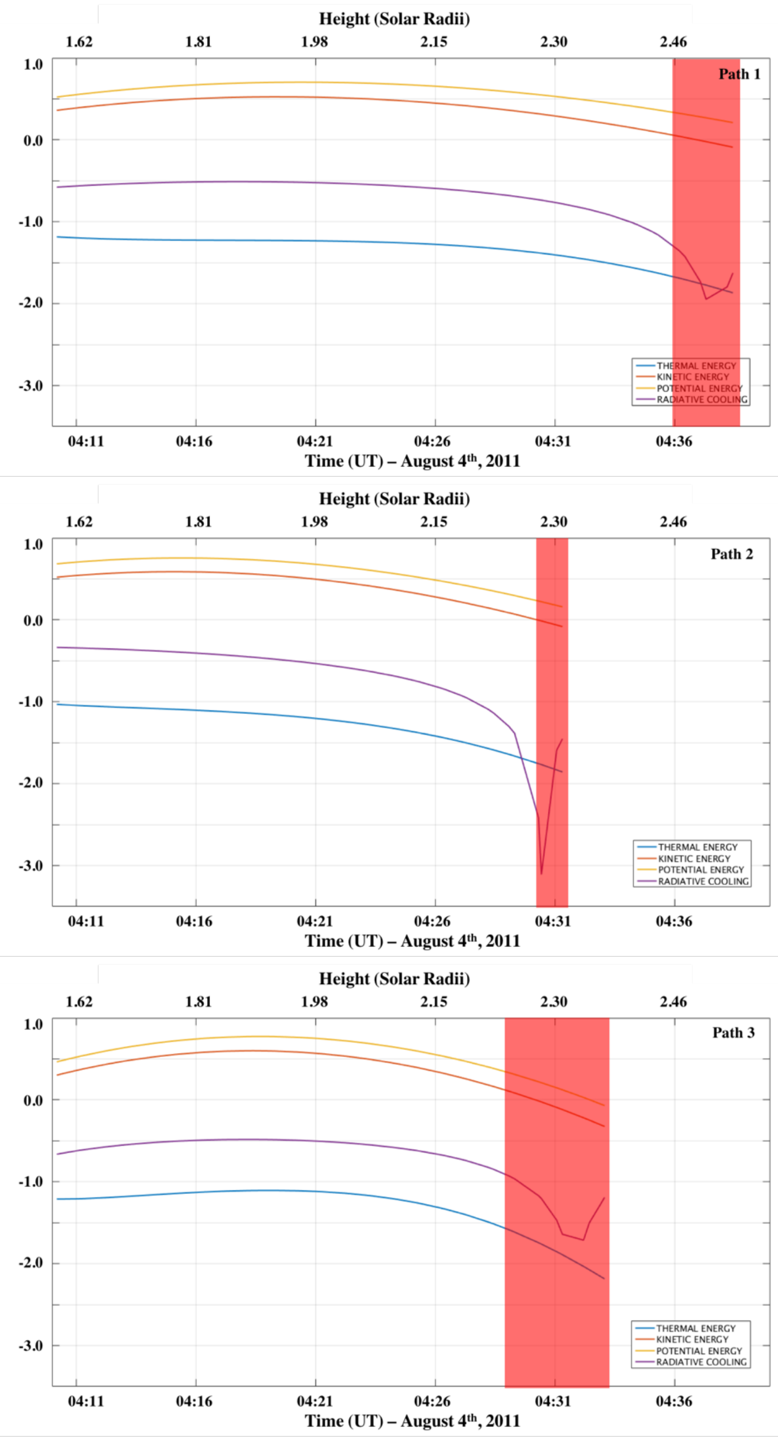

Figure IV.10: The above plots show logarithm of the thermal energy (blue line), kinetic energy (orange line), potential energy (yellow line), and the radiative cooling term (purple line), computed per unit volume (Joules/m^3), for the filament plasma followed along Paths 1 (top), 2 (middle), and 3 (bottom). The regions shaded red had very high uncertainties in measurements from the new diagnostic technique.

CHAPTER V

Conclusions and Future Work

ACE/SWICS has provided us with the most complete set of composition data to date of solar wind incident at 1 AU. *SDO*/AIA provides us with an unprecedented view of the solar corona in multiple wavelength bands, with images that span over 1.3 solar diameters at high-cadence and spatial resolution. AIA and SWICS were central to the series of investigations described in this dissertation, and, along with instruments on board *SOHO* and *STEREO,* were used to explore the following three overarching CME science topics:

(1) in-situ signatures of CME processes in the low solar corona,
(2) evolution of filament composition in the low solar corona, and
(3) evolution of filament dynamics and energetics in the low solar corona.

In Chapter II, an in-depth analysis of in-situ observations of 14 years of Earth-intercepting ICMEs and associated compositional anomalies was discussed. The investigation began with the departure of C^{6+}/C^{5+} and O^{7+}/O^{6+} from their expected correlation occurring in ~45% of ICMEs ("depleted ICMEs"), and distinct compositional and thermal trends associated with these events were reported. The “Depletion Region” was identified as the region within the depleted ICMEs that can be demarcated by this anomalous behavior. *The most consistent characteristics of the Depletion Region were (1) depleted fully stripped ions of helium, carbon, nitrogen, and oxygen, and (2) exposure to some source of heating, before/around the time the charge states froze-in.* Notably, the depleted ICMEs outside of the Depletion Region were compositionally and thermally identical to the non-depleted ICMEs, implying the Depletion Region plasma was subject to a process that did not significantly impact the rest of the ICME plasma. The analysis also concluded that there was no noticeable trend on the location of where in the Depleted ICME the Depletion Region occurred, or its time span.

Magnetic reconnection can generate significant thermal energy, and reconnection in current sheets of CMEs can occur near the freeze-in regions of various ions. This warranted a preliminary investigation into the possibility of the Depletion Region plasma being an in-situ signature of magnetic reconnection in the low solar corona.

Two theories were explored. (1) The Depletion Region was created by the acceleration of the fully stripped ions out of the reconnection region by energetic beams produced during the process of magnetic reconnection; (2) the compositional characteristics of the Depletion Region were a result of fully stripped ions being the only ions not picked up during magnetic reconnection following the criteria described in Drake et al. (2009).

However, this investigation into the coronal source of the Depletion Region requires:
a. statistically significant in-situ measurements sensitive enough to quantify fully ionized states of the other heavy ions (Ne^{10+}, Mg^{12+}, Si^{14+}, S^{16+}, Fe^{26+}), which we expect to also have lower abundances in the Depletion Region;

b. modeling of charge state composition within CME current sheets, along with a greater number of ions than those that are currently modeled;

c. a more rigorous understanding of energetic protons within current sheets and how they can impact the overall CME composition; and

d. understanding of acceleration of different mass/charge ions out of the reconnection exhaust.

Pending this, observations of Depletion Regions in ICMEs could serve as a diagnostic tool for reconnection in CME tails in the low solar corona.

While the research presented in Chapter II of this dissertation was built upon an extensive analysis of in-situ observations of Earth-incident ICMEs, Chapters III and IV of this dissertation were inspired to develop frameworks that used in-situ and remote-sensing observations synchronously to continue the scientific exploration into these consequential CME eruptions.

Filaments are associated with a large fraction of CME eruptions; *when present they constitute the core of the CME and are integral to quantifying the overall energy budget of CMEs.* In order to constrain the physics of CME cores low in the solar corona and the partition of thermal and kinetic energy of their plasmas, Chapter III presented a framework to determine the evolution of the thermal and kinetic properties of a single filament eruption event using the following instruments: *ACE*/SWICS, *SOHO*/LASCO, *STEREO A&B*/SECCHI, and *SDO*/AIA. The case study of a geoeffective ICME that arrived at Earth on August 5th, 2011 was considered. It was traced to the Sun using coronagraphs and imagers onboard *STEREO* and *SOHO*. A 30x30 pixel square plasma parcel within the filament eruption was tracked along three possible paths from 04:10 UT – 05:00 UT in multi-wavelength AIA images on August 4th, 2011 at 12-24 second cadence.

The column density and electron temperature of the plasma were estimated using the absorption diagnostic technique outlined in Landi & Reale (2013). The kinematics of the filament eruption were measured using *STEREO* multi-wavelength images and coronagraphs. Estimates of the line of sight length of the plasma from these images allowed for the calculation of the neutral hydrogen density. The proton and electron densities calculated from the neutral hydrogen density, along with the temperature and speed estimates, served as inputs to the MIC to study the time and spatial evolution of the ionization status of the CME core plasma.

The analysis in Chapter III allows for the high-cadence visualization of the kinematic and dynamic evolution of the filament eruption, leading to some notable inferences about the behavior of the filamentary plasma in the low solar corona. For instance, the charge states of C, N, O, and Fe within the filament were not frozen-in at the height of maximum observation (~2.1 - 2.4 R_{SUN}), beckoning additional investigations using instruments observing the filament eruption further out in the solar corona. The filament plasma experienced additional heating throughout its trajectory, photoionization impacted its ionization history, and the three different plasma trajectories did not have identical behaviors implying the filament was heterogenous.

The overarching goal of the analysis presented in Chapter IV was two-fold: (1) attempt to overcome a fundamental limitation of the Landi and Reale (2013) diagnostic technique, since it was central to a majority of the estimates presented in Chapter III, and (2) with more precise estimates of properties of the filamentary plasma from (1), describe the evolution of the energetics of the filament plasma.

The Landi and Reale (2013) EUV diagnostic technique assumed non-emitting plasmas and thus ignored the contribution of the erupting filament's own emission and/or other emission along the line of sight to the observed count rates in the 304 Å channel. In Chapter IV an improved diagnostic technique is introduced that accounts for emission and absorption contributions from emitting channels such as 304 Å. This diagnostic technique can be equally applied to emitting and non-emitting channels, paving the way for more realistic discussion of the heating and energetics of the filament plasma using a wider range of observations.

A comparison of results of the new diagnostic technique with those presented in Chapter III found that the temperature of the plasma is colder than previously predicted, and column densities were also decreased by a small factor. The values of proton and electron densities were over an order of magnitude lower for most of the measurement period. The charge states were still not frozen in, and the ionization equilibrium assumption once again held up; however, some changes were seen in the ionization profiles. Most notably, oxygen had lower ionization states and iron had higher ionization states than those predicted without considering emission in 304 Å. This was attributed to a colder as well as less dense plasma.

The energy budget of the filament plasma showed that the gravitational potential energy is greater than the kinetic energy, which is greater than the losses due to radiative cooling, and the thermal energy is the lowest term, though significant. In agreement with previous investigations into CME energetics, the filament plasma showed signs of significant heating. However, the thermal energy was not comparable to the kinetic energy as found by other studies. This is attributed to the fact that the filament analyzed here was colder and faster than the CMEs analyzed in previous studies.

The thermodynamic, kinematic, and composition profiles reported in Chapters III and IV were derived from high-cadence measurements of an expanding filamentary plasma tracked in the low solar corona. The new diagnostic technique developed in the course of this work and deployed in Chapter IV allowed for more robust and accurate measurements. This was the first time these quantities were measured at such high cadence and precision over an extended period of time, while attempting to ensure the same plasmas within filamentary eruptions were tracked. These measurements could serve as powerful tools to constrain existing models of CME eruptions, and determine the physical processes of heating and acceleration that shape the eruptions at their source and throughout the low solar corona.

The anticipated future work associated with the research presented in this dissertation can be described into three interconnected phases:

(a) developing new diagnostic/measurement tools and techniques,

(b) running diagnostics on a diverse range of CME events and plasma features, and

(c) conducting observation-model comparisons.

The new EUV diagnostic technique introduced in Chapter IV needs to be refined and its robustness tested. Ionization equilibrium, plasma homogeneity, unity filling factors, and constant emitted flux (F_{em}) were some of the assumptions made while expanding on the applicability and precision of the Landi and Reale (2013) technique. However, attempts will be made to improve the technique over time. An immediate project is applying the new diagnostic technique on an eruption where 335 Å counts were trustworthy in addition to the 304 Å counts. Since the 335 Å channel is non-emitting, a comparison of diagnostic results from the new EUV diagnostic technique compared with those using 335 Å could serve as an effective test of the accuracy of the new technique. The author is motivated to develop tools that the wider scientific community can benefit from, such as this new diagnostic technique.

These diagnostic abilities (in addition to existing diagnostic techniques) will allow for a more extensive and realistic analysis of CME eruptions. The second phase of future investigations associated with the research presented in this dissertation is to conduct detailed and high-cadence diagnostics of different CME plasmas for many more eruptions associated with different pre-eruptive states of CMEs. The goal is to create the most extensive database of CME plasma dynamics and energetics based on multi-instrument observations. The database will allow for comparative analysis of different categories of eruption and robust constraints to CME models.

The third phase of investigation associated with this research is using these extensive measurements to constrain models of CME evolution and compare observations with model results. A schematic of such a plan is shown in Figure V.1. The research presented in this dissertation partially conveyed some of the plan detailed in the top green box. Subsequent empirical comparisons between the observation-based measurements and model results will allow for more rigorous characterization and quantification of the physical processes that govern CME formation at the solar source, as well as the processes that influence CMEs through their heliospheric evolution.

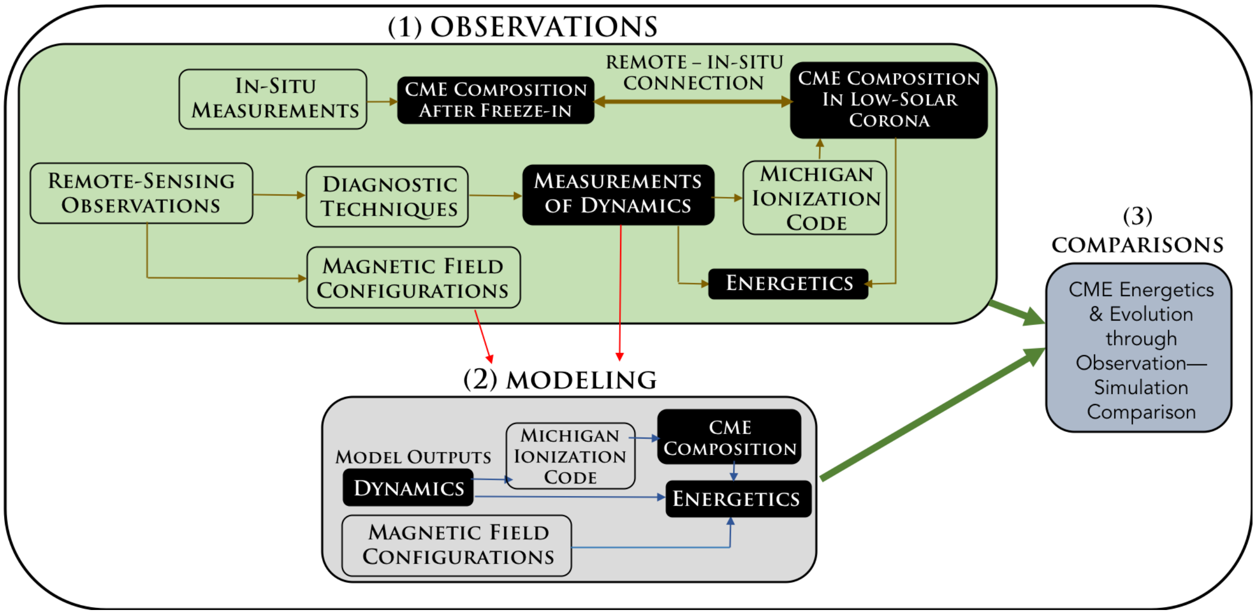

Figure V.1. Schematic showing a framework for potential future projects.

The future work associated with the research presented in this dissertation is rooted in the author's commitment to exploring societally-relevant and exciting scientific endeavors in the fields of solar and heliospheric sciences. Three CME topics were explored in this dissertation: in-situ signatures of CME processes in the low solar corona, evolution of filament composition in the low solar corona, and high-cadence estimates of filament energetics evolution in the low solar corona. This dissertation begins the foundational approach to these topics and sets the stage to utilize future observations to continue answering these questions and beyond.

Parker Solar Probe (*PSP*) will give us unprecedented in-situ measurements from 9-10 R_{SUN} above the photosphere. For instance, the *PSP*/SWEAP (Solar Wind Electrons Alphas and Protons, Kasper et al. 2016) instrument will help shed light on proton properties in reconnection regions, allowing for the Depletion Region hypothesis to the tested. The *PSP*/WISPR (Wide-Field Imager for Parker Solar Probe, Vourlidas et al. 2016) imager will allow us to use images of transients at unprecedented spatial resolution, significantly enhancing the accuracy and details of our measurements. In-situ observations from the Solar Orbiter spacecraft instrument suite, the Solar Wind Plasma Analyzer (SWA), will allow for a new era of investigation into heavy ion charge states that have been utilized throughout this investigation. The new diagnostic technique introduced here could be tailored to suit measurements from the following *Solar Orbiter* remote instruments: the Extreme Ultraviolet Imager (EUI), METIS Coronagraphs, and the Spectral Imaging of the Coronal Environment (SPICE). Remote observations from *PSP* and *Solar Orbiter* can be connected to in-situ measurements made by *Solar Orbiter* via techniques described throughout this dissertation. This will provide us with spectacular opportunities to utilize unprecedented CME measurements and perform series of observation-to-simulation connections to launch us into a new era of solar and heliospheric investigations.

APPENDIX

Reported here are detailed statistics of the comparison of thermal and compositional properties of 41 ionic charge states in the 5 regions of the 148 Depleted ICMEs and 193 non-Depleted ICMEs identified between 1998 and 2011 discussed in Chapter II. The reported percentages of Depleted ICME cases where a specific parameter is either depleted or enhanced is determined by computing the ratio of the averages and standard deviations of the parameter in one region (e.g., Region 3: Depletion Region) over the other (e.g., Regions 2 and 4: remaining plasma in the Depleted ICME).

A.1. Comparison of Depleted ICME (Regions 2,3,4) and the Surrounding Wind (Regions 1,5)

The distributions of compositions and thermal properties of protons and heavy-ions of the Depleted ICMEs are compared with their values in the wind surrounding the Depleted ICMEs. The difference between the behaviors of properties of the ions in these two regions is important because they lend themselves to our understanding of the conditions in which the entire Depleted ICME is born in the low solar corona. Due to low data counts in the individual regions analyzed ~26% of the Depleted ICMEs are excluded from the statistics. The key observational trends for the 148 Depleted ICME cases are reported in the following sections.

A.1.1. Proton Density, Speed, Temperature

a. The proton densities in the Depleted ICMEs (Regions 2, 3, and 4) are indistinguishable from their values in the plasma surrounding the Depleted ICMEs (Regions 1 and 5).

b. Proton speed is slightly slower in the Depleted ICME compared to its surrounding plasma in 62% of the cases.

c. Proton temperature is lower in the Depleted ICME than the surrounding plasma in nearly all Depleted ICMEs by a factor of 3, on average.

A.1.2. Density and Temperature of Fully-Stripped Ions: He^{2+}, C^{6+}, N^{7+}, O^{8+}

a. $n[X^{n+}]/n[X]$: The relative abundance of the fully stripped charge state of an ion to the total abundance of its element is lower in the Depleted ICME plasma compared to the plasma surrounding the Depleted ICME for C^{6+} in 79% of the Depleted ICME cases by a factor of 1.3, on average. The relative abundances of N^{7+} and O^{8+} do not show any significant trends in their differences between the Depleted ICME and its surrounding plasma.

b. $T[X^{n+}]/T[H^{1+}]$: The ion-proton relative temperatures of He^{2+}, C^{6+}, N^{7+}, and O^{8+} are greater in the Depleted ICME compared to the plasma surrounding the Depleted ICME in 85-95% of the Depleted ICME cases by factors of 2–3, on average.

c. T[X^{n+}]: The absolute temperatures of He^{2+}, C^{6+}, N^{7+}, and O^{8+} are lower in the Depleted ICME compared to the plasma surrounding the Depleted ICME in 75-90% of the cases by factors of 1.25–1.7, on average.

A.1.3. Density and Temperature of $C^{4\text{-}5+}$, $N^{4\text{-}6+}$, $O^{5\text{-}7+}$:

a. n[X^{n+}]/n[X]: The relative abundances of C^{5+}, N^{6+}, and O^{7+} to the total abundance of their elements are higher in the Depleted ICME compared to their values in the plasma surrounding the Depleted ICME in 85-95% of the cases by factors of 1.3–1.6, on average. The abundance ratio of C^{4+}/C is also greater in the Depleted ICME compared to its surrounding plasma in 61% of the cases by a factor of 1.2, on average. On the other hand, the abundance ratios of N^{5+} and O^{6+} to the total abundance of their elements are lower in the Depleted ICME compared to the surrounding plasma in 70-80% of the cases by a factor of 1.25, on average. We report no significant difference in O^{5+}/O_{total} and N^{4+}/N_{total} abundance ratios between the Depleted ICME and its surrounding plasma.

b. T[X^{n+}]/T[H^{1+}]: The ion-proton relative temperatures of C^{5+}, $N^{5\text{-}6+}$, and O^{6+} are greater in the Depleted ICME compared to the plasma surrounding the Depleted ICME in 60-80% of the cases by factors of 1.5–2.8, on average, and in >90% of the cases for C^{4+}, N^{4+}, and O^{5+} by factors of 1.7–2.8, on average, while showing no significant difference in trends in the two regions for O^{7+}.

c. T[X^{n+}]: The absolute temperatures of C^{5+}, N^{6+}, O^{7+} are lower in the Depleted ICME compared to the plasma surrounding the Depleted ICME for nearly all Depleted ICME cases by factors of 2–2.5, on average, and in over 85% of the cases for C^{4+}, $N^{4\text{-}5+}$, and $O^{5\text{-}}$

$^{6+}$ compared to the plasma surrounding the Depleted ICME in by factors of 1.33–2.22, on average.

A.1.4. Density and Temperature of the Charge States of Metals: Neon, Magnesium, Silicon, Sulphur, Iron:

In this section we discuss the plasma parameters associated with the behavior of $Ne^{8\text{-}9+}$, $Mg^{8\text{-}10+}$, $Si^{9\text{-}12+}$, $S^{10\text{-}14+}$, and $Fe^{6\text{-}20+}$.

a. $n[X^{n+}]/n[X]$: The relative abundances of the charge state of Ne^{9+}, Si^{14+}, S^{13+}, and $Fe^{12\text{-}13,17\text{-}20+}$ to the total abundance of their respective elements are greater in the Depleted ICME compared to the plasma surrounding the Depleted ICME in 60-80% of the cases, and over 85% of the cases for Mg^{10+}, $Si^{11\text{-}12+}$, and $Fe^{14\text{-}16+}$, by factors of 1.2–3.8, on average. On the other hand, the ratio of the abundances of Ne^{8+}, Si^{10+}, $S^{10\text{-}11+}$, and $Fe^{8,11+}$ to the total abundance of their elements is lower in the Depleted ICME compared to the plasma surrounding the Depleted ICME in 65-85% of the cases, and additionally lower in nearly all cases for $Mg^{8\text{-}9+}$, Si^{9+}, $Fe^{9\text{-}10+}$, by factors of 1.2–1.6, on average. We report no significant trends for S^{12+}, Fe^{6+}, and Fe^{7+}.

It is clear that the lower charge states of Ne, Mg, Si, S, and Fe are mostly depleted in the Depleted ICMEs, while their higher charge states are mostly enhanced, compared to the surrounding plasma.

b. T[X^{n+}]/T[H^{1+}]: The ion-proton relative temperatures of $Ne^{8\text{-}9+}$, Mg^{9+}, Si^{10+}, $S^{11\text{-}14+}$, and $Fe^{13\text{-}19+}$ are higher in the Depleted ICME compared to the plasma surrounding the Depleted ICME in 60-80% of the cases and >85% of the cases for Mg^{8+}, Si^{9+}, S^{10+}, $Fe^{6\text{-}12+}$ by factors ranging from 1.5 to 5, on average. We report no significant trends for the difference between ion-proton relative temperatures of Mg^{10+}, Si^{11+}, Si^{12+}, and Fe^{20+} between the Depleted ICMEs and their surrounding plasma.

c. T[X^{n+}]: The absolute ion temperatures of $S^{10,14+}$ and $Fe^{7,14,15,17+}$ are lower in the Depleted ICME compared to the plasma surrounding the Depleted ICME in 75-90% of the cases and in nearly all cases for $Ne^{8\text{-}9+}$, $Mg^{8\text{-}10+}$, $Si^{9\text{-}12+}$, $S^{11\text{-}13+}$, and $Fe^{10\text{-}13,16+}$, by factors ranging from 1.25 to 2.5, on average. We report no significant trends for the difference between the absolute ion temperatures of $Fe^{6,18\text{-}20+}$ between the Depleted ICME and its surrounding plasma.

A.1.5. Total Abundance Ratios of Carbon, Nitrogen, Oxygen and Iron

The abundance ratios of C/H, N/H, and N/O are lower in the Depleted ICME compared to the plasma surrounding the Depleted ICME in 65-85% of the cases, and nearly all cases for C/O by factors of 1.2–1.4, on average. Conversely, the Fe/O abundance ratio is higher in the Depleted ICME compared to its surrounding plasma in 83% of the cases, by a factor of 1.6, on average. We report no significant trends in the difference between the O/H abundance ratio in the Depleted ICME and its surrounding plasma.

A.2. Comparison of Depletion Region (Region 3) and the Remaining Depleted ICME (Regions 2 and 4):

The distributions of compositions and thermal properties of protons and heavy ions in the Depletion Region are compared with their values in the remaining plasma of the Depleted ICME. Due to low data counts in the individual regions analyzed ~2 to 6% of the Depleted ICMEs are excluded from the statistics.

A.2.1. Proton Density, Speed, Temperature

No differences were observed between the proton density and speed measured in the Depletion Region (Region 3) and those in the remaining Depleted ICME (Regions 2 and 4). The proton temperature, on the other hand, was lower in the Depletion Region compared to the remaining plasma in the Depleted ICME in 90% of the cases, by a factor of 2, on average.

A.2.2. Density and Temperature of Fully Stripped Ions: He^{2+}, C^{6+}, N^{7+}, O^{8+}

a. $n[X^{n+}]/n[X]$: The relative abundances of C^{6+}, N^{7+}, and O^{8+} to the total abundance of their respective elements is lower in the Depletion Region compared to the remaining plasma of the Depleted ICME in 70-90% of the cases by factors of 1.25–1.7, on average.

b. $T[X^{n+}]/T[H^{1+}]$: The ion-proton relative temperatures of He^{2+}, C^{6+}, N^{7+}, and O^{8+} are greater in the Depletion Region compared to the remaining plasma in the Depleted ICME for 70-80% of the cases, by factors of 1.7–2.2, on average.

c. $T[X^{n+}]$: The absolute temperatures of He^{2+}, C^{6+}, N^{7+}, and O^{8+} are lower in the Depletion Region compared to the remaining plasma in the Depleted ICME in 65-70% of the cases, by factors of 1.25–1.6, on average.

A.2.3. Density and Temperature of $C^{4\text{-}5+}$, $N^{4\text{-}6+}$, $O^{5\text{-}7+}$

a. $n[X^{n+}]/n[X]$: The relative abundances of $C^{4\text{-}5+}$, N^{6+}, and O^{7+} to the total abundance of its respective element is greater in the Depletion Region compared to the remaining plasma of the Depleted ICME in 70-90% of the cases, by factors of 1.2–1.5, on average. We report no trends for the difference between the abundance ratios of $N^{4\text{-}5+}/N_{total}$ and $O^{5\text{-}6+}/O_{total}$ in the Depletion Region and the remaining plasma in the Depleted ICME.

b. $T[X^{n+}]/T[H^{1+}]$: The relative ion-proton temperatures are lower for O^{7+} in the Depletion Region compared to the remaining plasma of the Depleted ICME in 69% of the cases, by a factor of 1.25, on average, while being higher for C^{4+}, N^{4+}, and O^{5+} in 65-75% of the cases by factors of 1.5–2, on average. We report no significant trends in the difference between the relative ion-proton temperatures for C^{5+}, N^{6+}, N^{5+}, O^{5+}, and O^{6+} in the Depletion Region and the remaining plasma of the Depleted ICME.

c. T[X^{n+}]: The absolute temperatures of $C^{4\text{-}5+}$, $N^{4\text{-}6+}$, and $O^{5\text{-}7+}$ are lower in the Depletion Region compared to the remaining plasma of the Depleted ICME in 70-90% of the cases, by factors of 0.5–0.9, on average.

A.2.4. Density and Temperature of the Charge States of Metals: Neon, Magnesium, Silicon, Sulphur, Iron

In this section we discuss the plasma parameters associated with the behavior of $Ne^{8\text{-}9+}$, $Mg^{8\text{-}10+}$, $Si^{9\text{-}12+}$, $S^{10\text{-}14+}$, and $Fe^{6\text{-}20+}$.

a. n[X^{n+}]/n[X]: The relative abundances of Ne^{9+}, Mg^{10+}, $Si^{11\text{-}12+}$, $S^{13\text{-}14+}$, and $Fe^{14\text{-}20+}$ to the total abundance of their respective elements are greater in the Depletion Region compared to the remaining plasma in the Depleted ICME in 60-70% of the cases, by factors of 1.1–2, on average. Conversely, the relative abundance ratio is lower for Ne^{8+}, Mg^{8+}, $Si^{9\text{-}10+}$, $S^{10\text{-}11+}$, and $Fe^{8\text{-}11+}$ in 60-75% of the cases, by factors of 1.2–1.3, on average. We report no significant trends in the difference between the relative abundance ratios of Mg^{9+}, S^{12+}, and $Fe^{6\text{-}7,12\text{-}13+}$ in the Depletion Region and the remaining plasma in the Depleted ICME.

b. T[X^{n+}]/T[H^{1+}]: The relative ion-proton temperatures for $Fe^{7\text{-}10+}$ are higher in the Depletion Region compared to the remaining plasma in the Depleted ICME in 60-70% of the cases, by a factor of 1.5–2, on average. We report no trend in the difference between the relative ion-proton temperatures of $Ne^{8\text{-}9+}$, $Mg^{8\text{-}10+}$, $Si^{9\text{-}12+}$, $S^{10\text{-}14+}$, and $Fe^{6,11\text{-}20+}$ in the Depletion Region and the remaining plasma in the Depleted ICME.

c. T[X^{n+}]: The absolute temperatures of $Ne^{8\text{-}9+}$, $Mg^{8\text{-}10+}$, $Si^{9\text{-}10,12+}$, $S^{10\text{-}14+}$, $Fe^{8\text{-}17+}$ are lower in the Depletion Region compared to the remaining plasma in the Depleted ICME for 75-90% of the Depleted ICME cases by factors ranging from 1.25 to 2, on average. We report no significant trends in the difference between the absolute temperatures of Si^{11+} and $Fe^{6\text{-}7+,18\text{-}20+}$ in the Depletion Region and the remaining plasma in the Depleted ICMEs.

A.2.5. Total Abundance Ratios of Carbon, Nitrogen, Oxygen, and Iron

The abundance ratios of C/H and C/O are lower in the Depletion Region compared to the remaining plasma in the Depleted ICME in ~90% of all cases, and also lower for N/O, N/H, and O/H in 60-70% of cases, by factors ranging from 1.25 to 1.7, on average. The Fe/O abundance ratio is higher in the Depletion Region compared to the remaining plasma in the Depleted ICME, in 67% of the cases, by a factor of 1.3, on average.

A.3. Comparison of Plasma of Depleted ICME outside the Depletion Region (Regions 2,4), and the non-Depleted ICMEs

To restate, non-Depleted ICMEs are those ICMEs where the Anomalous Wind is not detected, i.e., ICMEs where the Depletion Region is absent. There are 193 non-Depleted ICMEs between 1998 and 2011: We compare them with the ICME plasma outside the Depletion Region in the 148 Depleted ICMEs to test whether the compositional and thermal nature of the Depleted ICME is similar to all other ICMEs or not. For each parameter the average and standard deviation values for the 148 Depleted

ICMEs is compared with the average and standard deviation values of the 193 non-Depleted ICMEs.

We find that (1) the ratio of the abundance of the charge state of an ion, to the total abundance of that ion ($n[X^{n+}]/n[X]$), (2) the relative ion-proton temperature ratios ($T[X^{n+}]/T[H^{1+}]$), and (3) the absolute temperatures of the ions ($T[X^{n+}]$) of the plasma of the Depleted ICME outside the Depletion Region (Regions 2 and 4) are essentially indistinguishable from their values in the non-Depleted ICMEs, with the exception of the following:

a. $n[X^{n+}]/n[X]$: The proton densities and the ratios of the abundance of $O^{7\text{-}8+}$, Ne^{9+}, Si^{12+}, and $Fe^{15\text{-}17+}$ to the total abundance of their respective elements are greater in the plasma of the Depleted ICME outside the Depletion Region than their values in the non-Depleted ICMEs, by factors of 1.2–1.5, on average. Conversely, the ratios of the abundance of Mg^{8+}/Mg_{total} and $Fe^{6\text{-}8+}/Fe_{total}$ are lower in the plasma of the Depleted ICME outside the Depletion Region than their values in the non-Depleted ICMEs, by factors of 1.33–2.0, on average.

b. ($T[X^{n+}]/T[H^{1+}]$): The relative ion-proton temperature ratios of C^{6+}, N^{7+}, O^{8+}, and Fe^{19+} are greater in the plasma outside the Depletion Region of the Depleted ICME compared to their values in the non-Depleted ICMEs, by factors of 1.2–1.4, on average.

BIBLIOGRAPHY

Akmal A., Raymond J. C., Vourlidas A., Thompson B., Ciaravella A., Ko Y.-K., Uzzo M., & Wu R. 2001, ApJ, 553, 922

Antiochos S. K., DeVore C. R., & Klimchuk J. A. 1999, ApJ, 510, 485

Arnaud M., Rothenflug R. 1985, AAPS, 60, 425

Baker D. N., Balstad R., Bodeau J. M., et al. 2008, Severe Space Weather Events–Understanding Societal and Economic Impacts: A Workshop Report (Washington, DC: The National Academies Press)

Bame S. J., Asbridge J. R., Feldman W. C., & Kearney P. D. 1974, Sol. Phys., 35, 137

Bernasconi P. N., Rust D. M., & Hakim D. 2005, Sol. Phys., 228, 97

Brueckner G. E., Howard R. A., Koomen M. J.,F et al. 1995, Sol. Phys., 162, 357

Buergi A., & Geiss J. 1986, Sol. Phys., 103, 347

Cane H. V., & Richardson I. G. 2003, JGR, 108, 1156

Carlsson M., & Stein R. F. 1995, ApJL, 440, L29

Chen P. F. 2011, Living Rev. Sol. Phys., 8:1

Ciaravella A., Raymond J. C., Reiser P., et al. 2002, ApJ, 575, 1116

Cranmer S. R., van Ballegooijen A. A., & Edgar R. J. 2007, ApJS, 171, 520

Culhane J. L., Harra L. K., James A. M., et al. 2007, Sol. Phys., 243, 19

Del Zanna G., Dere K. P., Young P. R., Landi E., & Mason H. E. 2015, AAP, 582, A56

Delaboudini J. P., Artzner G. E., Brunaud J., et al. 1995, Sol. Phys., 162, 291

Dere K. P., Landi E., Mason H. E., Monsignori Fossi B. C., & Young P. R. 1997, VizieR Online Data Catalog, 412

Dere K. P., Landi E., Young P. R., et al. 2009, AAP, 498, 915

Domingo V., Fleck B., & Poland A. I. 1995, Sol. Phys., 162, 1

DeVore C. R., & Antiochos S. K. 2008, ApJ, 680, 740

Drake J. F., Cassak P. A., Shay M. A., et al. 2009, ApJL, 700, L16

Drake J. J., Cohen O., Garraffo C., Kashyap V. 2016, Solar and Stellar Flares and their Effects on Palents, 320, 196

Emslie A. G., Dennis B. R., Holman G. D., & Hudson H. S. 2005, JGR, 110, A1103

Emslie A. G., Dennis B. R., Shih A. Y., et al. 2012, ApJ, 759, 71

Emslie A. G., Kucharek H., Dennis B. R., et al. 2004, JGR, 109, A10104

Filippov B., & Koutchmy S. 2002, Sol. Phys., 208, 283

Fox N. J., Velli M. C., Bale S. D., et al. 2016, Space Sci. Rev., 204, 7

Geiss J., Gloeckler G., von Steiger R., et al. 1995, Science, 268, 1033

Gilbert H. R., Holzer T. E., Burkepile J. T., & Hundhausen A. J. 2000, ApJ, 537, 503

Gilbert H. R., Holzer T. E., MacQueen R. M. 2005, ApJ, 618, 524

Gilbert H., Kilper G., Alexander D., & Kucera T. 2011, ApJ, 727, 25

Gingerich O., Noyes R. W., & Kalkofen W. 1971, Sol. Phys., 18, 347

Gloeckler G., Cain J., Ipavich F. M. M., et al. 1998, SSR, 86, 497

Gombosi, T. I. 2004, Physics of the Space Environment (Cambridge: Cambridge Univ. Press)

Gopalswamy N., Barbieri L., Lu G., Plunkett S. P., & Skoug R. M. 2005, GRL, 32, LO3501

Gopalswamy N., Lara A., Yashiro S., Nunes S., & Howard R. A. 2003, Solar Variability as an Input to the Earth's Environment, 535, 403

Gosling J. T. 1993 PhFIB, 5, 2638

Gosling J. T., Pizzo V., & Bame S. J. 1973, JGR, 78, 2001

Gosling J. T., Thomsen M. F., Bame S. J., & Zwickl R. D. 1987, JGR, 92, 12399

Grevesse N., Asplund M., & Sauval A. J. 2007, SSR, 130, 105

Grevesse N., & Sauval A. J. 1998, SSR, 85, 161

Groth C. P. T., De Zeeuw D. L., Gombosi T. I., & Powell K. G. 2000, JGR, 105, 25053

Gruesbeck J. R., Lepri S. T., Zurbuchen T. H., & Antiochos S. K. 2011, ApJ, 730, 103

Hanaoka et al. 2013, astro-ph.SR, arXiv:1309.3718

Hannah I. G., & Kontar E. P. 2012, AAP, 539, A146

Hannah I. G., & Kontar E. P. 2013, AAP, 553, A10

Henke T., Woch J., Schwenn R., et al. 2001, JGR, 106, 10597

Hirshberg J., Asbridge J. R., & Robbins D. E. 1971, SoPh, 18, 313

Hirshberg J., Bame S. J., & Robbins D. E. 1972, SoPh, 23, 467

House L. L., Illing R. M. E., Sawyer C., & Wagner W. J. 1981, BAAS, 13, 862

Howard R. A., Moses J. D., Vourlidas A., et al. 2008, SSR, 136, 67

Howard R. A., Sheeley N. R., Jr., Michels D. J., & Koomen M. J. 1985, JGR, 90, 8173

Hundhausen A. 1999, The many faces of the sun: a summary of the results from NASA's Solar Maximum Mission., 148

Hundhausen A. J. 1972, Physics and Chemistry in Space, 5,

Hundhausen A. J. 1987, Sixth International Solar Wind Conference, 181

Hundhausen A. J., Gilbert H. E., & Bame S. J. 1968, JGR, 73, 5485

Illing R. M. E., Hundhausen A. J. 1985, JGR, 90, 275

Jian L. K., MacNeice P. J., Taktakishvili A., et al. 2015, Space Weather, 13, 316

Kaiser M. L., Kucera T. A., Davila J. M., et al. 2008, SSR, 136, 5

Karimabadi H., Roytershteyn V., Daughton W., & Liu Y.-H. 2013, SSR, 178, 307

Kasper J. C., Abiad R., Austin G., et al. 2016, Space Sci. Rev., 204, 131

Klein L. W., Burlaga L. F. 1982, JGR, 87, 613

Ko Y.-K., Raymond J. C., Lin J., et al. 2003, ApJ, 594, 1068

Kocher M., Landi E., Lepri S. T. 2018, ApJ, 860, 1

Kocher M., Landi E., Lepri S. T. 2018 b, ApJ, in preparation

Kocher M., Lepri S. T., Landi E., Zhao L., & Manchester W. B., IV. 2017, ApJ, 834, 147

Kohl J. L., Noci G., Cranmer S. R., & Raymond J. C. 2006 AandArv, 13, 31

Landi E., Gruesbeck J. R., Lepri S. T., Zurbuchen T. H., & Fisk L. A. 2012, ApJl, 758, L21

Landi E., Gruesbeck J. R., Lepri S. T., Zurbuchen T. H., & Fisk L. A. 2012, ApJ, 761, 48

Landi E., Lepri S. T. 2015, ApJL, 812, L28

Landi E., Lepri S. T. 2018, ApJ, in preparation

Landi E., Miralles M. P. 2014, ApJL, 780, L7

Landi E., Raymond J. C., Miralles M. P., & Hara H. 2010, ApJ, 711, 75

Landi E., Raymond J. C., Miralles M. P., & Hara H. 2010, SOHO-23: Understanding a Peculiar Solar Minimum, 428, 201

Landi E., Raymond J. C., Miralles M. P., & Hara H. 2012, ApJ, 751, 21

Landi E., Reale F. 2013, ApJ, 772, 71

Lee J.-Y., Raymond J. C. 2012, ApJ, 758, 116

Lee J.-Y., Raymond J. C., Ko Y.-K., & Kim K.-S. 2009, ApJ, 692, 1271

Lee J.-Y., Raymond J. C., Reeves K. K., Moon Y. J., & Kim K.-S. 2015, ApJ, 798, 106

Lee J.-Y., Raymond J. C., Reeves K. K., Moon Y. J., & Kim K.-S. 2017, ApJ, 844, 3

Lemen J. R., Title A. M., Akin D. J., et al. 2012, Sol. Phys., 275, 17

Lepri S. T., & Zurbuchen T. H. 2004, JGR, 109, A01112

Lepri S. T., & Zurbuchen T. H. 2010, ApJL, 723, L22

Lepri S. T., Zurbuchen T. H., Fisk L. A., et al. 2001, JGR, 106, 29231

Lin J. 2004, SoPh, 219, 169

Lin J., & Forbes T. G. 2000, JGR, 105, 2375

Lin J., Ko Y.-K., Sui L., et al. 2005, ApJ, 622, 1251

Lynch B. J., Antiochos S. K., DeVore C. R., Luhmann J. G., & Zurbuchen T. H. 2008, ApJ, 683, 1192

Lynch B. J., Edmondson J. K. 2013, ApJ, 764, 87

Lynch B. J., Edmondson J. K., Kazachenko M. D., & Guidoni S. E. 2016, ApJ, 826, 43

Lynch B. J., Reinard A. A., Mulligan T., et al. 2011, ApJ, 740, 112

Manchester W. B., IV. 2003, JGR, 108, 1162

Manchester W. B., IV., Gombosi T. I., Roussev I., et al. 2004, JGR, 109, A02107

Montgomery M. D., Asbridge J. R., Bame S. J., & Feldman W. C. 1974, JGR, 79, 3103

Mulligan T., Russell C. T., & Gosling J. T. 1999 AIP Conf. Proc. 471, The Solar Wind Nine Conf. (College Park, MD: AIP) 693

Murphy N. A., Raymond J. C., Korreck K. E., ApJ, 735, 17

Neugebauer M., Goldstein R., & Goldstein B. E. 1997, JGR, 102, 19743

Owocki S. P., Holzer T. E., & Hundhausen A. J. 1983, ApJ, 275, 354

Parenti S. 2014, Living Reviews in Solar Physics, 11, 1

Parenti S., & Vial J.-C. 2014, Nature of Prominences and their Role in Space Weather, 300, 69

Parker E. N. 1955, ApJ, 122, 293

Pesnell W. D., Thompson B. J., & Chamberlin P. C. 2012, Sol. Phys., 275, 3

Petty, W.G. 2006, A First Course in Atmospheric Radiation (Madison, WI: Sundog Publishing)

Phillips K. J., Feldman U., & Landi E. 2008, Ultraviolet and X-ray Spectroscopy of the Solar Atmosphere (Cambridge: Cambridge University Press)

Powell K. G., Roe P. L., Linde T. J., Gombosi T. I., & De Zeeuw D. L. 1999, JCoPh, 154, 284

Press W. H., Teukolsky S. A., Vetterling W. T., & Flannery B. P. 2002, *Numerical Recipes in C*, 2nd ed. (Cambridge: Cambridge Univ. Press)

Rakowski C. E., Laming J. M., Lepri S. T. 2007 ApJ, 667 602

Rakowski C. E., Laming J. M., Lyutikov M. 2011, ApJ, 730, 30

Reeves K. K., Linker J. A., Mikić Z., & Forbes T. G. 2010, ApJ, 721, 1547

Reinard A. A., Lynch B. J., & Mulligan T. 2012, ApJ, 761, 175

Richardson I. G., & Cane H. V. 1995, JGR, 100, 23397

Richardson I. G., & Cane H. V. 2004, JGR, 109, A09104

Richardson I. G., & Cane H. V. 2010, SoPh, 264, 189

Riley P., Baker D., Liu Y. D., et al. 2018, SSR, 214, 21

Rodkin D., Goryaev F., Pagano P., et al. 2017, Sol. Phys., 292, 90

Rodriguez L., Woch J., Krupp N., et al. 2004, JGR, 109, A01108

Schrijver C. J. and Siscoe G. L. 2009, Heliophysics: Plasma Physics of the Local Cosmos (Cambridge: Cambridge Univ. Press)

Shearer P., von Steiger R., Raines J. M., et al. 2014, ApJ, 789, 60

Shen C., Reeves K. K., Raymond J. C., et al. 2013, ApJ, 773, 110

Stakhiv M., Landi E., Lepri S. T., Oran R., & Zurbuchen T. H. 2015, ApJ, 801, 100

Stone J. M., & Norman M. L. 1992a, ApJS, 80, 791

Stone J. M., & Norman M. L. 1992b, ApJS, 80, 753

Tousey R. 1973, BAAS, 5, 419

Tousey R., Bartoe J. D. F., Bohlin J. D., et al. 1973, SoPh, 33, 265

Vaquero J. 2007, Historical Sunspot Observations: A Review. Advances in Space Research. 40. 10.1016/j.asr.2007.01.087.

Verner D. A., Ferland G. J., Korista K. T., & Yakovlev D. G. 1996, ApJ, 465, 487

Vidotto et al. 2014, astro-ph.SR, arXiv:1408.3943

von Steiger R., Schwadron N. A., Fisk L. A., et al. 2000, JGR, 105, 27217

von Steiger R., Zurbuchen T. H. 2011, JGR, 116, A01105

Vourlidas A., Balmaceda L. A., Stenborg G., & Lago A. D. 2017, ApJ, 838, 141

Vourlidas A., Howard R. A., Plunkett S. P., et al. 2016, Space Sci. Rev., 204, 83

Vourlidas A., Wu S. T., Wang A. H., Subramanian P., & Howard R. A. 2003, ApJ, 598, 1392

Wang Y., Cao H., Chen J., et al. 2010, “Solar Limb Prominence Catcher and Tracker (SLIPCAT): An Automated System and its Preliminary Statistical Results”, APJ, 717, 973–986, arXiv:1004.4553

Webb D. F., & Hundhausen A. J. 1987, Sol. Phys., 108, 383

Webb D. F., & Howard T. A. 2012, LRSP, 9, 3

Williams D. R., Baker D., & van Driel-Gesztelyi L. 2013, ApJ, 764, 165

Zhang J., Dere K. P., Howard R. A., Kundu M. R., & White S. M. 2001, ApJ, 559, 452

Zhao L., Landi E., Lepri S. T., et al. 2017, ApJ, 846, 2

Zhao L., Landi E., Lepri S. T., Kocher M., et al. 2016, ApJS, 228, 1

Zhao L., Landi E., Zurbuchen T. H., Fisk L. A., & Lepri S. T. 2014, ApJ, 793, 44

Zhao X. P., Webb D. F. 2003, JGR, 108, 1234

Zhao L., Zurbuchen T. H., & Fisk L. A. 2009, GRL, 36, 1

Zurbuchen T. H., Fisk L. A., Lepri S. T., & von Steiger R. 2003 AIP Conf. Proc. 679, Solar Wind Ten edited by Velli M., Bruno R., & Malara F., (Melville, NY: AIP) 604

Zurbuchen T. H., Hefti S., Fisk L. A., Gloeckler G., & Schwadron N. A. 2000, JGR, 105, 18327

Zurbuchen T. H., & Richardson I. G. 2006, SSR, 123, 31